POLITECNICO DI TORINO

Politecnico di Torino

ThalesAlenia Space
a Thales / Leonardo company

Master Degree course in Aerospace Engineering

Master Degree Thesis

Analysis and Implementation of Numerical Methods and Models for Radiative Heat Transfer in Hypersonic Regime

Supervisors
Prof. Domenic D'Ambrosio
Ing. Vincenzo Mareschi

Candidate
Lorenzo Colaci

Academic Year 2024-2025

Acknowledgements

I wish to express my deepest gratitude to **Prof. Domenic D'Ambrosio**, thesis supervisor, and to **Ing. Vincenzo Mareschi**, industrial tutor at Thales Alenia Space Italia. Their unwavering guidance has been central to the conception, execution and completion of this work.

Professor D'Ambrosio's rigorous scientific vision, combined with his constant availability for discussion, shaped the research framework and ensured that every methodological choice was sound and well motivated. His constructive criticism challenged me to refine both the technical content and the clarity of presentation, fostering a level of academic maturity that will accompany me in future endeavours.

Engineer Mareschi provided invaluable industrial perspective and hands-on expertise. His advice on practical implementation details proved decisive in overcoming key obstacles and aligning the outcomes with the needs of a real mission design environment.

To both, I extend my sincere appreciation for their patience, trust and encouragement. The professional and human qualities they demonstrated throughout this journey have been a constant source of motivation and an example of excellence that I aspire to emulate.

Abstract

Accurate prediction of the radiative heat flux at the stagnation point is critical to the sizing of thermal–protection systems (TPS) for atmospheric re-entry vehicles. This thesis investigates how thermal radiation, together with convection, shapes the overall heat load experienced during hypersonic flight. Chapter 1 offers a concise introduction to the unique physics of hypersonic aerothermodynamics—shock detachment, real-gas chemistry and plasma formation—and reviews the spectrum of radiative–transfer solvers now available, from tangent-slab and P_1 diffusion to discrete-ordinates, ray-tracing and Monte–Carlo techniques.

The research was carried out in collaboration with *Thales Alenia Space Italia*. Fluid-dynamic solutions are generated with Metacomp's CFD++, using structured two dimensional axisymmetric meshes with boundary layer clustering. Spectral emission and absorption coefficients are obtained from the SPARK line-by-line code, whose updated database spans 134 bound–bound and continuum systems; these data feed both a fast tangent-slab formulation and a Fibonacci-based ray tracer, giving a flexible tool-chain for radiative analyses.

The workflow aims to reproduce Da Silva's seminal study *Computational Fluid Radiative Dynamics of the Galileo Jupiter Entry*, providing the company with an alternative radiative calculation tool to those already in the CFD++ solver, especially for the Thermal Non-Equilibrium portion. Beyond delivering a vetted end-to-end methodology, the thesis distils best-practice guidelines on grid settings, spectral band selection and solver coupling that reduce turnaround time without sacrificing accuracy. The resulting framework equips engineers with transferable tools for next-generation missions.

Contents

List of Figures V

List of Tables VII

1 Introduction 1
- 1.1 Overview . . . 1
- 1.2 Hypersonic Flow Regime . . . 2
  - 1.2.1 Hypersonic Flow Characteristics . . . 2
  - 1.2.2 Shock: Shape and Features . . . 3
- 1.3 Thermal Protection Strategies . . . 7
  - 1.3.1 Internal Energy Modes and Non-Equilibrium Effects . . . 7
  - 1.3.2 Thermo-chemical modelling . . . 7
- 1.4 Heat-flux budget for TPS design . . . 8
- 1.5 Radiative-transfer modelling . . . 8

2 Physical Model 9
- 2.1 Intro . . . 9
- 2.2 Governing equations . . . 11
  - 2.2.1 Radiating Shock Layers . . . 12
- 2.3 Boundary conditions . . . 13
  - 2.3.1 Wall boundary condition for velocity . . . 13
  - 2.3.2 Wall boundary condition for temperature . . . 13
  - 2.3.3 Radiation-cooled surface . . . 14
- 2.4 High Temperature Gas . . . 15
  - 2.4.1 Calorically and thermally perfect gases . . . 18
  - 2.4.2 Chemically reacting mixtures of thermally perfect gases . . . 19
  - 2.4.3 Thermodynamic properties of a single chemical species . . . 20
- 2.5 Thermal Non-Equilibrium . . . 24
- 2.6 Radiation Heating . . . 27
  - 2.6.1 Specific Radiation Intensity and Radiation Flux . . . 28
  - 2.6.2 Radiative Transfer Equation . . . 31
  - 2.6.3 Transparent Gas . . . 33
  - 2.6.4 Absorbing Gas . . . 34
  - 2.6.5 Emitting and Absorbing Gas . . . 36

3 Thermal Radiation Heat Transfer Models in commercial codes 39
3.1 ICFD++ by Metacomp . . . 39
3.1.1 The P1 Radiation Model [27] . . . 39
3.1.2 The Discrete Ordinates (DO) Radiation Model . . . 44
3.1.3 Radiation Modelling: Standalone Mode . . . 50
3.1.4 Additional Specifications . . . 51
3.1.5 Conjugate Heat Transfer . . . 53
3.1.6 CFD Problem Definition: Equation Set Definition . . . 54
3.2 Star CCM+ by Siemens . . . 55
3.2.1 Participating Media Radiation . . . 55
3.2.2 Discrete Ordinate Method Numerical Solution . . . 60
3.3 Radiation Modelling in Ansys Fluent . . . 61
3.3.1 Setting the Stage . . . 61
3.3.2 Diffusion Approximations . . . 62
3.3.3 The $P-1$ radiation model in Ansys Fluent . . . 62
3.3.4 Ray-Based Solvers . . . 64
3.3.5 Surface-Only Exchange . . . 64
3.4 Statistical Path Tracing . . . 65
3.4.1 Choosing Wisely . . . 65
3.4.2 Concluding Remarks . . . 65

4 Spatial discretization 67
4.1 Topology Generation with GridPro . . . 68
4.1.1 Computational Domain Creation with Rhinoceros . . . 68
4.1.2 Importing the Geometry into GridPro . . . 71
4.1.3 Surface Meshing and Wall Classification . . . 71
4.1.4 Splitting the Surfaces . . . 72
4.1.5 Corner Definition and Geometry Validation . . . 72
4.1.6 Block Subdivision . . . 73
4.2 Mesh Generation with GridPro . . . 75
4.2.1 Grid Density Assignment and Mesh Generation . . . 75
4.2.2 Mesh Solution and Convergence . . . 75
4.2.3 Near-Wall Clustering and Boundary Layer Resolution . . . 78
4.2.4 Final Checks and Export . . . 80

5 SPARK Line-by-Line Code 81
5.1 Overview . . . 81
5.2 Capabilities and Structure of the SPARK Line-by-Line Code . . . 81
5.3 Radiative–Transfer Modules in SPARK LbL . . . 83
5.3.1 Hybrid MATLAB–Fortran Workflow . . . 83
5.3.2 Tangent Slab Model . . . 83
5.3.3 Ray-Tracing Model . . . 84
5.4 Matlab Part . . . 87

6 CFD Analysis and Results 91
6.1 Thermal Equilibrium Case . . . 91
6.1.1 Solver Convergence . . . 91
6.1.2 Mach-Number Field . . . 91
6.1.3 Static Pressure Field . . . 93
6.1.4 Static Temperature Field . . . 93
6.1.5 Stagnation-Line Profiles . . . 94
6.1.6 Species Number Densities . . . 95
6.1.7 Wall-Normal Convective Heat Flux . . . 96
6.2 Thermal Nonequilibrium Case . . . 96
6.2.1 Mach-Number Field . . . 96
6.2.2 Static Pressure Field . . . 98
6.2.3 Temperatures Field . . . 99
6.2.4 Stagnation-Line Profiles . . . 101
6.2.5 Temperatures and Species Number Densities . . . 101
6.2.6 Wall-Normal Convective Heat Flux . . . 103
6.2.7 Shock–Layer Species Distribution . . . 103
6.3 Radiative Post-Processing Workflow with SPARK . . . 107
6.3.1 Radiative Heat Flux Results . . . 107

7 Conclusions 111

Bibliography 113

List of Figures

1.1 Different kinds of supersonic vehicles [1] . . . 3
1.3 Shock features [1] . . . 5
1.4 $\beta - \theta - M$ diagram [1] . . . 6

2.1 Radiation cooled surface . . . 14
2.2 Schematic of the high-temperature regions in an entry-body flowfield, Ref [1] 16
2.3 Schematic of the plasma sheath around an Earth entry body, Ref [1] . . . 17
2.4 Schematic of the nonadiabatic, radiating flowfield around a body, Ref [1] . 17
2.5 Schematic of the temperature variation of the specific heat for a diatomic gas, Ref [1] . . . 18
2.6 Modes of molecular energy, Ref [1] . . . 22
2.7 Schematic of energy levels for the different molecular energy modes, Ref [1] 23
2.8 Geometric model for radiative intensity . . . 29
2.9 Geometric model for radiative flux, θ is the colatitude (angle from the North Pole) and $\phi = \varphi$ is the longitude . . . 30
2.10 Geometric model for the radiative-transfer equation . . . 31
2.11 Model for a transparent gas . . . 33
2.12 Infinite slab geometry for a transparent gas . . . 34
2.13 Model for an absorbing gas . . . 35
2.14 Model for an emitting and absorbing gas . . . 36
2.15 Overall scheme of absorbing-emitting medium . . . 38

3.1 Typical finite solid angle and angular space definition. . . . 45
3.2 Representation of discrete solid angle . . . 60

4.1 Galileo probe geometry [m] . . . 68
4.2 Computational domain and boundary conditions [40] . . . 69
4.3 Computational domain created with Rhino [m] . . . 70
4.4 GridPro geometry import . . . 71
4.5 GridPro surface splitting . . . 72
4.6 GridPro valid topology . . . 73
4.7 GridPro Topology 1° Upgrade . . . 74
4.8 GridPro Topology 2° Upgrade . . . 74
4.9 Initial pattern . . . 76
4.10 Mesh refinement . . . 76

4.11 Mesh convergence 64×96 cells . . . 77
4.12 Mesh clustering . . . 77
4.13 GridPro Mono-block Topology . . . 78
4.14 Initial Mesh . . . 79
4.15 Initial Mesh . . . 79

5.1 Structure of the SPARK Line-by-Line Code . . . 82
5.2 Tangent-slab model representation, Ref. [40] . . . 84
5.3 (a) Latitude-longitude scheme (b) Fibonacci-lattice scheme . . . 85
5.4 Representation of Linear Interpolation in the Ray Tracing at a given cell, Ref. [40] . . . 86
5.5 Example of a Ray-tracing calculation for a Jupiter entry at 47.5 km/s, IPFN – IST, Ray tracing (s.d.), latest access 17th july 2025. . . . 87
5.6 Mesh structure in radiative transfer module . . . 88

6.1 Residual history for the TE simulation. . . . 92
6.2 Mach number distribution (TE). White region: $M < 1$. . . . 92
6.3 Static-pressure distribution (TE); discrete shading highlights the expansion fan on the shoulder. . . . 93
6.4 Static-temperature field (TE). . . . 94
6.5 Pressure and axial velocity along the stagnation streamline (TE). . . . 95
6.6 Species number densities along the stagnation line (TE). . . . 95
6.7 Convective heat-flux profile normal to the wall at the nose (TE). . . . 96
6.8 Mach number distribution (TNE). White region: $M < 1$. . . . 97
6.9 Velocity Magnitude distribution (TNE) . . . 97
6.10 Stagnation Point zone (TNE). White region: $M < 1$ . . . 98
6.11 Static-pressure distribution (TNE); discrete shading highlights the expansion fan on the shoulder. . . . 98
6.12 Static-translational temperature field (TNE). . . . 99
6.13 Static-vibrational temperature field (TNE). . . . 99
6.14 Static-translational temperature field at Stagnation Point (TNE). . . . 100
6.15 Static-vibrational temperature field at Stagnation Point (TNE). . . . 100
6.16 Pressure (red) and axial velocity (blue) along the stagnation line (TNE). . 101
6.17 Species number densities along the stagnation line (TNE). . . . 102
6.18 Convective heat-flux profile normal to the wall at the nose (TNE). . . . 103
6.19 Molar fraction distribution of H_2 (TNE) . . . 104
6.20 Number density distribution of H_2 (TNE) . . . 104
6.21 Molar fraction distribution of H (TNE) . . . 105
6.22 Number density distribution of H_2+ (TNE) . . . 105
6.23 Number density distribution of H_2+ (TNE) at Stagnation Point . . . 106
6.24 Number density distribution of e^- (TNE) . . . 106
6.25 TNE results . . . 108
6.26 TNE results comparison with Da Silva . . . 108

7.1 Information flow in the TAS-I radiative prediction chain. . . . 112

List of Tables

2.1 List of commonly employed multi-temperature models in hypersonic flows. 27
2.2 Dissipative flux definitions, corresponding models employed and transport coefficients required as part of their definitions. Transport coefficients: D_s – mass diffusion coefficient of species s, μ – dynamic viscosity coefficient and k_k – thermal conductivity associated with thermal mode k. 27

5.1 Kinetic model employed in the present work and forward Arrhenius coefficients. 89

Chapter 1

Introduction

The present work had a two-fold ambition: *(i)* to survey the current landscape of radiation modelling for hypersonic flows and to clarify how much of that capability is already embedded in mainstream commercial CFD software, and *(ii)* to build—together with Thales Alenia Space Italia—a lean but reliable workflow that predicts the radiative heat flux reaching the stagnation point of a planetary-entry probe. Although radiative heating is rarely the principal contributor to the total thermal load in the rarefied, ultra-high-speed regime, it becomes a key driver in the sizing of ablative shields for giant-planet or exoplanet missions, where peak enthalpies push conventional design margins.

1.1 Overview

When the velocity of a gas stream overtakes the local speed of sound (Mach > 1), the motion is labelled supersonic. Push that speed several-fold higher—customarily somewhere above Mach 5–7—and specialists speak of hypersonic flow. This term does not mark a strict barrier; rather, it signals the appearance of additional thermo-chemical phenomena that ordinary supersonic theory cannot ignore.

In this high-speed domain, the bow shock collapses into an exceptionally thin layer and viscous heating becomes dominant. Temperatures just behind the shock rise so steeply that molecules dissociate, atoms ionise and new reactive species populate the gas. As the incoming velocity climbs, these effects strengthen and the shock front drifts closer to the vehicle's skin, complicating any attempt at numerical prediction beyond the reach of classic, perfect-gas solvers.

Charged-particle production also turns the post-shock gas into a dilute plasma. During orbital re-entry, for example, the ionised sheath enveloping a spacecraft can block radio waves, causing a brief loss of communication. Defence systems exploit a comparable signature: hypersonic missiles generate electrons detectable by specialised radar, allowing their trajectories to be tracked.

At such speeds the gas ahead of the body experiences vibrational and electronic non-equilibrium, intense radiative emission and rapid chemistry. Because these processes scale more directly with absolute velocity than with the Mach ratio, translational speed is the more reliable similarity parameter for hypersonic entry analyses (see Anderson, 2006, [1]).

To resume, in hypersonic flows the gas ahead of a vehicle experiences temperatures high enough for dissociation and ionization, for vibrational and electronic non-equilibrium, and for substantial radiative emission arising from the de-excitation of atoms and molecules. Because these phenomena depend more directly on translational speed than on Mach number, velocity is the more appropriate similarity parameter for hypersonic entry problems.

1.2 Hypersonic Flow Regime

This section describes the salient properties and temporal evolution of a hypersonic flow when it impacts a solid surface. The goal is to provide a unified view, connecting two complementary levels of investigation. On the one hand, the point-by-point behaviour of the gas is investigated using the balance equations that govern its dynamics; on the other, the macroscopic structure of the flow field is analysed, represented for example by the aerodynamic profile that envelops a vehicle during atmospheric reentry.

1.2.1 Hypersonic Flow Characteristics

The flow regime is strongly influenced by the Mach number of the flow, which is the ratio between flow/body velocity V and the sound speed a:

$$M = \frac{V}{a} \qquad\qquad a = \sqrt{\gamma \cdot R^* \cdot T}$$

where $\gamma = \frac{c_p}{c_v}$, $R^* = \frac{R}{\mathcal{M}}$ with R universal gas constant and $\mathcal{M}$ molar mass of the mixture.

- $M < 1$: subsonic flow
- $0.8 \leq M \leq 1.2$: transonic flow
- $M > 1$: supersonic flow

In regimes where the freestream Mach number exceeds five, the flow enters the hypersonic domain, characterized by a markedly thin shock layer—the narrow region between the shock wave and the vehicle surface. At higher speeds, maintaining the same deflection angle forces the shock wave to incline more sharply toward the body, compressing the shock layer and drawing the discontinuity closer.

Another salient feature of curved shock fronts is the spatial variation in entropy jump along different streamlines. Those intersecting the stronger portions of the shock undergo a larger entropy rise, while others crossing milder sections experience a smaller increase. This nonuniformity generates a downstream entropy gradient, commonly termed the *entropy layer*.

Such phenomena complicate the theoretical treatment of hypersonic flows. Indeed, Crocco's theorem predicts that an entropy gradient inevitably produces vorticity in the post-shock region.

$$T\nabla s = \frac{\partial \mathbf{v}}{\partial t} - \nabla h_0 - \mathbf{v} \times (\nabla \times \mathbf{v}) \tag{1.1}$$

where s represents the entropy, v denotes the velocity, h_0 is the enthalpy that remains invariant across the shock, and $\mathbf{w} = \nabla \times \mathbf{v}$ defines the fluid vorticity.

For blunt geometries, the stand-off distance of the shock front shrinks with increasing Mach number, steepening the entropy gradient in the shock–boundary region. This pronounced stratification amplifies vorticity production at high Mach speeds, which then interacts with the developing boundary layer, posing significant challenges for numerical solvers of hypersonic flows. Adjacent to the solid surface, a viscous boundary layer forms as a consequence of the no-slip condition. Under hypersonic conditions, the intense velocity gradients convert a large portion of kinetic energy into heat, elevating the near-wall temperature—a process referred to as viscous dissipation. The resultant thermal rise increases the dynamic viscosity, further thickening the boundary layer. Classical boundary-layer analysis assumes negligible pressure variation normal to the wall (i.e., $\partial p/\partial y = 0$). In this framework, the density drop near the surface must be offset by an increase in layer thickness to conserve mass flux under constant freestream conditions.

1.2.2 Shock: Shape and Features

The flight regime and mission profile of an aircraft dictate its aerodynamic efficiency. Vehicles intended for sustained supersonic cruise—such as the SR-71 Blackbird—or high-performance combat jets are equipped with finely sculpted leading edges. These sharp contours delay shock onset and diminish the wave drag that arises when traversing transonic and supersonic speed ranges.

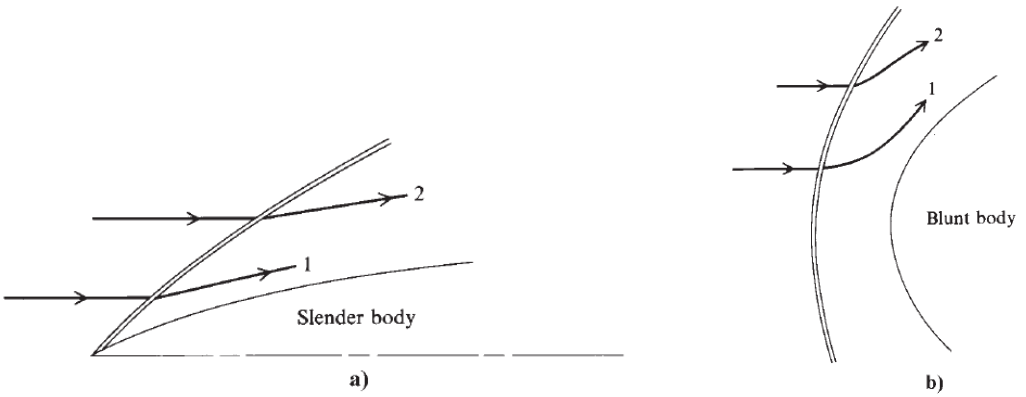

Figure 1.1: Different kinds of supersonic vehicles [1]

Conversely, re-entry capsules employ a blunt-body geometry, deliberately boosting drag to achieve rapid deceleration during atmospheric descent. This shape also thickens the shock layer, attenuating peak convective heat loads on the thermal protection system.

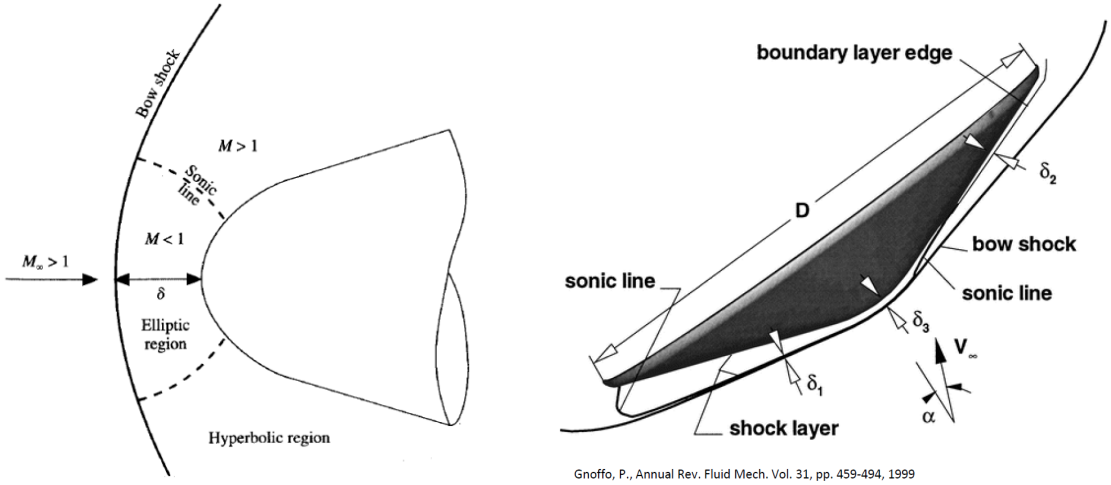

(a) Flowfield scheme over a blunt body [23] (b) Interesting features at hypersonic speeds

The flow field around a re-entry vehicle exhibits both subsonic and supersonic zones. Under supersonic freestream conditions, a detached bow shock envelops the blunt body (Figure ??), transforming much of the vehicle's kinetic energy into internal energy within the post-shock gas. Consequently, the spacecraft is immersed in a high-temperature gas layer and endures two dominant thermal loads:

1. *Convective* heating by direct molecular impact. It is inversely proportional to the root of the surface curvature radius.

$$|q_{w_C}| \propto \frac{1}{\sqrt{r}}$$

2. *Radiative* heating produced by photons emitted in the shock layer and subsequently absorbed by the surface. It is directly proportional to the body curvature of the body

$$q_{w_R} = \frac{E_e \delta}{2} \propto \frac{E_e}{2\frac{\rho_s}{\rho_\infty}} R \rightarrow |q_{w_R}| \propto R$$

Although physical shock waves possess a finite viscous thickness, CFD models invariably treat them as abrupt discontinuities. Upstream of the shock, flow variables remain essentially uniform; downstream, the abrupt deceleration in the normal direction generates steep velocity gradients and significant vorticity, giving rise to complex post-shock dynamics.

A primary objective in hypersonic blunt-body studies is to map the pressure and temperature along the surface. These surface distributions are dictated by the freestream thermodynamic state and the body's geometry. Two critical quantities—the shock detachment distance, δ (or "stand-off") and the shock's curvature—cannot be measured directly in flight. However, for canonical shapes (e.g., sphere–cone or cylinder–wedge), one can employ the empirically derived correlations of Billig [3] to obtain accurate estimates.

$$x = R + \delta - R_c \cot^2 \beta \left(\sqrt{1 + \frac{y^2}{2} \frac{\tan^2 \beta}{R_c^2}} - 1 \right) \tag{1.2}$$

$$\frac{\delta}{R} = \begin{cases} 0.143 \exp\left(\frac{3.24}{M_\infty^2}\right) & \text{sphere-cone} \\ 0.386 \exp\left(\frac{4.67}{M_\infty^2}\right) & \text{cylinder-wedge} \end{cases} \tag{1.3}$$

In this context, R refers to the nose radius, R_c denotes the curvature radius of the shock at the hyperbola's apex, and δ designates the stand-off distance (see Figure 1.3).

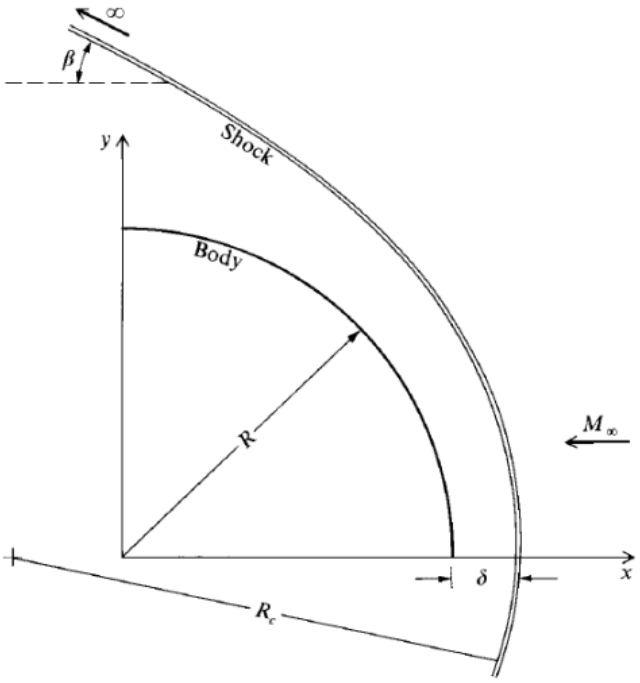

Figure 1.3: Shock features [1]

The variables x and y specify positions in the flow domain, while β represents the asymptotic shock angle far upstream of the nose. Its value depends on the freestream Mach number and the body's shape.

In the case of a sharp cone defined by half-angle θ_c, β equals the oblique shock angle for an attached shock on that cone. By contrast, for an axisymmetric cylinder aligned with the flow, β reduces to the Mach angle associated with an infinitesimal disturbance.

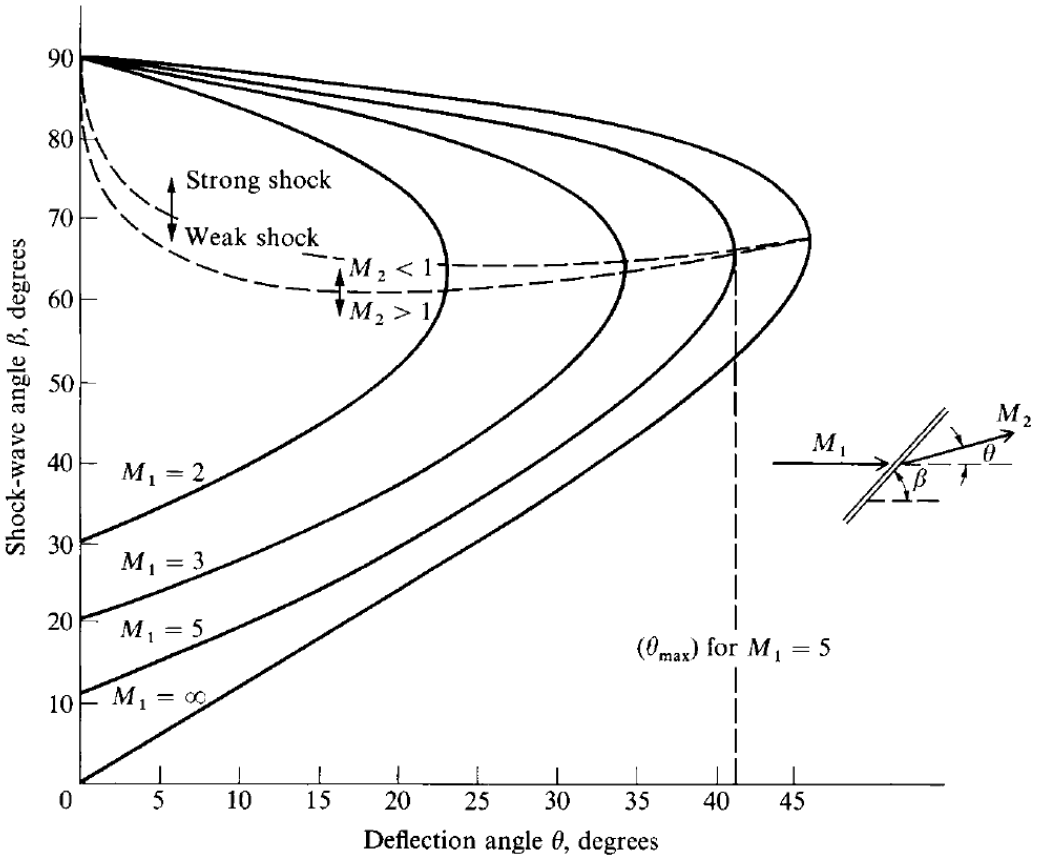

Figure 1.4: $\beta - \theta - M$ diagram [1]

Near the body's centerline, the shock attains its maximum strength and may be treated as a normal discontinuity. As one moves away from the axis, the shock angle diminishes and the wavefront curves outward. This variation is succinctly captured by the $\beta-\theta-M$ diagram (Figure 1.4), where the abscissa is the turning angle θ of the streamline and the ordinate is the shock angle β. Each curve corresponds to a fixed Mach number, illustrating how upstream speed governs the permissible β–θ combinations.

At zero deflection ($\theta = 0°$), the diagram bifurcates into two admissible solutions:

- A normal shock induces a pronounced deceleration and strong compression in the upstream flow. Applying the Rankine–Hugoniot jump conditions reveals that the downstream Mach number becomes subsonic immediately past the shock. Consequently, the gas layer directly behind the shock—adjacent to the vehicle nose—behaves according to elliptic governing equations rather than the hyperbolic form upstream.

The set of differential relations linking pre- and post-shock states is given by:

$$\rho_1 u_1 = \rho_2 u_2, \tag{1.4}$$

$$p_1 + \rho_1 u_1^2 = p_2 + \rho_2 u_2^2, \tag{1.5}$$

$$h_1 + \tfrac{u_1^2}{2} = h_2 + \tfrac{u_2^2}{2}, \tag{1.6}$$

- When the shock strength diminishes to the extent that flow variables across it remain virtually unchanged, a *vanishing shock* is said to occur. In this regime, the gas preserves its supersonic state even well downstream of the body, and the governing equations retain their hyperbolic character, reflecting the dominant propagation of wave-like perturbations.

The boundary between the subsonic and supersonic regions is called the sonic line.

1.3 Thermal Protection Strategies

Survivability therefore hinges on an appropriate thermal protection system (TPS). Reusable systems—such as those flown on the Space Shuttle—are limited to relatively gentle conditions, whereas severe environments demand ablative materials that sacrificially remove energy through pyrolysis and mass loss. Geometrically, TPS designs have ranged from spherical segments (Apollo) to sphere-cone layouts (Galileo). Increasing the nose radius reduces convective heat flux but simultaneously lengthens the radiative path, raising the photon contribution; optimal bluntness is thus mission specific.

1.3.1 Internal Energy Modes and Non-Equilibrium Effects

Post-shock temperatures are high enough to activate internal energy reservoirs that are nearly inert at lower speeds. Intermolecular collisions populate vibrational states, and when vibrational energy exceeds bond dissociation energies, molecular breakup follows. Collisions also elevate bound electrons to excited levels; spontaneous decay of these states is a potent source of ultraviolet and visible radiation. Given sufficient collisional energy, electrons can escape entirely, producing a partially ionized plasma [16].

Characteristic flow times in front of an entry vehicle are comparable to those governing chemistry and internal relaxation. Consequently, species concentrations and energy modes do not reach local thermodynamic equilibrium while the gas resides near the capsule. Accurate prediction of mass, momentum and energy transfer therefore requires models that resolve thermo-chemical non-equilibrium.

1.3.2 Thermo-chemical modelling

To capture these effects with affordable cost modern CFD codes employ macro-scopic multi-temperature models. A popular choice is the two-temperature (2-T) model introduced by Park [34], where a single vibrational/electronic temperature T_{int} evolves alongside T_{tr} and the chemical source terms are split accordingly. Relaxation of T_{int} is usually described with the Landau–Teller form and reaction rates follow Arrhenius or Park's curve-fitted expressions [10] .

1.4 Heat-flux budget for TPS design

For Earth-return capsules below about $11\,\mathrm{km\,s^{-1}}$ the Fay–Riddell stagnation correlation predicts convective wall heat fluxes that exceed any gas-phase radiative term by more than an order of magnitude, so radiation can usually be ignored at the design stage [12] . Conversely, in the Galileo probe at Jupiter entry ($v \approx 47\,\mathrm{km\,s^{-1}}$) line-by-line simulations show that radiative heating at the nose exceeds convection by a factor ≈ 3 [8] . A practical rule of thumb now adopted in ESA/NASA guidelines is:

$$q_{\mathrm{rad}}/q_{\mathrm{conv}} \gtrsim 0.1 \implies \text{full radiative analysis required.}$$

1.5 Radiative-transfer modelling

- **Tangent-Slab (TS)** — 1-D integration of the RTE along the wall normal, assuming locally parallel layers. Fast and robust; errors grow off the stagnation line [33], [8].
- **P_1 or Spherical-Harmonics** — first-order diffusion-type closure that adds angular dependence at negligible CPU penalty; suitable for moderately optically thick flows [10] .
- **Discrete Ordinates (DO)** — finite-volume solution of the RTE on a user-defined set of directions; available in most commercial CFD codes (ANSYS Fluent 2021) .
- **Ray-Tracing / DOM-Ray** — high-order line-of-sight integration over hundreds of rays; reference method for coupled flow-radiation problems, but computationally intensive [8].
- **Monte-Carlo** — statistical photon tracking, exact for any geometry and scattering law; used mainly for validation owing to its high cost [41].
- **WSGG / Multiband** — spectral-group averaging of optical properties, often coupled with any of the above solvers to accelerate CFD-level calculations; accuracy depends on band optimisation (common in LEWICE, CFD++, Fluent, etc.).

Chapter 2

Physical Model

2.1 Intro

Atmospheric entry drives the surrounding gas far beyond conventional flight conditions: velocities convert vast kinetic energy into heat, molecules dissociate, ionisation ensues, radiative exchange intensifies and, at times, electromagnetic forces intervene. Because these "high–temperature effects" emerge at Mach numbers that depend on composition, *hypersonic* designates an entire thermo-chemical milieu rather than a single velocity threshold.

This section distils the governing principles of such flows, with emphasis on thermochemical nonequilibrium. We first outline the challenges posed by elevated temperatures, then introduce a suite of physical and chemical models for predicting mixture composition. The aim is to offer clear guidance on selecting an appropriate fidelity level for any given study.

Multi-Scale Environment

A typical re-entry trajectory marches through orders of magnitude in Mach, Knudsen and Reynolds numbers. The *Knudsen number* (Kn) is a dimensionless ratio that compares the molecular mean free path λ to a characteristic geometric length L of the system (for a reentry capsule it can be defined as the diameter D):

$$\mathrm{Kn} \;=\; \frac{\lambda}{L}$$

Depending on the magnitude of Kn, different transport models apply:

- **$\mathrm{Kn} \ll 1$ — Continuum regime**
  $\lambda \ll L$; intermolecular collisions dominate. Classical Navier–Stokes equations (with Fourier heat conduction and Newtonian viscosity) are valid.
- **$\mathrm{Kn} \approx 0.1-1$ — Slip/transition regime**
  Rarefaction effects become noticeable; velocity– and temperature–slip at walls, Knudsen layers, and corrections to constitutive laws are required.

- **Kn $\gg$ 1 — Free-molecular regime**
  $\lambda \gg L$; molecule–wall interactions outweigh intermolecular collisions. The Boltzmann equation or particle methods (e.g. DSMC) must be used.

Consequently, the vehicle encounters, in rapid sequence,

- Laminar, transitional and turbulent regimes,
- Free-molecular, transitional and continuum gas,

which together inject severe stiffness into the governing equations.
High-temperature effects: a hypersonic flow is a thermo-chemically reacting flow. So chemical reactions and internal energy modes can either be frozen, in non-equilibrium or in equilibrium.

Frozen, non-equilibrium and equilibrium flows

A frozen flow is a flow in which the reaction rate constants are equal to zero ($k_f = k_b = 0$) and the vibrational relaxation time tends to infinity.
An equilibrium flow is a flow in which the reaction rate constants tend to infinity and the vibrational relaxation time is equal to zero, passing so quickly that the relaxation time is too large compared to the particle's velocity.

Examples:

- For a frozen flow, the only way to have zero change in composition and vibrational energy is to have precisely zero reaction rates, or an infinitely long relaxation time.
- For a flow in equilibrium, if temperature and pressure change as a function of space and time, the only way to maintain local equilibrium conditions at the local pressure and temperature is to have infinitely fast vibrational reaction/relaxation rates, or zero relaxation times.

In practice, neither frozen nor equilibrium flows occur in reality. However, if we define τ_f as the characteristic time for a fluid element to traverse the flow field of interest ($\tau_f = \frac{L}{V}$) and τ_c as the characteristic time for the chemical composition or vibrational energy to approach equilibrium, we can say that:

- If $\tau_f >> \tau_c$, then we can assume local equilibrium conditions.
- If $\tau_f << \tau_c$, then we can assume frozen flow.
- If $\tau_f \approx \tau_c$, then the flow is in non-equilibrium conditions.

The dimensionless parameter governing non-equilibrium is called the Damköhler number, defined as:

$$Da = \frac{\tau_f}{\tau_c}$$

For $Da \to 0$, we have a frozen flow, while for $Da \to \infty$, we can assume an equilibrium flow. If $Da = 0(1)$, the flow is non-equilibrium. Note that there can be many Damköhler numbers in a single flow field, one for each phenomenon that may be non-equilibrium. For example, we can define a Damköhler number for the vibrational energy of each diatomic species and a Damköhler number for the concentration of each species in the mixture.

Experimental and Numerical Tools

Replicating all coupled phenomena in a single experiment is seldom feasible—flight tests are costly and wind tunnels struggle to isolate individual processes without distorting others—hence researchers rely predominantly on computation. No universal solver exists:

Free-molecular/rarefied gas Direct Simulation Monte Carlo resolves the Boltzmann equation where particle collisions are scarce.

Continuum zones Conservative finite-volume formulations of the Navier–Stokes equations[1] prevail, capturing shock discontinuities while honouring fundamental balances.

Cooperation among fluid dynamicists, chemists and physicists is therefore indispensable: the gas is a reacting, multi-species mixture that may reside far from thermal or chemical equilibrium; shock layers radiate while electrons drift through magnetic fields, and every mechanism is intertwined.

2.2 Governing equations

The equations describing a reacting, non equilibrium, viscous flow containing N_s chemical species (N_v of which are molecules), can be summarized [1, 10] as follow:

$$\frac{\partial \rho}{\partial t} + \nabla\cdot(\rho\mathbf{v}) = 0 \tag{2.1}$$

$$\frac{\partial(\rho\mathbf{v})}{\partial t} \;+\; \nabla\cdot(p + \rho\mathbf{v}\mathbf{v}) \;-\; \nabla\boldsymbol{\tau} = 0 \tag{2.2}$$

$$\frac{\partial E}{\partial t} \;+\; \nabla\cdot[(E+p)\mathbf{v}] = \nabla\cdot(\boldsymbol{\tau}\cdot\mathbf{v}) \;+\; \nabla\cdot\left(k\nabla T + \sum_{i=1}^{N_s} h_i\,\rho D_i \nabla y_i\right) \tag{2.3}$$

$$\frac{\partial \rho_i}{\partial t} \;+\; \nabla\cdot(\rho_i\mathbf{v}) \;+\; \nabla\cdot\mathbf{J}_{m_i} = \Omega_i^{\mathrm{ch}}, \qquad i = 1,\ldots,N_s \tag{2.4}$$

$$\frac{\partial(\rho e_j^v)}{\partial t} \;+\; \nabla\cdot(\rho e_j^v\,\mathbf{v}) = \nabla\cdot(k_j^v\nabla T_j^v + h_j^v\,\rho D_j \nabla y_j) \;+\; \Omega_{y_j}^{\mathrm{vib}}, \qquad j = 1,\ldots,N_u \tag{2.5}$$

These equations express respectively the conservation statements for global mass, momentum, energy, single species mass and vibrational energy of molecules. In what follows the shear stress tensor is always intended to be expressed with the use of the Stokes' hypothesis, so:

$$\tau_{ij} = \mu\left[\left(\frac{\partial v_j}{\partial x_i} + \frac{\partial v_i}{\partial x_j}\right) - \frac{2}{3}(\nabla\cdot\mathbf{v}\delta_{ij})\right] \tag{2.6}$$

[1] Here, the term "Navier–Stokes equations" denotes the complete set of mass, momentum and energy conservation laws, the continuum limit of the Boltzmann equation.

while total energy E contains the contributions from internal energy modes: neglecting electronic energy:

$$E \;=\; \rho \sum_{i=1}^{N_s} \Big[y_i (e_i^{\mathrm{tr}} + e_i^{\mathrm{rot}} + e_i^{v} + \Delta h_{f_i}^{0}) \Big] \;+\; \frac{1}{2}\,\rho\,\mathbf{v}^2 \tag{2.7}$$

The physical information about the behaviour of a multicomponent gas mixture in high temperature conditions is contained in the source terms of eqs.(2.3) to (2.5).

2.2.1 Radiating Shock Layers

The compressible Navier-Stokes equations suitable for hypersonic flows are obtained by applying the equation of continuity to the conserved quantities of the flow, under the assumption of a continuum flow regime. These conserved quantities depend on the degree of thermo-chemical non-equilibrium considered,but generally consist of the mass, momentum and energy of the mixture when thermo-chemical equilibrium is assumed. For planetary entry conditions, however, an accurate description of the flow requires the inclusion of non-equilibrium effects, both chemical and thermal. When chemical non-equilibrium is considered, mass conservation of each species must be enforced individually. In turn, under conditions of thermal non-equilibrium, each independent thermal mode's energy must be conserved.

The governing equations for hypersonic radiating shock layers are:

$$\frac{\partial(\rho c_s)}{\partial t} + \nabla\cdot(\rho c_s \mathbf{V}) = \nabla\cdot\mathbf{J}_s + \dot{\omega}_s \tag{2.8}$$

$$\frac{\partial(\rho \mathbf{V})}{\partial t} + \nabla\cdot(\rho \mathbf{V}\otimes\mathbf{V}) = \nabla\cdot[\boldsymbol{\tau}] - \nabla p \tag{2.9}$$

$$\frac{\partial(\rho e)}{\partial t} + \nabla\cdot(\rho \mathbf{V} e) = \nabla\cdot(\mathbf{V}\cdot[\boldsymbol{\tau}]) - \nabla\cdot(p\mathbf{V}) - \nabla\cdot\mathbf{q} \tag{2.10}$$

where the heat flux vector is defined as

$$\mathbf{q} = -\sum_k k_k \nabla T_k + \sum_s \mathbf{J}_s h_s + \mathbf{q}_{\mathrm{rad}} \tag{2.11}$$

In addition to these equations, an additional energy conservation equation for each non-equilibrium thermal mode considered must be solved, that is,

$$\frac{\partial(\rho e_k)}{\partial t} + \nabla\cdot(\rho \mathbf{V} h_k) = \nabla\cdot\left(-k_k \nabla T_k + \sum_s \mathbf{J}_s h_{s,k}\right) + \dot{\Omega}_k \tag{2.12}$$

In Eqs.(2.8) – (2.12), ρ is the density, c_s is the species mass fraction, $\mathbf{V}$ is the flow velocity vector, $\mathbf{J}_s$ represents the mass diffusion flux vector, $\dot{\omega}_s$ is the source term for production/destruction of species s, $[\boldsymbol{\tau}]$ is the viscous stress tensor, p is the pressure, e is the specific internal energy of the mixture, k_k and T_k are the thermal conductivity and temperature associated with the thermal energy mode k, h_s is the species enthalpy, $\mathbf{q}_{\mathrm{rad}}$ is the radiative heat flux vector and, finally, e_k and $\dot{\Omega}_k$ are the internal energy and energy-exchange source term associated with thermal energy mode k.

2.3 Boundary conditions

2.3.1 Wall boundary condition for velocity

The classic boundary condition is $V = 0$ at the wall, meaning the flow adheres to the wall and this kind of boundary condition is valid in most cases in hypersonic flows. In low-density flows, when the Knudsen number is large enough to make the slip regime valid, then the velocity component parallel to the wall may be non-zero. So a standard no-slip condition can be applied to velocity. For temperature, the value at the wall can either be fixed, or an adiabatic (and radiation-adiabatic) wall can be modeled. At the wall, depending on the surface composition, species concentration can go through enhanced chemical reactions: the catalytic features can be modeled with several assumptions on the chemical source terms. In addition, provided that the computational grid is chosen in such a way that the subsonic pocket is well inside it, at the outflow boundary a supersonic exit condition can be imposed. At the inflow boundary, according to the shock-capturing philosophy, a supersonic condition is also imposed. Finally, a symmetry condition on the x axis is imposed for symmetric body geometries and particular flight conditions (zero angle of attack).

2.3.2 Wall boundary condition for temperature

In compressible viscous flows, the presence of the energy equation requires an additional boundary condition. If the gas and the solid are considered together, we study a Conjugate Heat Transfer (CHT) problem because we couple the heat exchange of the gas with that of the solid at the wall:

$$-k_g(\nabla T)g, w = -k_s(\nabla T)s, w$$

with $k_s \gg k_g$ in general and therefore $\nabla T_g \gg \nabla T_s$.

$$k_g \left(\frac{\partial T}{\partial y}\right) g, w \approx k_g \frac{T1, f - T_w}{\Delta y_g} \tag{2.13}$$

$$k_s \left(\frac{\partial T}{\partial y}\right) s, w \approx k_s \frac{T_w - T1, s}{\Delta y_s} \tag{2.14}$$

so that the unknown is T_w.

The boundary condition on the wall temperature prescribes that the wall temperature is given, i.e. $T_w = \text{const.}$, or, when the temperature varies along the body surface, $T_w = T(s)$ where s is a coordinate along the wall. This type of b.c. is justified when we know that the wall temperature will be fixed at a certain level, as happens during a very short-duration experiment in a hypersonic wind tunnel.

The boundary condition on the wall heat flux prescribes that the wall heat flux is known:

$$q_w = -k_w \left(\frac{\partial T}{\partial n}\right)_w \qquad \text{known}$$

A limiting situation occurs when the wall is thermally insulated, $k_s = \frac{1}{\infty}$, i.e. a highly insulating solid so that nothing passes through. If the RHS tends to zero, then the LHS

also tends to zero:

$$q_w = -k_w \left(\frac{\partial T}{\partial n}\right)_w = 0; \Longrightarrow; \left(\frac{\partial T}{\partial n}\right)_w = 0$$

In this case we speak of an **adiabatic wall boundary condition**. This is a very conservative condition, since the wall temperature is the highest possible because the heat is confined within the flow field.

2.3.3 Radiation-cooled surface

Radiation cooling is the basic cooling mechanism for hypersonic vehicles flying at speeds lower than 8 km/s (on Earth). It is a very effective mechanism, capable of reducing the wall temperature of a re-entry vehicle to such an extent that the materials of modern thermal-protection systems can tolerate it without additional cooling.

It is based on the assumption of a locally one-dimensional heat-transfer mechanism. The consequence of this assumption is that temperature variations on the wall in directions tangential to the surface are neglected.

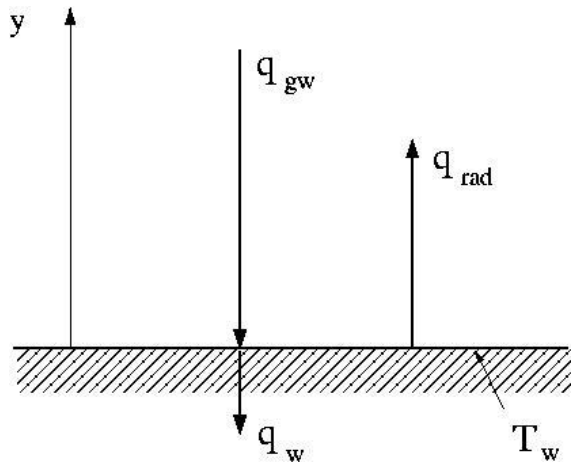

Figure 2.1: Radiation cooled surface

As shown in the figure, the local thermal balance on the vehicle surface is given by

$$q_w = q_{gw} + q_{rad}$$

Here we distinguish between q_w, which represents the net heat flux to the wall, and q_{gw}, which is the **gas** heat flux to the wall. Because the wall is cooled by radiation, the net heat flux to the wall is obtained by adding the radiative heat flux and the gas heat flux at the wall, the latter given by Fourier's law.

The heat radiated by the wall to outer space (treated as a black body at very low temperature) can be estimated using

$$q_{rad} = \varepsilon\sigma \left(T_2^4 - T_1^4\right) \tag{2.15}$$

but T_1 corresponds to the vacuum of space, so $T_2 \gg T_1$, and thus

$$q_{rad} = \varepsilon \sigma T_w^4$$

where ε is the emissivity (ranging from 0 to 1) and $\sigma = 5.670400 \times 10^{-8}$ W, m^{-2}, K^{-4} is the Stefan–Boltzmann constant. This radiation does not heat the gas, which is transparent to radiation. The radiative adiabatic wall condition equates the heat fluxes entering and leaving the surface:

$$q_{rad} = q_{conv} = -k \nabla T$$

Thermal state of a surface - Summary

Summarizing, we can distinguish five cases:

1. **Known wall temperature, without radiative cooling**: $q_w = q_{gw}$. The wall temperature is given as input, and the wall heat flux is the output.

2. **Adiabatic wall**: $q_{gw} = q_w = 0$, $q_{rad} = 0$. The wall heat flux is prescribed (zero). The wall temperature is the *adiabatic wall temperature* or *recovery temperature*, T_{aw}, and is an output.
$$\left(\frac{\partial T}{\partial y}\right) w = 0$$

3. **Radiative adiabatic wall**: $q_w = 0; \Rightarrow; q_{gw} = -q_{rad}$. The wall heat flux is prescribed (zero). The temperature is the radiative adiabatic temperature, T_{ra}, and is an output.
$$k_w \left(\frac{\partial T}{\partial y}\right) w - \varepsilon \sigma T_w^4 = 0$$

4. **Known wall temperature, with radiative cooling**: $q_w = q_{gw} + q_{rad}$. The wall temperature is given as input, and the wall heat flux is an output.

5. **Known wall heat flux**: q_w is prescribed. The wall temperature results from balancing all three heat fluxes:
$$-k_w \left(\frac{\partial T}{\partial y}\right)_w + \varepsilon \sigma T_w^4 - q_w = 0$$
Here q_w is positive when it flows from the wall to the gas (positive y direction Fig. 2.1).

2.4 High Temperature Gas

In a high-speed flow, there are regions of very high temperature where thermo-chemical processes are sufficiently strong to influence - or even dominate - the characteristics of the flow field.

For example, consider atmospheric entry. The large kinetic energy of the flow is converted, through the strong shock wave in front of the blunt body, into internal energy, so that very high temperatures occur in the shock layer, especially near the nose.

Downstream of the nose, the flow expands and cools, but near the body surface there is a boundary layer with a large external Mach number, where viscous dissipation can generate temperatures high enough to render the boundary layer a chemically reacting layer.

If the temperature is sufficiently high, ionization is also present in the shock layer. Ionized gases absorb radio-frequency radiation, and this causes a communications black-out during part of the re-entry trajectory. For this reason, predicting the electron density around a hypersonic vehicle is an important issue.

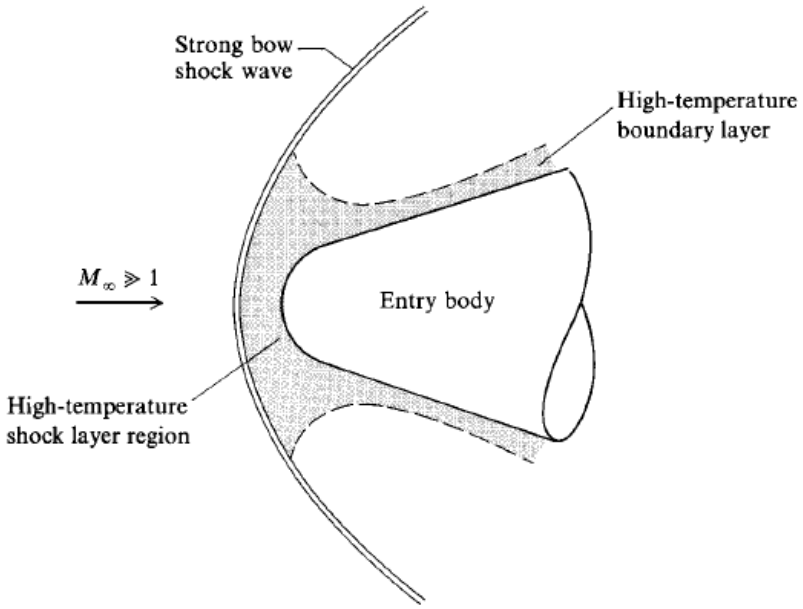

Figure 2.2: Schematic of the high-temperature regions in an entry-body flowfield, Ref [1]

Besides the phenomena mentioned above, if the flow temperature is sufficiently high, the flow itself may emit and/or absorb radiation. In this case, the flow becomes non-adiabatic, and the usual assumption of adiabatic flow, with its conceptual advantages, can no longer be employed.

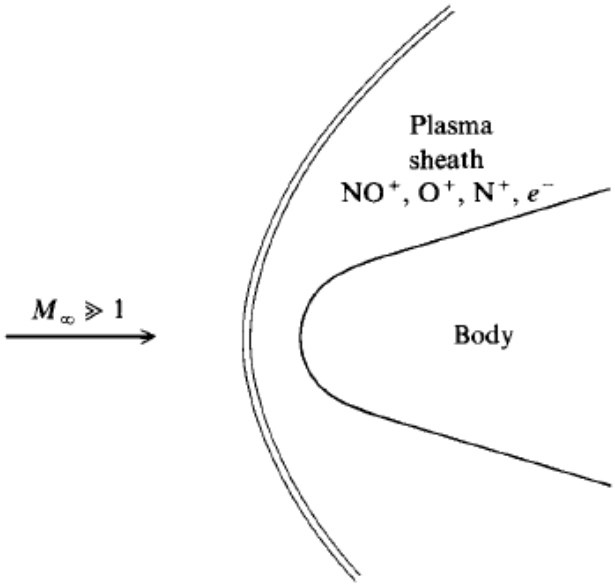

Figure 2.3: Schematic of the plasma sheath around an Earth entry body, Ref [1]

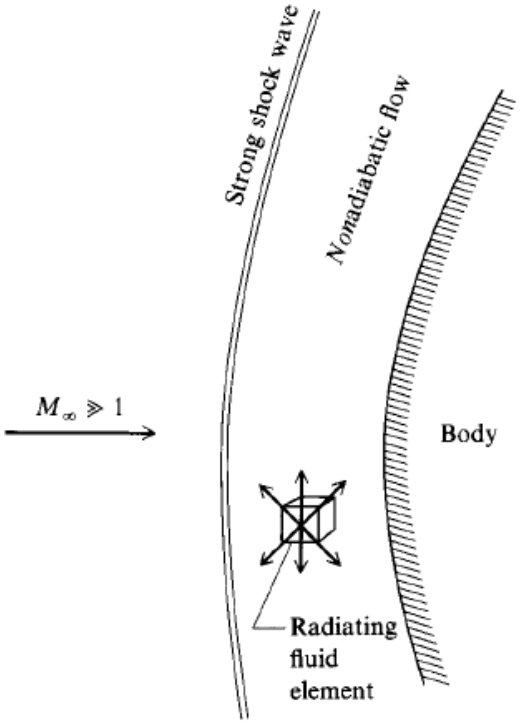

Figure 2.4: Schematic of the nonadiabatic, radiating flowfield around a body, Ref [1]

2.4.1 Calorically and thermally perfect gases

A gas that obeys the ideal-gas law is called a **thermally perfect gas**, and a gas whose specific heats are constant is a **calorically perfect gas**. Hence, a gas is ideal if it is both thermally and calorically perfect.

A thermally perfect gas can be modelled as one whose constituents have no spatial extent (point molecules) and experience no intermolecular forces except during actual collisions. This situation obtains when the molecules remain sufficiently far apart for most of the time (except during collisions) and does not require excessively high densities or pressures. In a thermally perfect gas, c_p and c_v vary and, in particular, are functions solely of temperature as shown in Fig.2.5.

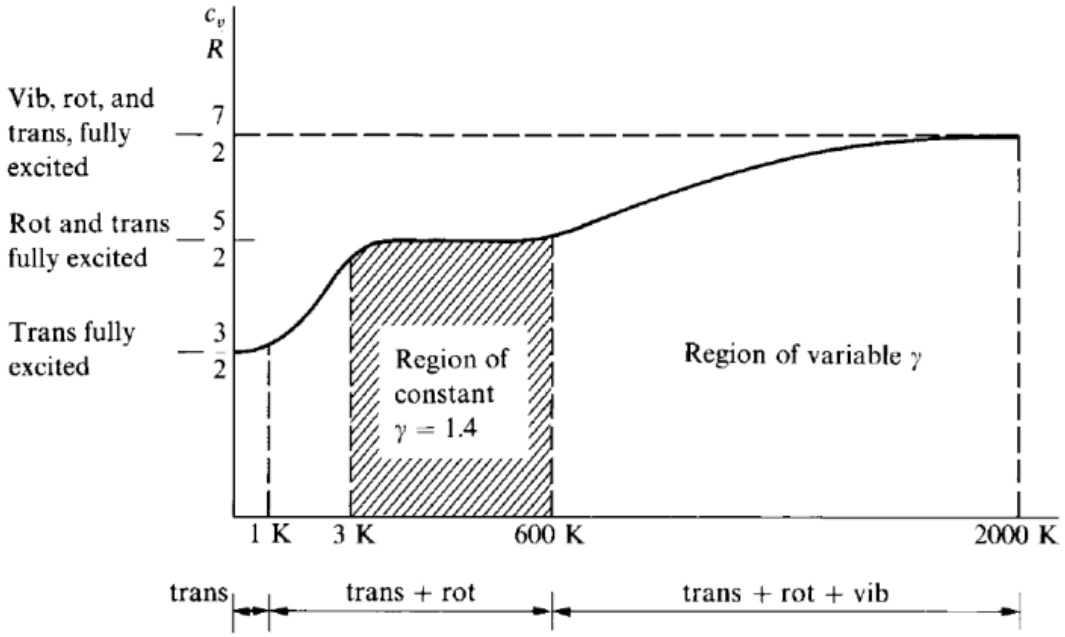

Figure 2.5: Schematic of the temperature variation of the specific heat for a diatomic gas, Ref [1]

Differential changes in internal energy and enthalpy are related to differential changes in temperature by

$$de = c_v dT \implies e_2 - e_1 = \int_{T_1}^{T_2} c_v(T)dT \quad \text{and} \quad dh = c_p dT \implies h_2 - h_1 = \int_{T_1}^{T_2 c_p(T)dT}$$

If, on the contrary, the spacing between molecules is comparable to the range of the intermolecular forces, Van der Waals effects arise. In this case the equation of state is written as

$$p = \rho RT, Z(\rho, T),$$

where Z is the compressibility factor (or real-gas factor) and can be expressed in terms

of the "*virial coefficients*" $B, C, D, \ldots$:

$$Z(\rho, T) = 1 + \rho B(T) + \rho^2 C(T) + \rho^3 D(T) + \ldots$$

Van der Waals effects become important at rather low temperatures and sufficiently high densities and pressures. During hypersonic flight, the flow conditions are such that these effects are negligible. However, they may have to be considered in ground-based hypersonic test facility, where pressure levels can be very high.

2.4.2 Chemically reacting mixtures of thermally perfect gases

Since real-gas effects are unlikely to arise in most applications of interest, we shall henceforth consider reacting gas mixtures whose constituents obey the ideal-gas law

$$p_i V = \mathcal{N}_i \mathcal{R} T \qquad \text{or} \qquad p_i = c_i \mathcal{R} T \qquad \text{or} \qquad p_i = \rho_i \frac{\mathcal{R}}{\mathcal{M}_i}, T \qquad \text{or} \qquad p_i = \rho, q_i \mathcal{R} T,$$

where p_i is the partial pressure, $\mathcal{N}_i$ the number of moles, c_i the concentration (moles per unit volume), ρ_i the partial density, and q_i the mole–mass ratio (moles per unit total mass) of the i-th species. $\mathcal{R}$ is the universal gas constant and $\mathcal{M}_i$ the molar mass of the i-th species.

The variables c_i and q_i define the composition of the gas mixture. Two other useful variables are the mass fraction y_i and the mole fraction x_i:

$$y_i = \frac{M_i}{M}, \qquad x_i = \frac{\mathcal{N}_i}{\mathcal{N}},$$

where M is the total mass and $\mathcal{N}$ the total number of moles. Using the ideal-gas law we can derive several additional useful relations:

$$\begin{aligned}
&\frac{p_i V = \mathcal{N}_i \mathcal{R} T}{p V = \mathcal{N} \mathcal{R} T} \Rightarrow \frac{p_i}{p} = x_i \\
&\frac{p_i = \rho_i R_i T}{p = \rho q_i \mathcal{R} T} \Rightarrow \frac{\rho_i}{\rho} = y_i \\
&\frac{p_i = \rho_i \frac{\mathcal{R}}{\mathcal{M}_i} T}{p = \rho \frac{\mathcal{R}}{\mathcal{M}} T} \Rightarrow x_i = y_i \frac{\mathcal{M}}{\mathcal{M}_i} = q_i \mathcal{M} \\
&\sum_i x_i = \mathcal{M} \sum_i q_i \Rightarrow \mathcal{M} = \frac{1}{\sum_i q_i}
\end{aligned}$$

In **equilibrium**, the **composition of the mixture is a function of temperature and pressure**:

$$y_i = y_i(T, p) \qquad \text{at equilibrium}$$

Here the mass fraction is used, but one could describe the mixture composition with any other suitable variable, such as the mole fraction, the molar–mass ratio, and so on. Whereas in **non-equilibrium** it is **also a function of time**:

$$y_i = y_i(T, p, t) \qquad \text{at non-equilibrium}$$

The mixture enthalpy h and internal energy e also depend on how much of each species is present in the mixture,

$$\begin{aligned} h &= h(T, y_1, y_2, y_3, ..., y_{N_s}) \\ e &= e(T, y_1, y_2, y_3, ..., y_{N_s}) \\ c_p &= c_p(T, y_1, y_2, y_3, ..., y_{N_s}) \\ c_v &= c_v(T, y_1, y_2, y_3, ..., y_{N_s}) \end{aligned}$$

In general, the mass fractions y_1,y_2,y_3,. . . ,y_n depend on T, p, and on time (or on the flow history).
The ideal-gas equation of state is still valid

$$p = \rho R T$$

but now R is a variable, because it depends on the mixture composition through the mixture molecular weight:

$$R = \frac{\mathcal{R}}{M} = \mathcal{R} \sum_i q_i.$$

Under equilibrium conditions, since $y_i = f_i(p, T)$, the above relations reduce to

$$\begin{aligned} h &= h(T, p) \\ e &= e(T, p) \\ c_p &= c_p(T, p) \\ c_v &= c_v(T, p) \end{aligned}$$

Of course, any pair among T, p, and ρ could be used to express the functional relations written above.

2.4.3 Thermodynamic properties of a single chemical species

As previously said calorically imperfect gases have variable specific heats, c_p and c_v. Here the origin of this phenomenon is examined.

The internal energy of a molecule can be modelled as if it were composed of four parts (*Bom-Oppenheimer approximation*):

$$\varepsilon' = \varepsilon'_{trans} + \varepsilon'_{rot} + \varepsilon'_{vibr} + \varepsilon'_{el}$$

- **Translational energy** ε'_{trans}: This is the translational energy, which even a single atom possesses. For polyatomic molecules, it corresponds to the translational kinetic energy of the center of mass and requires 3 thermal degrees of freedom.

- **Rotational energy** ε'_{rot}: This energy exists only for molecules. For diatomic molecules and linear polyatomic molecules, it requires 2 degrees of freedom (the rotational energy about the internuclear axis is negligible). For non-linear polyatomic molecules, it requires 3 degrees of freedom.

- **Vibrational energy** ε'_{vibr}: This energy also exists only for molecules. Imagining a molecule as atoms connected by a spring representing the intramolecular force, one degree of freedom is associated with the linear motion of the atoms as they vibrate back and forth, and a second degree of freedom is associated with the potential energy of the spring. Therefore, for linear polyatomic molecules, the vibrational energy generally requires $2(3n-5)$ degrees of freedom, whereas for non-linear polyatomic molecules it requires $2(3n-6)$ degrees of freedom, where n is the number of atoms in the molecule.

- **Electronic energy** ε'_{el}: This energy has two sources: the translational motion of the electrons along their orbits and the potential energy associated with the position of the electrons in the electromagnetic field created by the nucleus and the electrons themselves. This is a complex motion that is usually inconvenient to describe in terms of geometric or thermal degrees of freedom.

In the description of the internal energy modes presented on one of the previous pages, the reference to thermal degrees of freedom comes from classical thermodynamics. In fact, a classical theorem of kinetic theory, the *equipartition theorem*, states that each thermal degree of freedom of a molecule contributes $1/2\ k_B T$ to the energy of each molecule, or, in terms of energy per unit mass, contributes $1/2\ R_i T$ to the energy per unit mass of the gas. Kinetic theory and the equipartition theorem were developed between the late nineteenth and early twentieth centuries, before the introduction of quantum mechanics. If we also consider the translational and rotational energies, the result of the equipartition theorem is that, per unit mass

$$\begin{aligned} e_{trans} &= \frac{3}{2}RT \\ e_{rot} &= \frac{3}{2}RT \quad \text{for polyatomic molecules} \\ e_{rot} &= RT \qquad \text{for diatomic molecules} \end{aligned}$$

This result is in perfect agreement with that of modern quantum mechanics. If, however, we consider vibrational energy, the equipartition theorem tells us that, for a diatomic molecule

$$e_{vibr} = RT$$

Such a result is at odds with the result of quantum mechanics, which generally states that

$$e_{vibr} < RT \quad \text{with} \quad e_{vibr} \to RT \quad \text{only when} \quad T \to \infty$$

The formula for vibrational energy that we can obtain from quantum mechanics depends on how we choose to model the vibrational energy levels.

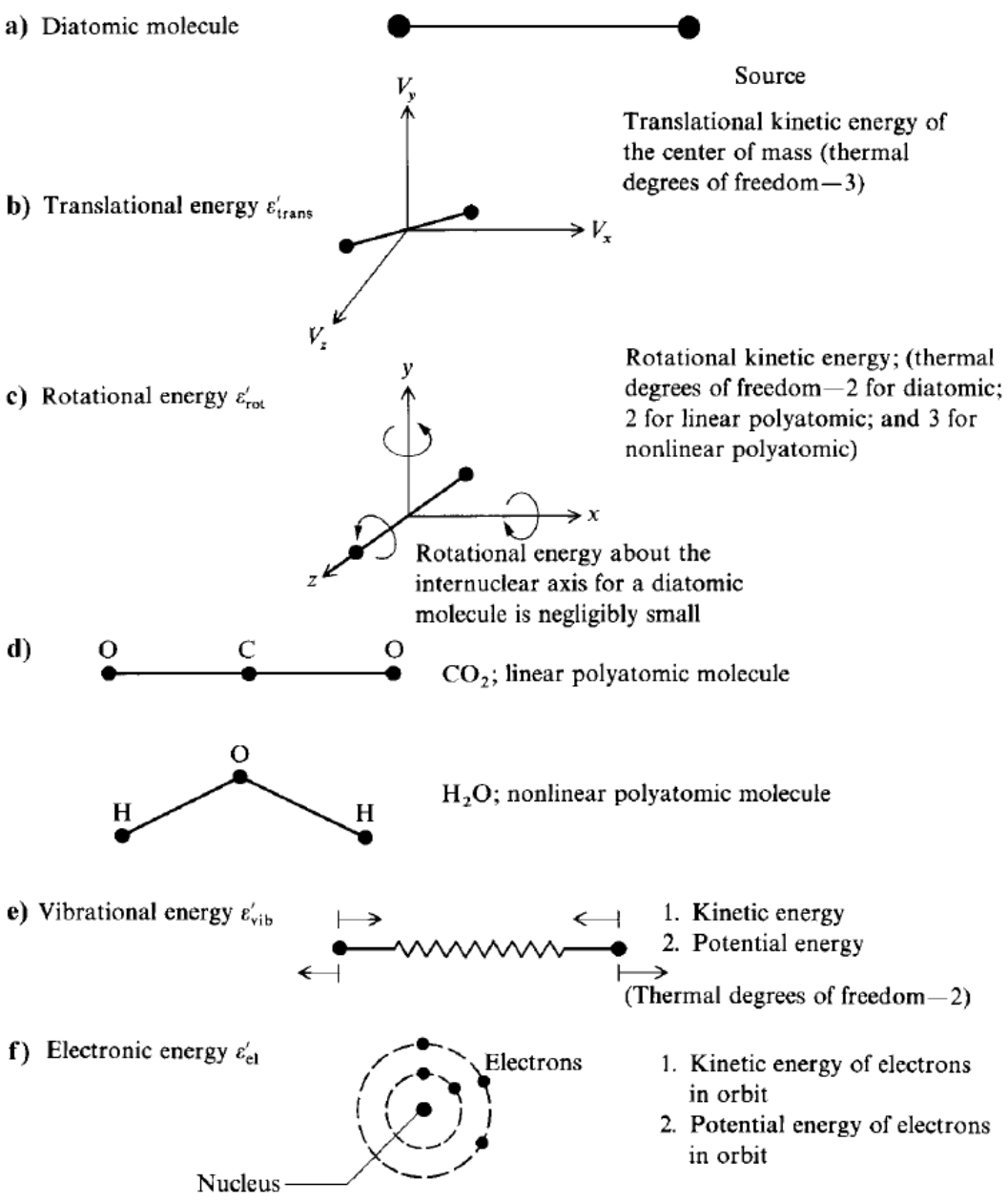

Figure 2.6: Modes of molecular energy, Ref [1]

Quantum mechanics has shown that each of the internal energies introduced earlier is **quantized**. So a molecule can possess only discrete values of translational, rotational, vibrational, and electronic energies.

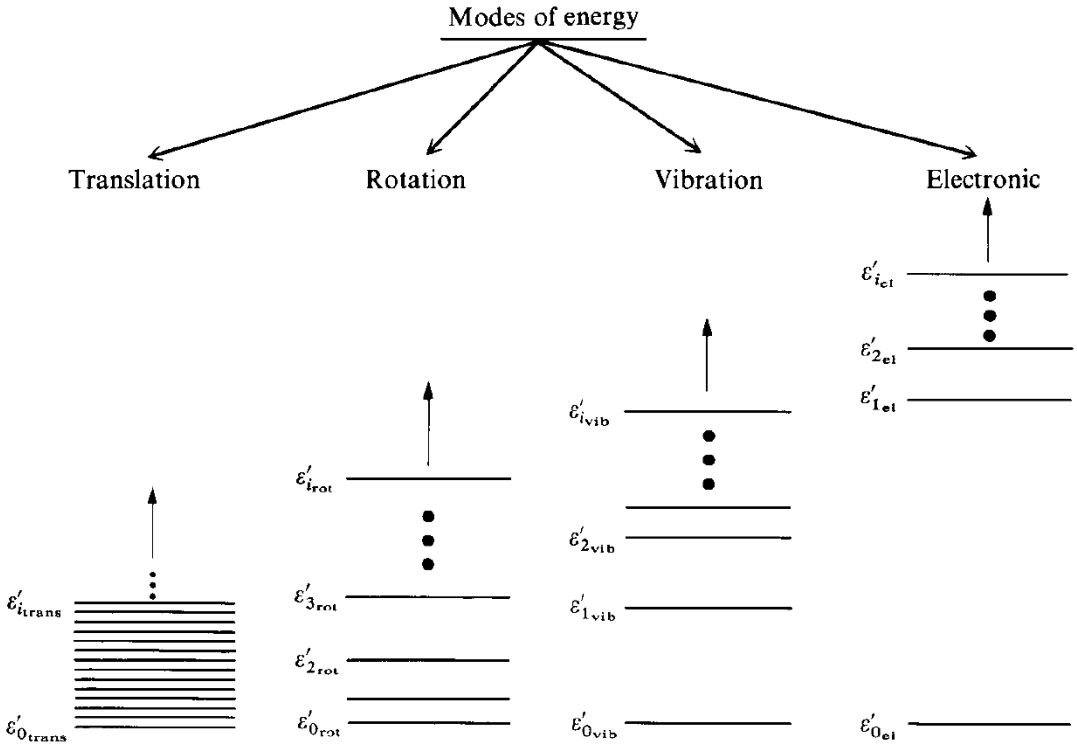

Figure 2.7: Schematic of energy levels for the different molecular energy modes, Ref [1]

The situation is illustrated in Fig.2.7. Here, each horizontal line represents a possible **energy level**. If we consider, as an example, rotational energy, we can see that the minimum rotational energy level possible is denoted as $\varepsilon'_{0_{rot}}$, then the next $\varepsilon'_{1_{rot}}$, then $\varepsilon'_{2_{rot}}$, $\varepsilon'_{3_{rot}}$, and so on. The image highlights the fact that the translational energy levels are very close to one another. The spacing between rotational energy levels is decidedly larger than that between translational energy levels and increases as the energies increase. The vibrational energy levels are much farther apart than the rotational energy levels, and in this case the spacing between two adjacent levels decreases as the energies rise. Finally, the electronic energy levels are much farther apart from each other than those of any other type of energy, and their spacing decreases as the energies rise.

The lowest allowed energy levels, $\varepsilon'_{0_{trans}}$, $\varepsilon'_{0_{rot}}$, $\varepsilon'_{0_{vibr}}$, and $\varepsilon'_{0_{el}}$, are called the ground state of the molecule. They are the energy the molecule would have at absolute zero temperature. Their values are the zero-point energies for the translational, rotational, vibrational, and electronic modes, respectively. Quantum mechanics shows that the rotational zero-point energy is exactly zero, whereas the translational, vibrational, and electronic zero-point energies are very small but non-zero. This means that, even at absolute zero temperature, molecules possess a certain amount of energy. The total zero-point energy of the molecule is therefore

$$\varepsilon'_0 = \varepsilon'_{0_{trans}} + \varepsilon'_{0_{vibr}} + \varepsilon'_{0_{el}}$$

and it is a well-defined quantity for each species. Since we are usually interested in energy variations, it is common to measure the energy of a molecule **above the zero-point energy**. We define the energies of the j-th translational level, the k-th rotational level, the l-th vibrational level, and the m-th electronic level, all measured above the zero-point energy, respectively, as:

$$\begin{aligned}
\varepsilon_{j\ trans} &= \varepsilon'_{j\ trans} - \varepsilon'_{0\ trans} \\
\varepsilon_{k\ rot} &= \varepsilon'_{k\ rot} \\
\varepsilon_{l\ vibr} &= \varepsilon'_{l\ vibr} - \varepsilon'_{0\ vibr} \\
\varepsilon_{m\ el} &= \varepsilon'_{m\ el} - \varepsilon'_{0\ el}
\end{aligned}$$

All the energy defined above, measured above the zero-point energy, is zero at absolute zero temperature.
With the definitions given above, the total energy of the molecule can be written as

$$\varepsilon'_i = \varepsilon_{j\ trans} + \varepsilon_{k\ rot} + \varepsilon_{l\ vibr} + \varepsilon_{m\ el} + \varepsilon'_0$$

and, for an atom, we have

$$\varepsilon'_i = \varepsilon_{j\ trans} + \varepsilon_{m\ el} + \varepsilon'_0$$

Note that, since the total energy of a molecule consists of quantized values, it is itself a quantized energy.
Quantum mechanics makes it possible to obtain the thermodynamic properties of a single chemical species. In what follows, we will not enter into the detailed derivation of such properties, but will simply provide and discuss the final results. For a system consisting of N molecules or atoms at a given temperature T and volume V, the Boltzmann distribution describes how many molecules or atoms of a given species, N_j, populate each energy level, ε_j, when the system is in thermodynamic equilibrium.

2.5 Thermal Non-Equilibrium

Equilibrium premise. A gaseous mixture is *thermally equilibrated* when the population of every quantum level follows a Boltzmann law, so that a single temperature T suffices for all energy reservoirs (translation, rotation, vibration, electronic, ...). In this limit the extra energy relation of Eq. (2.12) becomes redundant.

Departure from equilibrium. Spatial or temporal gradients disrupt the Boltzmann distribution: individual species may pump energy into their internal modes at dissimilar rates, and only sustained collisional or radiative exchanges can re-establish balance.

Relaxation time scale. Inter-mode energy transfer is usually expressed through a relaxation time τ_e. Whenever τ_e exceeds the characteristic flow time τ_f, the corresponding region remains out of equilibrium. Imposing $\tau_e = 0$ globally restores the single-temperature assumption—acceptable in quiescent zones, but unrealistic just behind a strong shock.

Nonequilibrium can be accommodated by assigning a distinct temperature to each lagging mode, thereby adding one energy equation per extra temperature. Because each temperature T_k carries its own conductivity κ_k, the fluid is described by multiple transport coefficients. The system therefore consists of

- a bulk energy equation for the mixture temperature T, and
- supplementary energy equations whose sources $\dot{Q}_k$ couple the modes.

Representative models. Table 2.1 lists formulations widely employed in hypersonic studies:

1. **2T (translation–rotation / vibro–electronic).** Heavy-particle translation is assumed to equilibrate with rotation, forming $T_{\text{tr-rot}}$, while vibration and electronic excitation share a common temperature T_{ve}.
2. **Park 2T.** Electron translation often decouples from heavy particles; Park therefore groups vibration, electronic excitation and electron translation into a single T_{ve} and retains $T_{\text{tr-rot}}$ for heavy particles.
3. **3T (separate electrons).** Splits free-electron translation into its own T_{e}, leaving vibration–electronic modes at T_{ve} alongside $T_{\text{tr-rot}}$.
4. **Alternative 3T.** Couples electron translation with electronic excitation, assigning $T_{\text{e+el}}$, while vibration remains distinct.
5. **Species-specific vibration.** At the highest fidelity, each chemical species s receives an individual vibrational temperature $T_{v,s}$, adding $(1 + N_s)$ energy equations when N_s species are present.

Practical limits. In theory, one could define arbitrarily many nonequilibrium temperatures; in practice, the constraint is not CPU time but the scarcity of relaxation data required to close the additional equations.

Energy bookkeeping. Whenever a multi-temperature scheme is invoked, the internal energy and enthalpy must be partitioned by mode, since each non-equilibrium energy equation (e.g. Eq. (**??**)) calls for explicit mode-wise contributions.

The task is merely to recast each thermodynamic relation with the pertinent temperature, *i.e.*,

$$e_{tr,s} = \frac{3}{2} R_g T_{tr,s}, \tag{2.16}$$

$$e_{rot,s} = R_g T_{rot,s}, \tag{2.17}$$

$$e_{vib,s} = \frac{\dfrac{h\nu_s}{k_B T_{vib,s}}}{\exp\!\left(\dfrac{h\nu_s}{k_B T_{vib,s}}\right) - 1} R_g T_{vib,s}, \tag{2.18}$$

$$e_{exc,s} = R_g T_{exc,s}^2 \frac{\partial}{\partial T_{exc,s}} \left\{ \ln\!\Big[\sum_l g_{l,s} \exp\!\Big(-\tfrac{\varepsilon_{l,s}}{k_B T_{exc,s}} \Big) \Big] \right\}. \tag{2.19}$$

As an instructive aside, imagine a cold gas whose chemistry is effectively frozen—so the reactive component of the specific heats is nil—and in which vibrational and electronic reservoirs provide a negligible fraction of the internal energy. Under these premises, one readily observes that

$$C_{v,tr,s} = \frac{3}{2} R_g, \qquad C_{p,tr,s} = \frac{5}{2} R_g, \tag{2.20}$$

$$C_{v,rot,s} = R_g, \qquad C_{p,rot,s} = R_g. \tag{2.21}$$

Under such conditions it's true that

$$C_v = \text{const}, \qquad C_p = \text{const},$$

so that their ratio attains the familiar value

$$\gamma = \frac{C_p}{C_v} = \frac{7}{5} = 1.4.$$

At these temperatures the translational and rotational reservoirs are already saturated, whereas vibrational and electronic states lie too high in energy to be excited and therefore contribute negligibly.

Capturing pronounced deviations from Boltzmann statistics demands a *state-to-state* formulation in which every quantum level is promoted to a pseudo-species. With suitably detailed, level-resolved rate coefficients, these models can reproduce arbitrary population distributions [26]. The methodology is still maturing and its intricacies fall beyond the remit of this study.

A multi-temperature framework, by contrast, assigns one temperature to each out-of-equilibrium mode. In theory an unlimited set of temperatures could be introduced; in practice, the chief constraint is not computational cost but the paucity of relaxation data required to close the additional equations.

Table 2.1: List of commonly employed multi-temperature models in hypersonic flows.

Model	**Energy Mode (Particle Type)**				
	Translational (e^-)	Translational (Heavy)	Rotational (Molecules)	Vibrational (Molecules)	Electronic (Heavy)
Equilibrium	T	T	T	T	T
2T Model	T_{ve}	$T_{\mathrm{tr-rot}}$	$T_{\mathrm{tr-rot}}$	T_{ve}	T_{ve}
3T Model	T_{el}	$T_{\mathrm{tr-rot}}$	$T_{\mathrm{tr-rot}}$	T_{ve}	T_{ve}
$(2+N_s)$T Model	T_e	$T_{\mathrm{tr-rot}}$	$T_{\mathrm{tr-rot}}$	$T_{v,s}$	T_e

Table 2.2: Dissipative flux definitions, corresponding models employed and transport coefficients required as part of their definitions. Transport coefficients: D_s – mass diffusion coefficient of species s, μ – dynamic viscosity coefficient and k_k – thermal conductivity associated with thermal mode k.

Dissipative Flux	**Symbol**	**Model**	**Mathematical Definition**	**Transport Coefficient**	**SI Units**	**Gradient**
Mass Diffusion	J_s	Fick's Law	$J_s = \rho D_s \nabla c_s$	D_s	$\mathrm{m^2\,s^{-1}}$	∇c_s
Momentum Diffusion	$[\tau]$	Newtonian Fluid[a]	$[\tau] = \mu\left(\nabla\mathbf{V} + (\nabla\mathbf{V})^{\mathrm{T}}\right) - \frac{2}{3}\mu\,(\nabla\mathbf{V})\,[\mathbf{I}]$	μ	$\mathrm{kg\,m^{-1}\,s^{-1}}$	$\nabla\mathbf{V}$
Heat Conduction	$q_{c,k}$	Fourier's Law	$q_{c,k} = k_k \nabla T_k$	k_k	$\mathrm{J\,m^{-1}\,s^{-1}\,K^{-1}}$	∇T_k

[a] Stokes' Hypothesis is also considered as part of the model, i.e. $\lambda + \frac{2}{3}\mu = 0$.

2.6 Radiation Heating

When the gas temperature is sufficiently high, the medium begins to emit energy in the form of thermal radiation and may also absorb radiation originating from other regions of the flow. As a result, a fluid particle can simultaneously lose energy due to emission and gain energy through the absorption of radiation emitted by neighbouring fluid particles. This phenomenon leads to a non-adiabatic behaviour of the flow, since an internal heat source is present within the gas. Consequently, it introduces an additional contribution to the total heat flux at the surface, referred to as radiative heating. The energy radiated by a black body per unit of time and per unit of surface in relation to its temperature is expressed by the Stefan-Boltzmann law:

$$q_r = \sigma \cdot \varepsilon \cdot T^4$$

where $\sigma = 5{,}67 \cdot 10^{-8}\ \frac{W}{m^2 K^4}$ is the Stefan-Boltzmann constant, ε is the dielectric constant and T is the absolute body temperature.
This effect becomes significant—typically on the order of 10% of the total heat flux—when local temperatures reach approximately 10,000 K, as occurs during high-speed planetary re-entries rather than from low Earth orbit.

The total heat flux at the surface, q_{tot}, is then the sum of two components: the convective-conductive contribution, q_c, and the radiative contribution, q_r:

$$q_{tot} = q_c + q_r. \tag{2.22}$$

Radiation and fluid flow are inherently coupled phenomena. The radiative properties depend on the local thermodynamic state of the flow, while in turn the flow evolution is affected by the energy exchange induced by radiation.

In general, the gas should be modelled as a participating medium (**self-absorbing gas**), meaning it both emits and absorbs radiation. A portion of the emitted radiation escapes to the surroundings, while another part is reabsorbed by the gas itself, effectively storing energy radiated by other fluid elements.

A simplified assumption can be made by treating the gas as transparent to radiation (**transparent gas**)—i.e., it emits but does not absorb. In this approximation, all radiated energy is lost to the surroundings, which considerably simplifies the modelling effort. If radiation is included, its contribution to the total heat flux must be evaluated and retained only if it exceeds a certain threshold, typically in the range of 10–15%, depending on the temperature.

It is important to emphasize that a self-absorbing gas exhibits a mathematically elliptic behaviour in the radiation transport problem, as the radiation emitted at a given location can influence the entire flow field, even in the presence of supersonic motion. Conversely, in the case of a transparent gas, radiation has only local effects, and no upstream influence occurs, making the problem strictly hyperbolic from a fluid dynamic standpoint.

2.6.1 Specific Radiation Intensity and Radiation Flux

To introduce a basic mathematical model for radiative heating, we must first define two fundamental quantities: the specific radiative intensity and the radiative flux.

1. *Specific Radiative Intensity*: is the radiative energy emitted by a unit surface and transferred in a given direction per unit time, per unit solid angle (expressed in steradians), and per unit frequency. To define it, imagine a point P in an emitting gas and define a direction starting from that point. Let dA be a virtual source surface containing the point P, from which a small but finite amount of energy dE is emitted. Now consider a small solid angle $d\Omega$ around r, which defines a cone containing the direction along which the energy is emitted.

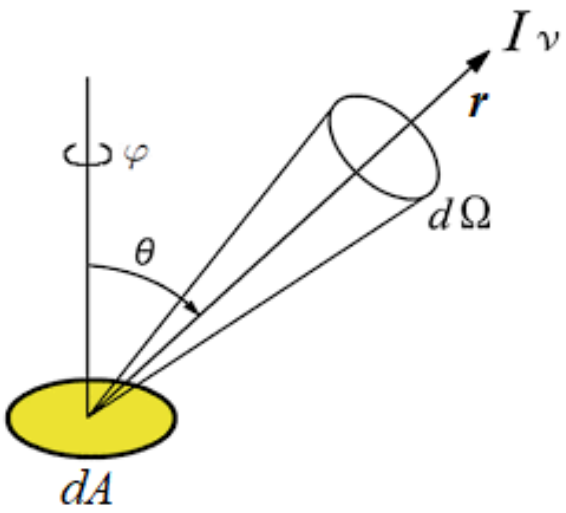

Figure 2.8: Geometric model for radiative intensity

Now it is possible to define $dE = I_\nu \cdot cos\theta \cdot dA \cdot d\omega \cdot d\nu \cdot dt$, with:

- I_ν, the frequency-specific radiative intensity ν. I_ν refers to a certain particular frequency, radiation frequency that integrates with all frequencies to get the total overall flux $[J/s \cdot sr \cdot Hz \cdot m^2]$;
- θ, angle between the direction r and the normal to the surface dA;
- dE, emitted energy;
- dA, source area;
- $d\Omega$, solid angle;
- $d\nu$, frequency band;
- dt, time interval.

2. *Radiative Flux*: is the energy per unit time (hence a power) that passes through a unit surface due to radiation coming from all directions. Therefore:

$$q_\nu = \int_{4\pi} I_\nu \cdot cos\theta \; d\omega, \tag{2.23}$$

The 4π is for the sphere since the solid angle derives from the spherical surface element. From the definition of the solid angle, which is the ratio between the area of the part of the sphere's surface subtended by the angle ($\sigma = 4 \cdot \pi \cdot r^2$) and the square of the sphere's radius, we can derive:

$$d\omega = \frac{d\sigma}{r^2}, \tag{2.24}$$

in spherical coordinates it becomes:

$$d\sigma = r \cdot d\varphi \cdot r \cdot sin\theta \cdot d\theta \tag{2.25}$$

and so:

$$d\omega = d\psi \cdot sin\theta \cdot d\theta \tag{2.26}$$

To calculate q_ν we proceed as follows:

$$q_\nu = \int_0^{2\pi} \int_0^{\pi} I_\nu(\theta, \psi) \cdot cos\theta \cdot sin\theta \; d\theta d\psi \tag{2.27}$$

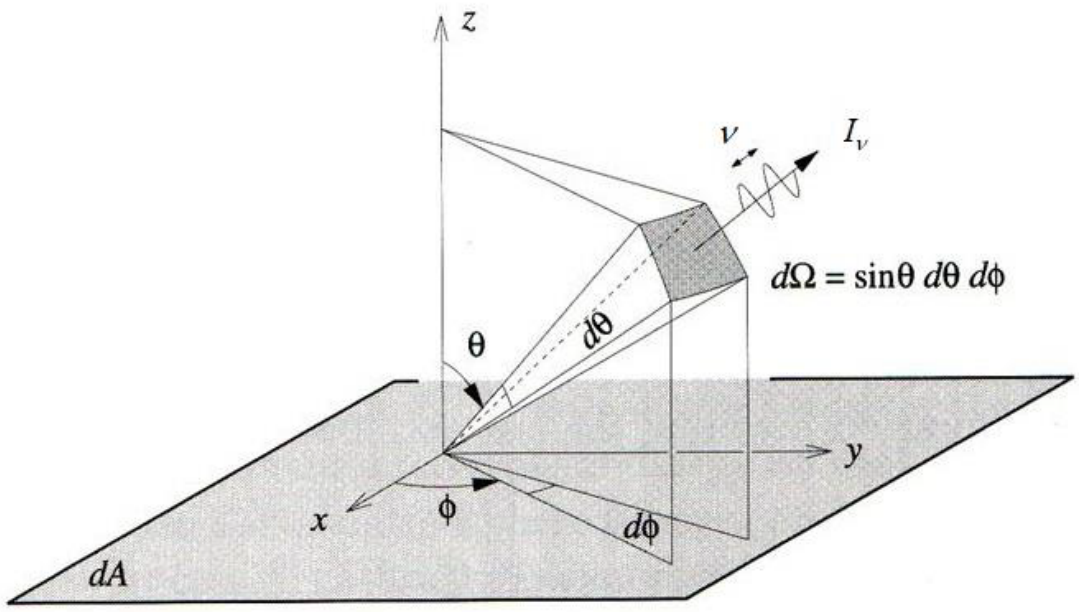

Figure 2.9: Geometric model for radiative flux, θ is the colatitude (angle from the North Pole) and $\phi = \varphi$ is the longitude

To determine the total radiative flux, we proceed by integrating over the entire frequency spectrum:

$$q = \int_0^{\infty} q_\nu \; d\nu = \int_0^{\infty} \int_0^{2\pi} \int_0^{\pi} I_\nu(\varphi, \theta) \cdot cos\theta \cdot sin\theta \; d\theta \cdot d\varphi \cdot d\nu \tag{2.28}$$

As a final point, it should be remembered that a classical black body is an idealized physical body that absorbs all incident electromagnetic radiation, regardless of frequency or angle of incidence. It also emits radiation in a characteristic spectrum that depends only on its temperature, according to Planck's law. This black body is characterized by a radiative intensity of an ideal black body given by:

$$B_\nu(T) = \frac{2 \cdot h \cdot \nu^3}{c^2 \cdot (e^{\frac{h\nu}{kT}} - 1)}, \tag{2.29}$$

where B_ν is the blackbody radiative intensity at frequency ν, h is Planck's constant, k is Boltzmann's constant, c is the speed of light, and T is the temperature.

2.6.2 Radiative Transfer Equation

Consider a volume element in a radiative gas. When radiation passes through the element in the s-direction, its intensity is modified in three ways:

- **Emission**: The air in the volume emits radiation in the s-direction, causing an increase in intensity;
- **Absorption**: The air in the volume absorbs a fraction of the radiation passing through it in the s-direction, causing a decrease in intensity;
- **Scattering**: The air in the volume scatters a fraction of the radiation in another direction (reducing the intensity), and a fraction of the remaining radiation is scattered throughout the volume in the s-direction (increasing the intensity); in other words, it is the ability of a gas or substance to deflect radiation. Here, scattering processes will be ignored.

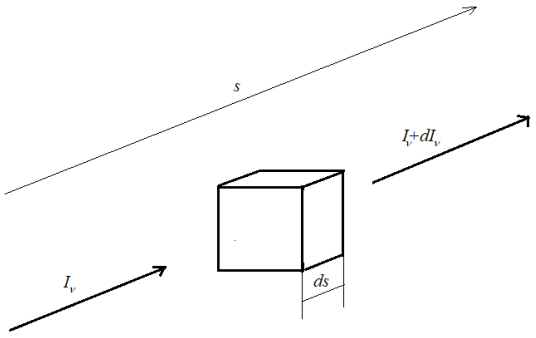

Figure 2.10: Geometric model for the radiative-transfer equation

The variation of radiative intensity can be defined as:

$$dI_\nu = J_\nu ds - k_\nu I_\nu ds \tag{2.30}$$

and hence the **Fundamental equation of radiative transfer** is expressed as:

$$\frac{dI_\nu}{ds} = J_\nu - k_\nu I_\nu \tag{2.31}$$

where the term J_ν is the emission coefficient and k_ν is the absorption coefficient.

Radiative heat flux can be calculated from this equation. Specifically, the radiative term appearing in the energy balance equation is given by the relationship between radiative heat flux and the heat transfer equation:

$$\nabla \cdot \mathbf{q}_r = \int_0^\infty \int_{4\pi} J_\nu d\omega d\nu - \int_0^\infty \int_{4pi} k_\nu I_\nu d\omega d\nu \tag{2.32}$$

since the gas emits and absorbs radiative energy from/in all directions and at all frequencies (NOTE: it's $q_r = q_{rad}$ and not q_ν because It is already integrated along ν).

Note that since the gas emits energy uniformly in all directions, we can also write:

$$\int_0^\infty \int_{4\pi} J_\nu d\omega d\nu = \int_0^\infty \int_{4pi} k_\nu I_\nu d\omega d\nu, \tag{2.33}$$

which represents the energy emitted in all directions per unit time and per unit volume, and which we will call E_e. At this point, we can make a consideration by imagining that our gas is a **blackbody** in thermal equilibrium. If this were the case, I_ν would not vary with s, since the radiative intensity of a blackbody in equilibrium conditions does not depend on s. Therefore, for a blackbody:

$$\frac{dI_\nu}{ds} = J_\nu - k_\nu B_\nu = 0, \tag{2.34}$$

and so

$$J_\nu = k_\nu B_\nu \tag{2.35}$$

That is, for a black body, the radiative intensity does not change; it emits and absorbs equally.

Now, even if the medium is not a black body but is in local thermodynamic equilibrium (i.e., in equilibrium at the local level, within a small region), Kirchhoff's law of thermal radiation states that the emissive power of an arbitrary opaque body of fixed size and shape at a given temperature can be described by a dimensionless ratio: the ratio of the body's emissive power to the emissive power of a black body of the same size and shape at the same fixed temperature.

Therefore, the relation

$$J_\nu = k_\nu B_\nu \tag{2.36}$$

holds in general, provided that the local thermal equilibrium conditions are satisfied. The previous result allows us to rewrite the radiative transfer equation as

$$\frac{dI_\nu}{ds} = k_\nu B_\nu - k_\nu J_\nu, \tag{2.37}$$

recalling that the terms in the above equation, such as $\frac{dI_\nu}{ds}$, have the dimensions of energy per second per unit solid angle per unit frequency per unit volume.

2.6.3 Transparent Gas

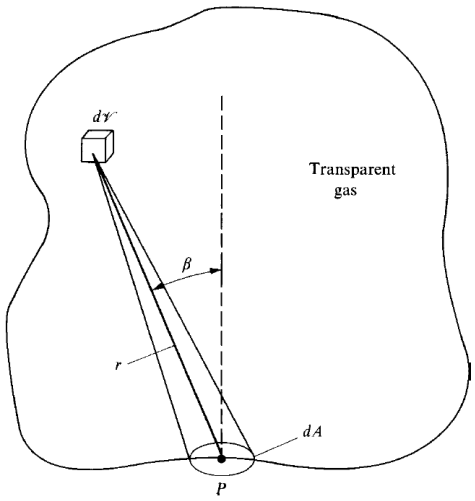

Figure 2.11: Model for a transparent gas

Let us now consider the case of a transparent gas, that is, a gas that emits only radiation: I remove the absorption term ($K_\nu I_\nu = 0$); therefore the fundamental equation of radiative transfer is

$$\frac{dI_\nu}{ds} = k_\nu B_\nu \tag{2.38}$$

Referring to the image, we want to know the total radiative heat flux generated by a transparent gas within the volume V that crosses the boundaries of the volume itself.

To do this, we need to integrate J_ν

$$\int_V \int_0^{4\pi} \int_0^{\infty} J\nu d\nu d\omega dV = \int_V \int_0^{\infty} J d\omega dV = \int_V J \frac{dA cos\beta}{r^2} dV \tag{2.39}$$

to obtain the flux, simply divide by dA, and remembering that $E_e = 4\pi J$, which represents the energy emitted by the gas in all directions per unit of time and per unit of volume, and 4π is the integration on ω which covers the entire sphere, we obtain:

$$q_r = \frac{1}{4\pi} \int_V E_e \frac{cos\beta}{r^2} dV. \tag{2.40}$$

Now, consider an infinitely wide slab of radiative gas with constant properties (constant pressure and temperature) of thickness δ. The slab represents the shock layer in the region around the stagnation point. The left side of the slab is the shock, and the right side is the wall. As a rough approximation, we assume that all flow properties in the shock layer (i.e., the slab) are constant and equal to the post-shock conditions, so we can assume that E_e is constant everywhere.

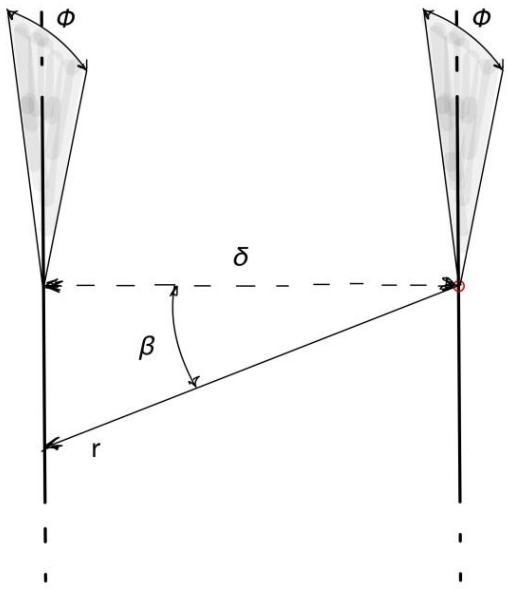

Figure 2.12: Infinite slab geometry for a transparent gas

Several theoretical studies in the literature have shown that, for sufficiently high Mach numbers, the normalized shock separation distance at the stagnation point, δ/R , in our case, is proportional to $\frac{\delta}{R} \propto \frac{\rho_\infty}{\rho_s}$, where R is the radius of curvature of the body at the stagnation point and ρ_s is the post-shock density. Combining this result with the estimated radiative heat flux, we obtain that the radiative heat flux is proportional to the shock layer thickness δ and δ is proportional to the radius of curvature R:

$$q_R = \frac{E_e \delta}{2} \propto \frac{E_e}{2\frac{\rho_s}{\rho_\infty}} R \rightarrow q_R \propto R \tag{2.41}$$

This is an interesting result showing that, unlike conductive heat flux, which is inversely proportional to the square root of R ($q_c \propto 1/\sqrt{R}$), radiative heat flux at the wall is directly proportional to the radius of curvature of the body. Therefore, when designing thermal protection systems for lunar or other interplanetary reentry missions, a trade-off will need to be considered to minimize both conductive and radiative heat fluxes, which behave oppositely to the curvature of the blunt nose: the flatter the body, the more radiation it receives.

2.6.4 Absorbing Gas

Now consider the opposite situation to a transparent gas, that is, a gas that only absorbs energy, without emitting it. In this case, the radiative transfer equation reads:

$$\frac{dI_\nu}{ds} = -k_\nu I_\nu \tag{2.42}$$

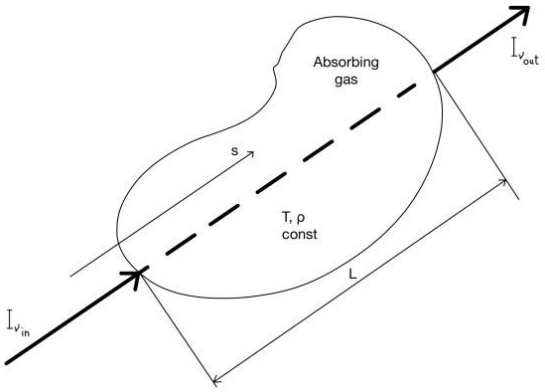

Figure 2.13: Model for an absorbing gas

The radiative intensity in the s-direction enters the volume as $I_{\nu,in}$, and exits as $I_{\nu,out}$, after traversing a volume V for a length L. Integrating the radiative transfer equation, we obtain:

$$\int_{I_{\nu,in}}^{I_{\nu,out}} \frac{dI_\nu}{I_\nu} = -\int_0^L k_\nu ds \tag{2.43}$$

Now, if we assume that the gas has homogeneous properties, hence constant pressure and density, then k_ν is constant, and the solution is:

$$I_{\nu,out} = I_{\nu,in} e^{-k_\nu L} \tag{2.44}$$

If, instead, the gas has variable properties, then k_ν varies along s, and the solution is:

$$I_{\nu,out} = I_{\nu,in} e^{-\tau_\nu} : \tag{2.45}$$

the integral just shown is called Optical Integral, thanks to the presence of τ_ν called *Optical Thickness* and defined as:

$$\tau_\nu = \int_0^L k_\nu ds \tag{2.46}$$

2.6.5 Emitting and Absorbing Gas

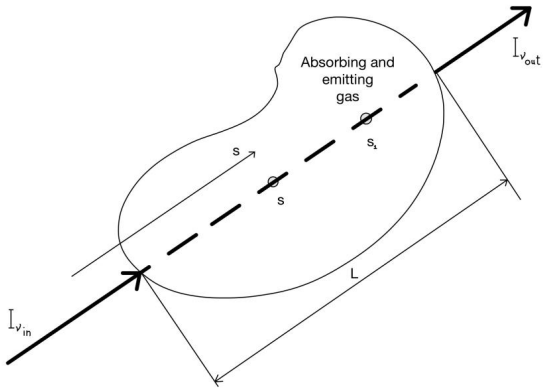

Figure 2.14: Model for an emitting and absorbing gas

Now consider a gas with variable properties that both emits and absorbs radiation. The radiative transfer equation is:

$$\frac{dI_\nu}{ds} = k_\nu B_\nu - k_\nu I_\nu. \tag{2.47}$$

Using the definition of optical thickness, we obtain: $d\tau_\nu = k_\nu ds$. Now, let's assume a solution of the type:

$$I_\nu = c(\tau_\nu)e^{-\tau_\nu}, \tag{2.48}$$

with $c(\tau_\nu)$ which is a coefficient that can change with s because $\tau_\nu = \int_0^L k_\nu ds$ and differentiating we obtain:

$$\frac{dI_\nu}{d\tau_\nu} = -c \cdot (\tau_\nu)e^{-\tau_\nu} + e^{-\tau_\nu}\frac{dc}{d\tau_\nu}. \tag{2.49}$$

Substituting the two equations above into the radiative transfer equation, we get:

$$-c \cdot (\tau_\nu) \cdot e^{-\tau_\nu} + e^{-\tau_\nu}\frac{dc}{d\tau_\nu} = B_\nu - c \cdot (\tau_\nu)e^{-\tau_\nu} \rightarrow \frac{dc}{d\tau_\nu} = e^{\tau_\nu}B_\nu \tag{2.50}$$

Since τ_ν =0 when s=0 (start), and setting $\tau_\nu = \tau_{\nu 1}$ when $s = s_1$, we can integrate the above equation as:

$$c(\tau_{\nu 1}) - c(0) = \int_0^{\tau_{\nu 1}} B_\nu e^{\tau_\nu} d\tau_\nu, \tag{2.51}$$

knowing that:

$$c(\tau_{\nu 1}) = I_\nu(s_1)e^{\tau_{\nu 1}}c(0) = I_\nu(0), \tag{2.52}$$

from the definition of the solution,
and

$$c(0) = I_\nu(0), \tag{2.53}$$

The general solution to the radiative transfer equation for a gas with variable properties that emits and absorbs radiation is as follows:

$$I_\nu(s_1) = I_{\nu,in}e^{-\tau_{\nu 1}} + \int_0^{\tau_{\nu 1}} B_\nu e^{-(\tau_{\nu 1} - \tau_\nu)} d\tau_\nu, \tag{2.54}$$

where the first term represents the radiative intensity that entered the volume after being attenuated by absorption between $s = 0$ and $s = s_1$, and the second term is the radiation emitted at any position s after being attenuated by absorption between s and s_1. In particular, the first term represents the incoming radiation absorbed and damped up to s_1, while the second represents the radiation emitted, at a generic position, which is damped because I have moved in the meantime and is therefore absorbed up to s_1; B_ν is only a function of T since it is the emissivity of the blackbody (and of the frequency ν).

Instead of assuming a possible solution for the radiative transfer equation, another method to solve it is to use the *factor integration method*, a technique for solving first-order ordinary differential equations. In this case, the method is applied by multiplying the radiative transfer equation by a function (the integrating factor) which is usually an exponential because the derivative always remains the same:

$$\frac{dI_\nu}{d\tau_\nu} = B_\nu - I_\nu \rightarrow e^{\tau_\nu}\frac{I_\nu}{d\tau_\nu} = e^{\tau_\nu}B_\nu - e^{\tau_\nu}I_\nu \rightarrow e^{\tau_\nu}\frac{dI_\nu}{d\tau_\nu} + e^{\tau_\nu}I_\nu = e^{\tau_\nu}B_\nu \rightarrow \frac{d}{d\tau_\nu}(e^{\tau_\nu}I_\nu) = e^{\tau_\nu}B_\nu \tag{2.55}$$

N.B: $\frac{dI_\nu}{d\tau_\nu} \cdot e^{\tau_\nu} + e^{\tau_\nu}I_\nu$ is precisely the differential of $e^{\tau_\nu}I_\nu$, that is: $\frac{d}{d\tau_\nu}(\tau_\nu I_\nu) = e^{\tau_\nu}B_\nu$
Integrating between $s = 0$ and $s = s_1$ as done previously, we obtain:

$$\int_0^{\tau_{\nu 1}} \frac{d}{d\tau_\nu}(e^{\tau_\nu}I_\nu)d\tau_\nu = \int_0^{\tau_{\nu 1}} e^{\tau_\nu}B_\nu d\tau_\nu \rightarrow e^{\tau_{\nu 1}}I_\nu[\tau_{\nu 1}(s_1)] - I_\nu(0) = \int_0^{\tau_{\nu 1}} e^{\tau_\nu}B_\nu d\tau_\nu \tag{2.56}$$

$$I_\nu[\tau_{\nu 1}(s_1)] = I_\nu(0)e^{-\tau_\nu 1} + \int_0^{\tau_\nu 1} B_\nu e^{-(\tau_{\nu 1} - \tau_\nu)}d\tau_\nu \tag{2.57}$$

The result of equation (2.56) is the same result we obtained in the previous equation (2.53).

To obtain the radiation term in the energy equation, recall that the radiative energy emitted per unit time and per unit volume is defined as:

$$E_e = 4\pi J = 4\pi \int_0^\infty k_\nu B_\nu d\nu \tag{2.58}$$

On the other hand, the energy absorbed per unit time per unit volume is:

$$E_a = \int_0^\pi \int_{4\pi} k_\nu I_\nu d\omega d\nu = \int_0^\infty \int_0^{2\pi} \int_0^\pi k_\nu I_\nu sin\theta d\theta d\varphi d\nu \tag{2.59}$$

where I_ν is the solution we got previously, i.e.

$$I_\nu[\tau_{\nu 1}(s_1)] = I_\nu(0)e^{-\tau_{\nu 1}} + \int_0^{\tau_{\nu 1}} B_\nu e^{-(\tau_{\nu 1} - \tau_\nu)}d\tau_\nu \tag{2.60}$$

I integrated E_a between 0 and ∞ because the radiative intensity is on a monochromatic frequency, while on 4π because it is from all directions

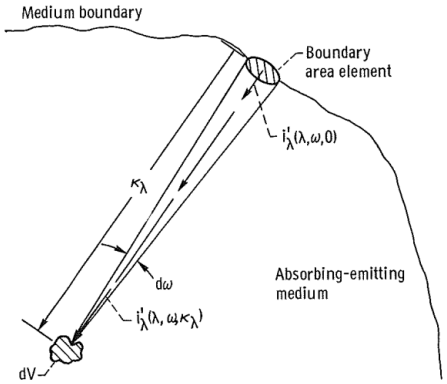

Figure 2.15: Overall scheme of absorbing-emitting medium

The radiative flux divergence in the energy balance equation represents the net amount of radiative energy leaving the elementary control volume per unit time. A positive value indicates that more energy leaves the volume than enters, while a negative value indicates the opposite. Therefore, in spherical coordinates:

$$\nabla \cdot \mathbf{q}_r = E_e - E_a = 4\pi \int_0^\infty k_\nu B_\nu d\nu - \int_0^\infty \int_0^{2\pi} \int_0^\pi k_\nu I_\nu sin\theta d\theta d\varphi d\nu \tag{2.61}$$

The values of k_ν are highly dependent on the reactions and vary according to the frequency ν.

This chapter draws partially from the unpublished lecture slides of the course *Hypersonic Aerothermodynamics* by Prof. Domenic D'Ambrosio, Politecnico di Torino [9].

Chapter 3

Thermal Radiation Heat Transfer Models in commercial codes

3.1 ICFD++ by Metacomp

3.1.1 The P1 Radiation Model [27]

The P_1 approximation converts the full integro-differential radiative-transfer equation into a diffusion-like form, supplying a computationally economical yet adequately accurate strategy for modelling radiative heat transport within CFD simulations.

Introduction

In CFD++ radiative heat transport is handled through the P_1 scheme, a particular member of the broader P_N moment hierarchy. The procedure defines angular moments of the specific intensity and, by taking moments of the radiative-transfer equation, generates a coupled system whose solution supplies the radiative energy flux required in the medium's energy balance.

Introducing successively higher moments, however, produces more unknowns than equations. Closure is obtained by expanding the intensity in spherical harmonics: truncating the series after N terms yields the P_N approximation, while the special case $N = 1$ recovers the familiar P_1 diffusion model.

Equation of Radiative Heat Transfer [41]

Radiation travelling through a participating medium is weakened by absorption and out-scattering yet reinforced by thermal emission and in-scattering from other directions. The *total intensity*, I, expresses the energy rate passing through a unit area, per steradian, per unit time, on a surface normal to the ray and summed over every wavelength. Conversely, the *spectral intensity*, I_λ, denotes the same quantity per wavelength interval.

For a medium that simultaneously absorbs, emits, and scatters, the evolution of I_λ along a coordinate s is described by the radiative-transfer equation

$$\frac{dI_\lambda}{ds} = -\kappa_\lambda I_\lambda + \kappa_\lambda I_\lambda^* - \gamma_\lambda I_\lambda + \gamma_\lambda \frac{1}{4\pi} \int_{\Omega_i=0}^{4\pi} I_\lambda(s, \Omega_i) \Phi(\lambda, \Omega, \Omega_i) d\Omega_i \tag{3.1}$$

where $\Phi(\lambda, \Omega, \Omega_i)$ is the phase function, and $\frac{\Phi(\lambda,\Omega,\Omega_i)}{4\pi}$ is the percentage of the intensity scattered from a given direction into the s direction. For isotropic scattering, $\Phi(\lambda, \Omega, \Omega_i) = 1$.

In Eq. (3.1) each term on the right has a clear role.

- **Absorption** (including stimulated emission) subtracts energy from the beam.
- **Spontaneous emission** adds energy, with no contribution from induced processes.
- **Out–scattering** diverts intensity away from the ray.
- **In–scattering** supplies energy from other directions into the path s.

If the extinction coefficients are uniform and scattering is isotropic, integrating Eq. (3.1) over all wavelengths collapses the relation to its grey–gas form:

$$\frac{dI}{ds} = -(\kappa + \gamma) I + \kappa I^* + \gamma \frac{1}{4\pi} \int_{\Omega_i=0}^{4\pi} I(s, \Omega_i) d\Omega_i \tag{3.2}$$

It is useful to write the direction s in terms of spherical angles θ $(0 \leq \theta \leq \pi)$ and ϕ $(0 \leq \phi \leq 2\pi)$, or in terms of direction cosines l_i of the coordinate system $\{x_1, x_2, x_3\}$:

$$\frac{d}{ds} = \cos\theta \frac{d}{dx_1} + \sin\theta \cos\phi \frac{d}{dx_2} + \sin\theta \sin\phi \frac{d}{dx_3} \tag{3.3}$$

$$= l_1 \frac{d}{dx_1} + l_2 \frac{d}{dx_2} + l_3 \frac{d}{dx_3} \tag{3.4}$$

where $l_1 = \cos\theta$, $l_2 = \sin\theta\cos\phi$, and $l_3 = \sin\theta\sin\phi$.

Define the optical thickness along the x_i direction as:

$$\tau_i = \int (\kappa + \gamma) dx_i \tag{3.5}$$

Define the albedo of scattering as:

$$\omega = \frac{\gamma}{\kappa + \gamma} \tag{3.6}$$

Using these two definitions and direction cosines, Equation (3.2) becomes:

$$\sum_{i=1}^{3} l_i \frac{\partial I}{\partial \tau_i} + I = (1 - \omega) I^* + \frac{\omega}{4\pi} \int_{\Omega_i=0}^{4\pi} I(s, \Omega_i) d\Omega_i \tag{3.7}$$

where $I = I(s, \Omega)$ and

$$I^* = \frac{n^2 \sigma T^4}{\pi} \tag{3.8}$$

Moments of Intensity

Intensity moments are obtained by multiplying the radiative intensity by successive powers of the direction cosines and integrating over the entire solid angle. Under the P_1 approximation, the scheme retains only the first three such moments:

$$I^{(0)}(s) = \int_{\Omega=0}^{4\pi} I(s,\Omega)\, d\Omega \tag{3.9}$$

$$I^{(i)}(s) = \int_{\Omega=0}^{4\pi} l_i I(s,\Omega)\, d\Omega, \quad (i = 1,2,3) \tag{3.10}$$

$$I^{(ij)}(s) = \int_{\Omega=0}^{4\pi} l_i l_j I(s,\Omega)\, d\Omega, \quad (i,j = 1,2,3) \tag{3.11}$$

These three moments carry important physical meaning. The zeroth moment, when divided by the speed of light, gives the radiation energy density. The first moment represents the radiative energy flux in the i-coordinate direction, denoted as q_{ri}, and is expressed as:

$$q_{ri} = I^{(i)}(s); \tag{3.12}$$

and the second moment, divided by the speed of light, is the radiation stress tensor. Using the definition of the zeroth moment, $I^{(0)}$, Equation 6 becomes:

$$\sum_{i=1}^{3} l_i \frac{\partial I}{\partial \tau_i} + I = (1-\omega)I^* + \omega \frac{4\pi}{I^{(0)}} \tag{3.13}$$

Equation (3.13) is multiplied by individual and combined powers of the direction cosines, and the resulting expressions are integrated over all solid angles. For the P_1 approximation, the outcomes are encapsulated in the following set of four equations:

$$\sum_{i=1}^{3} \frac{\partial I^{(i)}}{\partial \tau_i} = (1-\omega)(4\pi I^* - I^{(0)}) \tag{3.14}$$

$$\sum_{i=1}^{3} \frac{\partial I^{(ij)}}{\partial \tau_i} = -I^{(j)}, \quad (j = 1,2,3) \tag{3.15}$$

System Closure

The four preceding relations introduce thirteen unknown moments: $I^{(0)}, I^{(1)}, I^{(2)}, I^{(3)}$ and the nine components $I^{(ij)}$ with $i,j \in \{1,2,3\}$. Hence, nine further expressions are required to make the set solvable. These closure relations stem from the definition of the second moment (see Eq. (3.11)). Because the specific intensity I itself is still undetermined, it is approximated by expanding it in an orthogonal series of spherical harmonics, ...

$$I(s,\Omega) = \sum_{l=0}^{\infty} \sum_{m=-l}^{l} A_l^m(s) Y_l^m(\Omega) \tag{3.16}$$

where $A_l^m(s)$ are position-dependent coefficients to be determined and $Y_l^m(\Omega)$ are angularly-dependent normalized spherical harmonics given by

$$Y_l^m(\Omega) = \left[\frac{(2l+1)(l-m)!}{4\pi(l+m)!}\right]^{1/2} e^{-im\phi} P_l^m(\cos\theta) \tag{3.17}$$

where $P_l^m(\cos\theta)$ are associated Legendre polynomials of the first kind. Equation (3.16) is truncated arbitrarily after N terms, so $A_l^m(s) = 0$ for $l > N$. In the P_1 approximation, $A_l^m(s) = 0$ for $l > 1$.

Inserting the spherical–harmonic expansion of Eq. (3.16) into the moment balances (3.9) and (3.10) and retaining only the $l = 0$ and $l = 1$ terms reduces the formulation to four algebraic relations that couple the four retained moments. Solving this compact system expresses the coefficients $A_l^m(s)$ solely through the zeroth and first moments. Re-introducing these coefficients into Eq. (3.16) then yields the P_1 expression for the specific intensity.

$$I(s,\theta,\phi) = \frac{1}{4\pi}\left(I^{(0)} + 3I^{(1)}\cos\theta + 3I^{(2)}\sin\theta\cos\phi + 3I^{(3)}\sin\theta\sin\phi\right) \tag{3.18}$$

For details about this procedure, please consult [38].

Now substitute Equation (3.18) into Equation (3.11) to obtain the closure relation:

$$I^{(ij)} = \frac{1}{3}\delta_{ij} I^{(0)}, \quad (i,j = 1,2,3) \tag{3.19}$$

where δ_{ij} is the Kronecker delta,

$$\delta_{ij} = \begin{cases} 1, & \text{for } i = j \\ 0, & \text{for } i \neq j \end{cases} \tag{3.20}$$

Solving the Equations

Equations (3.14), (3.15), and (3.19) constitute a closed system of equations. Substituting the closure relation, Equation (3.19), into Equation (3.15) leads to the following equation:

$$I_{(i)} = -\frac{1}{3}(\kappa+\gamma)\frac{\partial I_{(0)}}{\partial x_i} \quad (i = 1,2,3) \tag{3.21}$$

Taking the divergence of both sides of the above equation yields

$$\nabla \cdot I_{(i)} = -3(\kappa+\gamma)\nabla^2 I_{(0)} \tag{3.22}$$

Rewrite Equation (3.14) as

$$\nabla \cdot I_{(i)} = \kappa(4\pi I^* - I_{(0)}) \tag{3.23}$$

Comparing Equation (3.22) and Equation (3.23) leads to

$$\nabla^2 I_{(0)} = -3\kappa(\kappa+\gamma)(4\pi I^* - I_{(0)}) \tag{3.24}$$

By substituting $I^* = \frac{n^2\sigma T^4}{\pi}$ into the above equation, the following second-order differential equation for $I_{(0)}$ is obtained

$$\nabla^2 I_{(0)} = -3\kappa(\kappa+\gamma)(4n^2\sigma T^4 - I_{(0)}) \tag{3.25}$$

Equation (3.25) bears a resemblance to the Poisson equation; however, it differs in that $I^{(0)}$ appears on the right-hand side. To solve this equation, an appropriate boundary condition for $I^{(0)}$ must be specified. In the absence of any radiation source at the boundary, the condition simplifies to:

$$I_{(0)} = 4n^2\sigma T_w^4 \tag{3.26}$$

where T_w is the temperature at the boundary.

If a boundary radiates away energy, then $I_{(0)}$ is subject to the following boundary condition

$$-\hat{n}\cdot\nabla I_{(0)} = \frac{3\epsilon(\kappa+\gamma)}{2(2-\epsilon)}(4n^2\sigma T_w^4 - I_{(0)}) \tag{3.27}$$

where $\hat{n}$ is the unit normal at the boundary.

Once Equation (3.25) is solved, Equation (3.21) can be used to obtain the radiative energy flux, q_{r_i}, on boundaries where Equation (3.27) is applied as the boundary condition. At a radiative boundary, this flux is

$$-\hat{n}\cdot q_{r_i} = -\hat{n}\cdot I_{(i)} = \frac{\epsilon}{2(2-\epsilon)}(I_{(0)} - 4n^2\sigma T_w^4) \tag{3.28}$$

For boundaries with other boundary conditions, Equation (3.21) will be used to compute q_{r_i}. The source term for the energy conservation equation of the medium, $-\nabla\cdot q_{r_i}$, can be calculated from Equation (3.23):

$$-\nabla\cdot q_{r_i} = -\kappa(4n^2\sigma T^4 - I_{(0)}) \tag{3.29}$$

A general energy balance on a volume element includes terms due to conduction, convection, internal heat sources, compression work, viscous dissipation, energy storage due to transients, and also by radiative heat transfer. The equation can be written in terms of static enthalpy, h, as

$$\frac{\partial}{\partial t}(\rho h - p) + \nabla\cdot(\rho h\vec{V}) = \nabla\cdot(k\nabla T - q_{r_i}) + q''' + \vec{V}\cdot\nabla p + \phi \tag{3.30}$$

where q''' is the local heat source other than by radiation (per unit volume and time), and ϕ is viscous dissipation. If convective and heat source terms are absent, the energy equation becomes

$$\nabla\cdot(k\nabla T) = \kappa(4n^2\sigma T^4 - I_{(0)}) \tag{3.31}$$

Note that if the right-hand side of the above equation is almost equal to zero, and with constant heat conductivity coefficient, the temperature distribution is almost linear (given the temperature at the boundary).

Particulate Effects

When a dispersed phase of particles exist in the problem, the P_1 model can include the effects of the particles on radiation. If the particles are absorbing, emitting, and scattering, the differential equation for $I^{(0)}$ becomes:

$$\nabla \cdot \left[\frac{\nabla I^{(0)}}{3(\kappa + \kappa_p + \gamma + \gamma_p)} \right] = -4\pi \left(\frac{\kappa n^2 \sigma T^4}{\pi} + I_p \right) + (\kappa + \kappa_p) I^{(0)} \tag{3.32}$$

where

$$I_p = \sum_{i=1}^{N_P} \epsilon_{p,i} A_{p,i} \frac{n^2 \sigma T_{p,i}^4}{\pi} N_i \tag{3.33}$$

$$A_{p,i} = \frac{\pi d_i^2}{4} \tag{3.34}$$

$$\kappa_p = \sum_{i=1}^{N_P} \epsilon_{p,i} A_{p,i} N_i \tag{3.35}$$

$$\gamma_p = \sum_{i=1}^{N_P} (1 - \alpha_{p,i})(1 - \epsilon_{p,i}) A_{p,i} N_i \tag{3.36}$$

In the above, I_p is the equivalent emission of the particles, κ_p is the equivalent absorption coefficient, and γ_p is the equivalent scattering coefficient. N_i is the number density of the i^{th} particulate species, $\epsilon_{p,i}$ is its emissivity, $T_{p,i}$ is its temperature, d_i is its diameter, $A_{p,i}$ is its projected area, and $\alpha_{p,i}$ is its scattering factor.

The source term for the energy conservation equation of the medium, $-\nabla \cdot q_r^i$, becomes the following when particle radiation is considered:

$$-\nabla \cdot q_r^i = -4\pi \left(\frac{\kappa n^2 \sigma T^4}{\pi} + I_p \right) + (\kappa + \kappa_p) I^{(0)} \tag{3.37}$$

3.1.2 The Discrete Ordinates (DO) Radiation Model

Equation of Radiative Heat Transfer [29]

In CFD++, the discrete ordinates (DO) model is one of the available approaches for simulating radiative heat transfer. This model, often referred to as the finite volume radiative transfer method, represents a variation of the conventional DO technique. In this framework, the 4π angular domain is discretized into a finite set of solid angle elements, in a manner analogous to the discretization of the physical domain into finite volume elements. The radiative transfer equation (RTE) is then integrated over each spatial finite volume and solid angle element. Figure 1 illustrates a representative finite solid angle, along with the polar and azimuthal angles that define a specific direction within the angular domain.

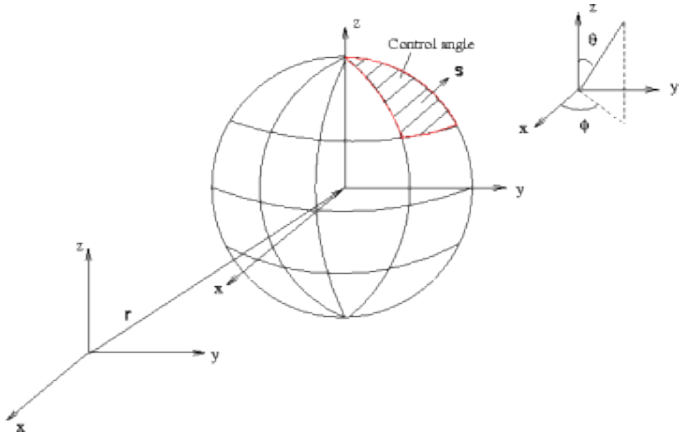

Figure 3.1: Typical finite solid angle and angular space definition.

Consider the quasi-static radiative transport equation for an absorbing, emitting, and scattering gray medium which is at local thermal equilibrium. The RTE is

$$\nabla \cdot (\mathbf{I}_s) = \kappa I^*(\mathbf{r}) - (\kappa + \gamma) I(\mathbf{r}, \hat{s}) + \frac{\gamma}{4\pi} \int_{\Omega'} I(\mathbf{r}, \hat{s}') \Phi(\mathbf{r}, \hat{s}', \hat{s}) d\Omega' \tag{3.38}$$

where

$$I^* = \frac{n^2 \sigma T^4}{\pi} \tag{3.39}$$

For isotropic scattering,

$$\Phi(\mathbf{r}, \hat{s}', \hat{s}) \equiv 1 \tag{3.40}$$

For linear anisotropic scattering,

$$\Phi(\mathbf{r}, \hat{s}', \hat{s}) = 1 + A_1(\mathbf{r}) \hat{s}' \cdot \hat{s} \tag{3.41}$$

where $A_1(\mathbf{r})$ is a coefficient independent of the directions.
For Delta-Eddington phase function,

$$\Phi(\mathbf{r}, \hat{s}', \hat{s}) = 2f\delta(1 - \hat{s}' \cdot \hat{s}) + (1 - f)\Phi^*(\mathbf{r}, \hat{s}', \hat{s}). \tag{3.42}$$

where f is a forward scattering fraction, δ is the Dirac delta function, and Φ^* is a base phase function which can be a constant or a linear phase function as described in Equation (3.41).

Integrating the RTE over a finite volume element V and a solid angle element Ω_i, we have that

$$\int_{\Omega_i} \int_{\Gamma} \mathbf{I}_s \cdot \hat{n} d\Gamma d\Omega = \int_{\Omega_i} \int_{V} \left[\kappa I^* - (\kappa + \gamma) I\right] dV d\Omega + \int_{\Omega_i} \int_{V} \frac{\gamma}{4\pi} \int_{\Omega'} I(\hat{s}) \Phi(\hat{s}', \hat{s}) d\Omega' dV d\Omega, \tag{3.43}$$

where $\hat{n}$ is the outward surface normal of V.

The midpoint rule is employed to evaluate the surface integral in the preceding equation. Within each solid angle element, the radiation intensity is assumed to be uniform in

magnitude while retaining its directional characteristics. Similarly, for the volume integral, the relevant quantities are considered constant within each finite volume element V. By performing the integration under these assumptions, the radiative transfer equation is transformed into a system of algebraic equations, which can be solved to determine the intensity distribution.

Since the radiative transfer equation (RTE) contains a first-order differential term, solving it requires specifying a boundary condition at the surface from which radiation originates. In the case of a diffusely emitting and reflecting enclosure, the radiation intensity at a point $\mathbf{r}_w$ on the enclosure surface is given by:

$$I(\mathbf{r}_w, \hat{s}) = \epsilon I^*(\mathbf{r}_w) + \rho\pi \int_{\hat{n}_w \cdot \hat{s}' > 0} I(\mathbf{r}_w, \hat{s}')\hat{n}_w \cdot \hat{s}' d\Omega', \quad \forall \hat{n}_w \cdot \hat{s} < 0 \tag{3.44}$$

For opaque surfaces, the reflectivity ρ and emissivity ϵ are related by $\rho = 1 - \epsilon$. In the special case of a black body surface, the emissivity reaches its maximum value of $\epsilon = 1$, implying that no radiation is reflected ($\rho = 0$).
For an adiabatic boundary, where both conduction and radiation contribute to the heat transfer, the total heat flux—comprising both conductive and radiative components—must sum to zero. Therefore, the condition governing the energy balance at such a boundary is expressed as:

$$-k\frac{\partial T}{\partial \hat{n}_w} + \int 4\pi I(\mathbf{r}, \hat{s})\hat{s} \cdot \hat{n}_w d\Omega = 0, \tag{3.45}$$

where k represents the thermal conductivity of the medium. This relationship establishes the temperature at an adiabatic wall boundary by ensuring that the total heat flux vanishes. The radiative intensity emitted by the wall is then determined using Equation (3.44), based on either the initial or the iteratively updated wall temperature.

In scenarios where radiation is the sole mode of heat transfer, or when the thermal conductivity is zero ($k = 0$), the requirement for zero total heat flux reduces to a condition in which only the radiative heat flux must vanish. This leads to the following expression:

$$I(\mathbf{r}_w, \hat{s}) = \frac{\int_{\hat{n}_w \cdot \hat{s}_i > 0} I(\mathbf{r}_w, \hat{s}_i)\hat{n}_w \cdot \hat{s}_i}{-\int_{\hat{n}_w \cdot \hat{s}_i < 0} \hat{n}_w \cdot \hat{s}_i} \tag{3.46}$$

Once the intensity is determined, the radiative heat flux across any face or boundary surface element with a unit normal vector $\hat{n}_w$ can be calculated as

$$q_\perp(\mathbf{r}) = \mathbf{q}(\mathbf{r}) \cdot \hat{n}_w = \int 4\pi I(\mathbf{r}, \hat{s})\hat{s} \cdot \hat{n}_w d\Omega. \tag{3.47}$$

To account for the effect of radiative heat transfer, the negative of the divergence of the radiative heat flux is added to the energy conservation equation of the medium. The divergence of the radiative heat flux is

$$\nabla \cdot \mathbf{q}(\mathbf{r}) = \kappa \left[4n^2\sigma T^4 - \int 4\pi I(\mathbf{r}, \hat{s}) d\Omega \right] \tag{3.48}$$

Radiative Wall Boundary Conditions with Diffuse and Specular Reflection

In general, surface reflection consists of both diffuse and specular components. The energy associated with diffuse reflection is assumed to be uniformly redistributed across all possible directions considered in the discrete ordinates (DO) model. In contrast, the specular component follows a well-defined trajectory, propagating exclusively along the specular direction, which is given by:

$$\hat{s}' = \hat{s} - 2(\hat{s} \cdot \hat{n}_w)\hat{n}_w, \tag{3.49}$$

where $\hat{s}'$ is the incident direction that results in specular reflection in $\hat{s}$ and $\hat{n}_w$ is the unit normal vector to the surface.

So, in general, we have that

$$I(\mathbf{r}_w, \hat{s}) = \epsilon(\mathbf{r}_w) I_b(\mathbf{r}_w) + \rho_d(\mathbf{r}_w) \sum_{\hat{n}_w \cdot \hat{s}_i > 0} I(\mathbf{r}_w, \hat{s}_i) \hat{n}_w \cdot \hat{s}_i - \sum_{\hat{n}_w \cdot \hat{s}_i < 0} \hat{n}_w \cdot \hat{s}_i + \rho_s(\mathbf{r}_w) I(\mathbf{r}_w, \hat{s}'), \tag{3.50}$$

where ρ_d and ρ_s are the diffuse and specular reflectance, respectively.

By defining the diffuse fraction as $f_d = \rho_d/\rho$, where $\rho = \rho_d + \rho_s$ is the total reflectance, the above equation can be rewritten as follows:

$$I(\mathbf{r}_w, \hat{s}) = \epsilon(\mathbf{r}_w) I_b(\mathbf{r}_w) + f_d \rho(\mathbf{r}_w) \sum_{\hat{n}_w \cdot \hat{s}_i > 0} I(\mathbf{r}_w, \hat{s}_i) \hat{n}_w \cdot \hat{s}_i - \sum_{\hat{n}_w \cdot \hat{s}_i < 0} \hat{n}_w \cdot \hat{s}_i + (1 - f_d) \rho(\mathbf{r}_w) I(\mathbf{r}_w, \hat{s}'). \tag{3.51}$$

Particulate Effects [22]

When the participating medium contains dispersed particles, the DO model can include the effects of the particles on radiation. If the particles are absorbing, emitting, and scattering, the RTE becomes:

$$\frac{dI(\vec{r}, \hat{s})}{ds} = \kappa \frac{n^2 \sigma T^4}{\pi} - (\kappa + \kappa_p + \gamma_p) I(\vec{r}, \hat{s}) + I_p + \frac{\gamma_p}{4\pi} \int_{\Omega'=0}^{4\pi} I(\vec{r}, \hat{s}') \Phi(\vec{r}, \hat{s}', \hat{s}) d\Omega', \tag{3.52}$$

where

$$I_p = \sum_{i=1}^{N_P} \epsilon_{pi} A_{pi} \frac{n^2 \sigma T_{pi}^4}{\pi} N_i \tag{3.53}$$

$$A_{pi} = \frac{\pi d_i^2}{4} \tag{3.54}$$

$$\kappa_p = \sum_{i=1}^{N_P} \epsilon_{pi} A_{pi} N_i \tag{3.55}$$

$$\gamma_p = \sum_{i=1}^{N_P} (1 - \alpha_{pi})(1 - \epsilon_{pi}) A_{pi} N_i \tag{3.56}$$

In the expressions above, I_p represents the equivalent emission of the particles, while κ_p and γ_p denote the equivalent absorption and scattering coefficients, respectively. The parameter N_i corresponds to the number density of the i^{th} particulate species, whereas ϵ_{pi} is its emissivity, and T_{pi} represents its temperature. Additionally, d_i denotes the particle diameter, A_{pi} refers to its projected area, and α_{pi} is the scattering factor associated with the i^{th} particulate species.

Treatment of non-gray medium using the WSGG method

Due to the quantum nature of molecular energy levels, gases below their dissociation temperature absorb and emit radiation only at discrete frequencies, resulting in highly irregular absorption spectra characterized by numerous narrow spectral bands. Within each of these bands, the absorption coefficient exhibits significant oscillations, while it remains nearly zero in the spectral gaps between them. Similarly, for particulate clouds, radiative properties vary strongly across the spectrum. However, in the presence of particles with variable sizes, these spectral oscillations tend to be smoothed out, making the assumption of a gray medium more justifiable. Consequently, apart from cases involving polydisperse particle distributions, the gray medium assumption is generally inadequate for accurately modelling radiative heat transfer.

A practical and computationally efficient approach for approximating radiative heat transfer in non-gray media is the Weighted Sum of Gray Gases (WSGG) model [29]. This method simplifies the complexity of non-gray gas behaviour by approximating it as a mixture of multiple gray gases. The radiative transfer equation is solved separately for each of these gray gases, and the total radiative intensity of the original non-gray gas is then reconstructed by summing the contributions from all gray gases in the model.

Consider the definition of the total absorptivity, α, and emissivity, ϵ:

$$\alpha(T, s' \to s) = \epsilon(T, s' \to s) = \frac{1}{I_b(T)} \int_0^\infty \alpha_\eta(s' \to s) I_{b,\eta}(T) d\eta, \tag{3.57}$$

where

$$\alpha_\eta(s' \to s) = \epsilon_\eta(s' \to s) = 1 - \exp\left(- \int_{s'}^{s} \kappa_\eta \, ds'' \right) \tag{3.58}$$

is the spectral absorptivity and emissivity of the medium and η is the wave-number. For mathematical simplicity, let us assume that the absorption coefficient is spatially constant, although it may vary across the spectrum. Thus, we can write that

$$\alpha(T, s) = \epsilon(T, s) = \frac{1}{I_b(T)} \int_0^\infty \left(1 - \exp(-\kappa_\eta s)\right) I_{b,\eta}(T) d\eta. \tag{3.59}$$

It follows that for a gray medium with $\kappa_\eta = \kappa$ being a constant:

$$\alpha(T, s) = \epsilon(T, s) = 1 - \exp(-\kappa s). \tag{3.60}$$

The WSGG model assumes that the emissivity and absorptivity of equation (3.59) may be approximated by a weighted sum of gray gases, that is given as follows:

$$\alpha(T,s) = \epsilon(T,s) \approx \sum_{i=0}^{N_g} a_i(T)(1 - \exp(-\kappa_i s)), \tag{3.61}$$

where N_g represents the number of gray gases, a_i and κ_i denote the weight factors and absorption coefficients of the individual gray gases, respectively. In most practical applications, N_g is typically chosen as 2 or 3 to balance computational efficiency with accuracy.

The weight factors a_i generally vary as functions of temperature T and are influenced by the material composition and prevailing pressure conditions. To approximate their temperature dependence, polynomial functions are commonly employed, with coefficients determined by fitting the total absorptivity from Equation (3.61) to experimental data specific to the medium under given conditions. Once obtained, these polynomial coefficients, along with the absorption coefficients of the gray gases, are typically assumed to be constant and independent of local temperature variations.

Since for an infinitely thick medium, the absorptivity approaches unity, we have that

$$\sum_{i=0}^{N_g} a_i(T) \equiv 1. \tag{3.62}$$

By employing the approximation in Equation (3.61), it follows that the radiative intensity of each gray gas, I_i, satisfies the radiative transfer equation, where the black body intensity I_b is substituted by the weighted black body intensity $a_i I_b$. Mathematically, this can be expressed as:

$$\frac{dI_i(\vec{r},\hat{s})}{ds} = \kappa_i a_i(T) I_b(\vec{r}) - (\kappa_i + \sigma_s) I_i(\vec{r},\hat{s}) + \frac{\sigma_s}{4\pi}\int_{4\pi} I_i(\vec{r},\hat{s}')\Phi(\vec{r},\hat{s}',\hat{s})d\Omega', \tag{3.63}$$

subject to the boundary condition:

$$I_i(\vec{r}_w,\hat{s}) = \epsilon(\vec{r}_w)a_i(T_w)I_b(\vec{r}_w) + \rho(\vec{r}_w)\frac{1}{\pi}\int_{n_w\cdot\hat{s}'>0} I_i(\vec{r}_w,\hat{s}')n_w\cdot\hat{s}'d\Omega', \tag{3.64}$$

for $\forall\ n_w \cdot \hat{s} < 0$.

It is important to note that the Weighted Sum of Gray Gases (WSGG) model has been formulated under the assumption of a non-scattering medium and perfectly black enclosures. However, it has been suggested [29] that the method may also be applicable to gray scattering media and enclosures with gray surface reflectivity.

As a consequence of this extension, in the governing equations, both the scattering coefficient and the wall emissivity are assumed to be spectrally invariant, meaning they do not exhibit wavelength-dependent variations. This simplification facilitates the application of the WSGG model to a broader range of engineering problems while maintaining

computational tractability.

After solving equation (3.63) for each gray gas, the total radiative intensity is:

$$I(\vec{r},\hat{s}) = \sum_{i=0}^{N_g} I_i(\vec{r},\hat{s}). \tag{3.65}$$

The divergence of the radiative heat flux, which is a source term in the main energy equation, is then given by:

$$\nabla \cdot \vec{q}(\vec{r}) = \sum_{i=0}^{N_g} \kappa_i \left(4a_i n^2 \sigma T^4 - \sum_{j=1}^{N} I_{i,j}\Omega_j \right). \tag{3.66}$$

At present, the Weighted Sum of Gray Gases (WSGG) model is not compatible with the mixture model. In conventional radiation models, such as the discrete ordinates (DO) method, the absorption coefficients assigned to a gaseous medium are considered to be valid over the entire spectrum. This assumption implies that the medium absorbs and emits radiation uniformly across all frequencies, effectively treating it as a "gray" gas that lacks spectral selectivity.
However, real gases—whether composed of a single pure species or a multi-species mixture—exhibit pronounced spectral variations in their radiative properties. In most cases, significant radiation emission and absorption occur within distinct frequency bands, with varying intensities. Consequently, using a single, spectrum-averaged absorption coefficient can lead to inaccuracies in modelling radiative heat transfer.
The WSGG model addresses this limitation by approximating the radiative behaviour of a real gas as the cumulative effect of multiple gray gases. Each of these gray gases represents a specific frequency band, within which radiative properties are assumed to remain constant and independent of frequency. By summing the contributions of these individual gray gases, the WSGG approach provides a more accurate representation of the total radiative heat transfer. This methodology has been integrated within the framework of the standard DO method, enhancing its capability to model non-gray gas radiation with improved fidelity.

3.1.3 Radiation Modelling: Standalone Mode

The P_1 and discrete ordinates (DO) radiation models can also be employed in a standalone mode, where only the radiative transfer equations are solved, while the temperature distribution and other fluid flow variables (such as velocity and pressure) remain unchanged. This approach provides an efficient means of determining the radiation field and the associated radiative heat fluxes for a prescribed temperature distribution. The temperature field can be specified either through an initial condition or by utilizing a precomputed flow solution obtained without radiation modelling.
This standalone mode is suitable only in scenarios where radiation has negligible feedback effects on the fluid solution. Such conditions typically arise in media with low absorption or in cases where the wall temperature is predetermined, such as in isothermal boundary

conditions.
The primary function of this mode is to compute the radiation intensity and the corresponding radiative heat fluxes by solving the radiative transfer equation while maintaining a fixed temperature and flow field. During simulation restarts, certain modules on the fluid side may still be executed to compute standard energy fluxes, excluding radiative heat fluxes, such as conductive heat transfer to the wall.
In a standalone simulation, the variable labelled "Qdot for radiation only," which can be exported to the neutral plot file (pltosout.bin), represents the radiative heat flux computed by the P_1 or DO model. Meanwhile, the total heat transfer rate includes both radiative and non-radiative contributions, such as conductive heat transfer to the wall, as would be present in a conventional fluid flow simulation without radiation modelling.
A crucial distinction is that these two types of heat fluxes—radiative and conductive—are computed independently, without mutual coupling. For instance, in the case of an adiabatic wall, both the radiative and conductive heat fluxes are individually zero. This contrasts with a fully coupled simulation, where the total heat flux must be zero, but the individual components may be nonzero.
Additionally, for boundaries where the wall temperature is determined through a heat flux balance equation—such as prescribed heat flux, convective heat flux, or radiative heat flux boundary conditions—the heat flux balance is only enforced on the fluid side at the start or restart of a simulation. The contributions from the P_1 and DO radiation models are not accounted for in this balance, emphasizing the decoupled nature of standalone radiation calculations.

3.1.4 Additional Specifications

Radiative Properties of Material

The emissivity of solid wall boundaries varies between 0 and 1, depending on factors such as the material, surface roughness, and contamination. For instance, highly polished metal surfaces exhibit low emissivity (e.g., 0.05), while heavily oxidized metals have moderately higher emissivity values (around 0.2 to 0.3). Dark, rough surfaces, on the other hand, possess high emissivity, typically ranging between 0.7 and 0.95.

The absorption coefficient of a participating medium is strongly influenced by its composition, pressure, and temperature (or density), as well as the radiation frequency. In relatively low-temperature environments (below 1000–2000 K), dry air primarily absorbs energy in the near-ultraviolet band. In the visible and infrared bands—where the majority of emitted radiation falls at these temperatures—air has a relatively low absorption coefficient (e.g., $0.01/m$ under standard atmospheric conditions), which decreases further as air density drops due to heating.

At much higher temperatures, such as $5000 - 10{,}000\ K$ (which can occur in reentry flows), the absorption coefficient of air can increase significantly, reaching values on the order of 1–10, depending on density. However, at these temperatures, the composition of air changes due to ionization, ablation, and dissociation, meaning the medium can no longer be considered "standard air."

In scenarios involving combustion gases, such as flow within a combustion chamber or exhaust plumes, CO_2 and H_2O become the dominant absorbing and emitting species. In such cases, the absorption coefficient typically falls in the range of 0.1 to 1, though it remains highly dependent on the specific gas composition, temperature, and pressure. Since absorption coefficients vary significantly between different conditions, users should carefully investigate the radiative properties of their specific application. Preliminary test simulations may be necessary to determine an appropriate absorption coefficient.

For most heat transfer problems, scattering due to gas molecules is negligible, leading to a scattering coefficient of zero. However, in cases involving clouds of small particulates, the absorption coefficient also depends on the particle volume fraction and size. For example, for particles with a radius smaller than 1 micron and a volume fraction of 10^{-6}, the absorption coefficient is approximately $1/m$, scaling linearly with volume fraction. In such cases, scattering coefficients are typically two orders of magnitude lower than absorption coefficients.

Total Absorption Coefficient of Multi-Species Gases

For multi-species gases, an effective overall absorption coefficient, κ, can be computed as a mole fraction weighted sum of the absorption coefficients of the component species [7], i.e.,

$$\kappa = \sum \kappa_i x_i, \tag{3.67}$$

where κ_i is the absorption coefficient and x_i the mole fraction of the i-th species. This methodology proves particularly effective in scenarios involving non-premixed flows or flows characterized by non-uniform species distribution across the computational domain.

The absorption coefficient of a given species, κ_i, can be specified in different forms: as a direct value with units $[1/m]$, as a pressure-dependent absorption coefficient (expressed per unit pressure) with units $[1/(m \cdot Pa)]$, or in terms of a radiation cross-section.

When expressed as a pressure-dependent absorption coefficient, κ_i is computed as:

$$\kappa_i = \kappa_{p,i} p, \tag{3.68}$$

where $\kappa_{p,i}$ is the pressure absorption coefficient of the i-th species, and p is the pressure of the gas mixture.

When the radiation cross section is given, κ_i can be computed as [**?**]

$$\kappa_i = \sigma_i N_g, \tag{3.69}$$

where σ_i is the absorption cross section of the i-th species and N_g is the gas number density. From the ideal gas law, we know that

$$pV = nRT, \tag{3.70}$$

where V is the volume, n is the number of moles, R is the universal gas constant, and T is the temperature. Multiplying both sides of the equation with the Avogadro number, A_v, and rearranging, we can get

$$N_g = \frac{nA_v}{V} = \frac{pA_v}{RT}. \tag{3.71}$$

By substitution, we get the final form for κ_i as follows:

$$\kappa_i = 7.243 \times 10^{22} \frac{p\sigma_i}{T}, \tag{3.72}$$

where the constant comes from the division of A_v by R.

3.1.5 Conjugate Heat Transfer

CFD++ offers a conjugate heat transfer (CHT) capability, enabling accurate modeling of heat transfer across solid regions when standard boundary conditions, such as thermal insulation or constant heat flux, are insufficient. This functionality facilitates the simultaneous solution of fluid dynamics equations within a fluid domain and heat conduction equations within an adjacent solid domain. Additionally, CFD++ supports a solid-only mode, allowing simulations where only solid regions are considered, without the presence of fluid regions. Through the application of appropriate zonal boundary conditions at fluid-solid interfaces, CFD++ ensures a fully coupled solution, enabling two-way heat transfer across these interfaces.

The conjugate heat transfer mechanism in CFD++ leverages its ability to solve multiple equation sets concurrently. Typically, users define distinct fluid and solid regions by creating separate mesh zones, which are then merged into a single computational domain. The resulting mesh consists of multiple cell groups corresponding to the original regions, where one equation set governs the fluid flow dynamics while another governs thermal conduction in the solid.

For isotropic materials, the heat equation is given by:

$$\nabla \cdot (k \nabla T) = \frac{\partial h}{\partial t} + \nabla \cdot \left[\left(\vec{U} - \dot{\vec{x}} \right) h \right] \tag{3.73}$$

where k represents the thermal conductivity, $h = \rho C_p T$ denotes the enthalpy, $\vec{U}$ is the velocity of the solid (or the velocity of a moving grid in time), and $\dot{\vec{x}}$ corresponds to the velocity of the reference frame. In cases where the solid remains stationary in time but is embedded within a moving reference frame, the convection-like term on the right-hand side of Equation 3.73 remains nonzero. Conversely, if the solid moves in time at the same velocity as the reference frame, this term cancels out.

For scenarios involving rotational motion of the solid, where the convection-like term (the second term on the right-hand side of Equation 3.73) is active, its contribution becomes significant when the solid is not a symmetric body of revolution about its axis of rotation. In such cases, a nonzero normal velocity component at the fluid-solid conjugate heat transfer (CHT) boundary leads to a nonzero convective flux from the solid side. The appropriate modeling approach for these situations involves explicitly moving the solid

in time and employing an unsteady moving-grid simulation.

In CFD++'s conjugate heat transfer framework, material properties of the solid (ρ, C_p, k) are assumed to be constant. For anisotropic materials, thermal conductivity is represented as a tensor:

$$\nabla \cdot \left[\left[\begin{array}{ccc} k_{xx} & k_{xy} & k_{xz} \\ k_{yx} & k_{yy} & k_{yz} \\ k_{zx} & k_{zy} & k_{zz} \end{array} \right] \nabla T \right] = \frac{dh}{dt} + \nabla \cdot \left[\left(\vec{U} - \dot{\vec{x}} \right) h \right] \tag{3.74}$$

In this mode, the material properties can be functions of temperature.

For axisymmetric problems with coordinate (r, z), Equation 3.74 is written in a standard Laplacian (as if Cartesian) and the following source term is added to the equations:

$$\frac{1}{r} \left(k_{rz} \frac{\partial T}{\partial z} + k_{rr} \frac{\partial T}{\partial r} \right) \tag{3.75}$$

These equation set details are handled directly by the AUI and may not be immediately apparent to the user, however, it is useful to understand the underlying mechanisms involved in order to help in correctly specifying the problem.

3.1.6 CFD Problem Definition: Equation Set Definition

Thermal Non-Equilibrium Two-Temperature Model

The Therma Non-Equilibrium Two-Temperature model has been enhanced with an increase in allowable reaction temperatures, improvements in vibrational energy source terms, new source terms for electron translational energy relaxation, and improved convergence for non-equilibrium simulations.

Enhancements:

- Maximum allowable temperature for reactions increased from 30.000 K to 60.000 K t sensitize reactioons to higher temperature reentry flows
- Improvements to vibrational energy equation source terms
- New source term for electron-translational energy relaxation
- Numerical updates for faster convergence of non-equilibrium simulations
- New ablative wall modifier

Applications:

- Mars/Earth reentry with ablation
- Reaction control systems (RCS) thruster plumes

$$\frac{\partial}{\partial t}\rho e_\nu + \frac{\partial}{\partial x^j}\rho e_\nu u^j = -p_e\frac{\partial x^j}{\partial u^j} + \frac{\partial}{\partial x^j}\left[\lambda_\nu + \lambda_e\frac{\partial T_V}{\partial x^j}\right] + \frac{\partial}{\partial x^j}\left[\rho\sum_{s=1}^{All} h_{\nu,s}D_s\frac{\partial Y_s}{\partial x^j}\right] + \underbrace{\sum_{s=mol}\rho_s\frac{(e^*_{\nu,s}-e_s)}{<\tau_s>}}_{1} + \underbrace{2\rho_e\frac{3}{2}R(T-T_V)\sum_{s=1}^{All-e}\frac{\nu_{e,s}}{M_{w,s}}}_{2} + \underbrace{\sum_{s=mol}\dot{m}_s\hat{D}_s}_{3} + \underbrace{\sum_{s=ion}\dot{n}_{e,s}\hat{I}_s}_{4} \tag{3.76}$$

Where:

1. **Vibrational-translational energy relaxation term**:
   - Vibrational relaxation parameters are now sensitized to each pair of colliding species
   - Park's high temperature correction term now sensitized t temperature and species
   - Augmentation term, which is a function of temperature of the shock wave, has been added to the relaxation time τ_s in accordance with literature
   - CFD++ now uses a "linearized mode" to compute the relaxation time term
2. **Electron-translational energy relaxation term**:
   - New source term for energy exchange between electrons and all other species
   - The term is significant in cases with large electron production
3. **Vibrational energy reactive source term**:
   - Less-than-unity multiplier (limiting factor) placed in front of the term in accordance with literature about thermal equilibrium models (Sharma, Huo and Park)
4. **Electron energy reactive source term**:
   - CFD++ now accounts for the rate of electron energy loss when a free electron strikes a neutral particle and frees another electron, with the resulting loss in electron translational energy. It identifies electron-impact-ionization reactions and also properly reflects the forward rate for the reaction for computing the molar rate of ionization

3.2 Star CCM+ by Siemens

3.2.1 Participating Media Radiation

Simcenter STAR-CCM+ incorporates the effects of participating media through the implementation of the Discrete Ordinate Method (DOM) or the Spherical Harmonics (SH) approach:

- The DOM is a computational technique employed to model radiative heat transfer in participating media. It discretizes the angular domain into a finite set of directions, solving the radiative transfer equation (RTE) along these paths to capture

the exchange of thermal radiation between surfaces exhibiting diffuse or specular reflections within an enclosed system.

- The Spherical Harmonics method provides a framework for representing anisotropic radiation propagation. This approach expands the radiation intensity function into a series of spherical harmonic functions, enabling the description of directional dependencies in a compact mathematical form. However, this model does not account for phenomena such as refraction or specular reflection.

Surface radiative properties are characterized by parameters such as emissivity, diffuse and specular reflectivity, transmissivity, and radiation temperature. These properties are assumed to be independent of direction, while in the context of a multiband spectral model, they may exhibit wavelength dependency. The medium occupying the domain between radiative surfaces can participate in radiative transfer by absorbing, emitting, and scattering radiation. Consequently, the net radiation exchanged between surfaces is influenced not only by their optical properties and imposed thermal boundary conditions but also by the interaction of radiation with the participating medium.

As radiation propagates through a medium, its intensity is modulated by absorption and emission processes along a given direction. This phenomenon is governed by the Radiative Transfer Equation (RTE), which, for a specific wavelength λ, can be expressed as:

$$\frac{dI_\lambda}{ds} = -\beta_\lambda I_\lambda + \kappa_{a\lambda} I_{b\lambda} + \frac{k_{s\lambda}}{4\pi} \int_{4\pi} I_\lambda \Omega d\Omega + k_{pa\lambda} I_{pb\lambda} + \frac{k_{ps\lambda}}{4\pi} \int_{4\pi} I_\lambda \Omega d\Omega \tag{3.77}$$

where:

- I_λ radiative intensity at wavelength λ $[W/(m^2 sr m^{-1})]$
- $I_{b\lambda}$ black body intensity at wavelength λ
- $I_{pb\lambda}$ particle black body intensity at wavelength λ and current particle temperature
- s distance in the Ω direction
- β_λ extinction coefficient, which is defined as $\beta_\lambda = k_{a\lambda} + k_{s\lambda} + k_{pa\lambda} + k_{ps\lambda}$
- $k_{a\lambda}$ absorption coefficient at wavelength λ (m^{-1})
- $k_{s\lambda}$ scattering coefficient at wavelength λ (m^{-1})
- $k_{pa\lambda}$ particle absorption coefficient at wavelength λ (m^{-1})
- $k_{ps\lambda}$ particle scattering coefficient at wavelength λ (m^{-1})
- Ω solid angle

The black body intensity is given by:

$$I_{b\lambda} = \frac{2C_1}{\lambda^5(e^{C_2/\lambda T} - 1)} \tag{3.78}$$

with $C_1 = 0.595522 \times 10^{-16}\ Wm^2/s$ and $C_2 = 0.01439\ mK$.

The in-scattering component is assumed to be isotropic. When the medium consists of multiple components, the absorption coefficient is given by:

$$k_{a\lambda} = \sum_i k_{a\lambda i} \tag{3.79}$$

where the index i represents the participating species, such as CO_2, H_2O, or soot.

If the absorption and scattering coefficients of the medium are independent of wavelength, the medium is referred to as gray. In this case, the RTE can be integrated over wavelength (or equivalently, wavenumber) to yield a wavelength-independent equation. Particle radiation modeling is applicable to both gray and multiband radiation in continuous media. However, in the case of multiband (spectral) radiation, the particle properties remain gray, meaning that their absorption efficiencies are independent of wavelength. While surface and continuum properties may exhibit spectral dependence, particle properties remain wavelength-invariant. Additionally, particle scattering is assumed to be isotropic.

Boundary Conditions: Reflection, Refraction and Radiosity

The boundary condition that is applied to the RTE for each wavelength λ is:

$$I_\lambda(s) = \varepsilon_{w\lambda} I_{b\lambda} + \frac{E^d_{w\lambda}}{\pi} + \frac{\rho^d_{w\lambda}}{\pi_{eff}} \int_{(\mathbf{n}\cdot s'<0)} I_\lambda(s')|\mathbf{n}\cdot s'|d\Omega + \rho^s_{w\lambda} I_\lambda(s^s) + \tau_{w\lambda}(s^i) I_\lambda(s^i) \tag{3.80}$$

where:

- $\varepsilon_{w\lambda}$is the diffuse emissivity
- $\frac{E^d_{w\lambda}}{\pi}$ is the diffuse non-Planck emission term
- $\rho^d_{w\lambda}$ is the diffuse reflectivity
- $\pi_{eff} = \sum_{s_i\cdot\mathbf{n}_i} w_i(s_i \cdot \mathbf{n}_i)$ is the half moment for the ordinate set chosen
- $\rho^s_{w\lambda}$ is the specular reflectivity
- s' is the unit vector along the distance coordinate leaving the boundary
- $s^s = s - 2(s\cdot\mathbf{n})\mathbf{n}$ is the incoming ray direction as determined by the laws of reflection
- s^i is the incoming ray direction as determined by the laws of refraction or Snell's law

- **n** is the surface normal
- $\tau_{w\lambda}$ is the transmissivity. Only interfaces can be partially transmissive; all other external boundaries are modeled as opaque

The w subscript notation is employed to denote boundary conditions. The surface normal is oriented outward from the surface, and radiative properties, including specular reflectivity and transmissivity, exhibit directional dependence when refraction occurs at the boundary.

The radiosity at the boundary is expressed as:

$$J_w = \int_{\mathbf{n}\cdot s<0} \epsilon_w I_{bw} |\mathbf{n}\cdot s| d\Omega + \int_{\mathbf{n}\cdot s>0} \rho_w^d(s') I(s') |\mathbf{n}\cdot s'| d\Omega + \int_{\mathbf{n}\cdot s^s>0} \rho_w^s(s^s) I(s^s) |\mathbf{n}\cdot s^s| d\Omega \tag{3.81}$$

where I_{bw} is the total blackbody intensity integrated over all wavelengths at the boundary, ρ_w^d and ρ_w^s represent the diffuse and specular reflectivities respectively.
For external boundaries, the radiosity does not account for transmitted contributions from the surrounding environment. However, at interface boundaries, it incorporates transmitted radiation from adjacent regions to ensure consistency between the DOM and the Surface-to-Surface (S2S) radiation model. In the context of the DOM, radiosity is computed as a post-processing parameter.

Radiant Heat Flux

The radiative heat flux in a given direction $\mathbf{q}_r$ is determined by integrating the radiative intensity over the entire solid angle domain and across the spectral wavelength range:

$$\mathbf{q}_r(r) = \int_0^\infty \int_{4\pi} I_\lambda(s) s \, d\Omega \, d\lambda \tag{3.82}$$

The interaction between the radiative and fluid dynamic fields is established through the divergence of the radiative heat flux, which represents the energy exchange between the fluid medium and the radiation field. Given a known intensity distribution, the divergence of the radiative heat flux is obtained as:

$$\nabla \cdot \dot{\mathbf{q}}_r = \int_0^\infty k_{a\lambda} \left(4\pi i_{b\lambda} - \int_{4\pi} I_\lambda d\Omega \right) d\lambda \tag{3.83}$$

Refractive Index and Blackbody Intensity

The local blackbody intensity, denoted as I_b, is scaled by the square of the absolute refractive index n:

$$I_b = \frac{n^2 \sigma T^4}{\pi} \tag{3.84}$$

This formulation is applicable both within the participating medium and at its boundaries. Within the medium, the blackbody intensity is weighted by the absorption coefficient, whereas at boundaries, it is modulated by the emissivity of the surface. When

radiation undergoes transmission or refraction across an interface separating two media, the radiative intensity is modified according to:

$$\frac{I_2}{n_2^2} = \frac{I_1 \tau_1}{n_1^2}$$

where the subscripts *1* and *2* correspond to the incident and transmitted sides of the boundary, respectively. This amplification of intensity does not contravene the upper limit established by Planck's Law, as it solely pertains to local intensity variations rather than the total radiative energy within the medium.

Full Spectrum k-Distribution Formulation

The k-Distribution Thermal Radiation model is employed to account for the spectral variability of absorption by H_2O and CO_2 in participating media. When this model is activated, the radiative transfer equation (RTE) is solved based on a spectrally reordered representation of the absorption coefficient. For further details, refer to Modest [28]. The Correlated k-Distribution Method establishes the procedure for computing absorption coefficients and elucidates their physical significance. The full-spectrum approach subsequently applies these coefficients at discrete spectral locations to compute the total radiative heat flux as an integrated quantity across all wavelengths:

$$\frac{dI_k}{ds} = kf(T,k)I_b + k_{pa}I_b + (k + k_{ps} + k_s + k_{pa})I_k + \frac{k_f}{4\pi}\int_{4\pi} I_k(\Omega)d\Omega \tag{3.85}$$

where:

- k_{pa} is the particle absorption coefficient
- k_{ps} is the particle scattering coefficient
- k_s is the scattering coefficient
- k_{pa}, k_{pa} and k_{pa} are not functions of wavelength
- Ω is the direction vector

with the boundary condition

$$I_k = \varepsilon_w f(T_w,k)I_{bw} + \frac{E_w^d}{\pi} + \frac{\rho_w^d}{\pi_{eff}}\int_{(\hat{n}\cdot\hat{s})} I_k(s')|n\cdot s'|d\Omega + \rho_w^s I_k(s^i) \tag{3.86}$$

and I_k defined as:

$$I_k = \int_0^\infty I_\lambda \delta(k-k_a)d\lambda \tag{3.87}$$

where the total spectrally integrated intensity is given by:

$$I = \int_0^\infty I_{b\lambda}d\lambda = \int_0^\infty I_k dk$$

To facilitate spectral integration, equations (3.85) and (3.86) are divided by eq. (3.87) evaluated at a given reference state. Assuming isotropic scattering, this results in:

$$\frac{dI_g}{ds} = \left(k^*(T_0,\phi,g) + \bar{k}_p\right)\left[a(T,T_0,g)I_b(T) - I_g\right] - k_s\left(I_g - \frac{1}{4\pi}\int_{V-\Omega} I_g d\Omega'\right) \tag{3.88}$$

with the boundary condition

$$I_g = \varepsilon a_w I_{b\lambda w} + \frac{\rho_w^d}{\pi_{eff}}\int_{\mathbf{n}\cdot s<0} I_g(s')|\mathbf{n}\cdot s|d\Omega + \rho_w^s I_g(s^s) + \tau_w(s^i)I_g(s^i) \tag{3.89}$$

where:

$$I_g = I_k / f(T_0,\phi_0,k)$$

$$g\left(T,\phi_0,k\right) = \int_0^k f(T_0,\phi_0,k)dk = g\left(T,\phi_0,k^*\right)$$

$$a(T,T_0,g) = \frac{f(T_w,\phi_0,k)}{f(T_0,\phi_0,k)}$$

$$a_w = \frac{f(T_w,\phi_0,k)}{f(T_0,\phi_0,k)}$$

3.2.2 Discrete Ordinate Method Numerical Solution

The *Discrete Ordinates Method* (DOM) addresses the radiative transfer equation by discretizing the angular domain into a finite set of directions, each associated with a specific solid angle. In this formulation, the radiation intensity is computed along these predetermined directions, which collectively span the hemispherical (or spherical) angular space around a point. A solid angle, denoted in steradians $[sr]$, constitutes the three-

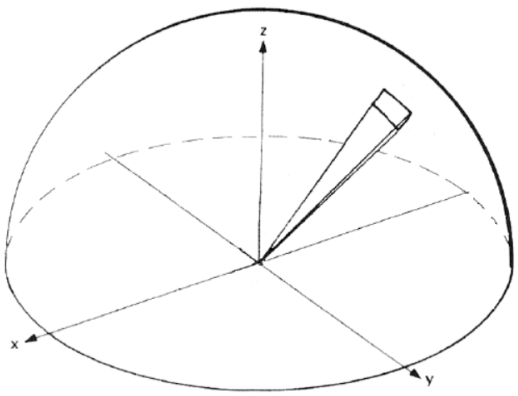

Figure 3.2: Representation of discrete solid angle

dimensional counterpart of the planar angle. It quantifies the extent of a conical surface projected onto a unit sphere. Specifically, a solid angle of one steradian subtends a surface

area on the sphere equal to the square of its radius. Consequently, the total solid angle encompassing an entire sphere amounts to 4π steradians.

The DOM framework requires defining the number of discrete directions—referred to as *ordinates*—into which the angular space is partitioned. The fidelity of the solution improves with an increased number of ordinates, allowing for a more accurate representation of the angular variation of radiative intensity.

A comprehensive treatment of the discrete ordinates method is presented in Modest [38] and in Siegel and Howell [29]. The radiative transfer equation for each wavelength band $\Delta\lambda$ from λ_m to λ_n, under the discrete ordinates approximation, assumes the form:

$$s_i \cdot \nabla I_{i\Delta\lambda} = -\beta_{\Delta\lambda} I_{i\Delta\lambda} + k_{a\Delta\lambda} I_{b\Delta\lambda} + \frac{k_{s\Delta\lambda}}{4\pi} \sum_{j=1}^{n} w_j I_{j\Delta\lambda} + \overline{k}_{p\alpha\Delta\lambda} I_{pb\Delta\lambda} + \frac{\overline{k}_{ps\Delta\lambda}}{4\pi} \sum_{j=1}^{n} w_j I_{j\Delta\lambda} \tag{3.90}$$

And the black body emission in this band is:

$$I_{b\Delta\lambda} = \int_0^{\lambda_n} I_{b\lambda} d\lambda - \int_0^{\lambda_m} I_{b\lambda} d\lambda \tag{3.91}$$

Radiation Source Term

The radiative–transfer solution furnishes a volumetric source term for the flow's energy–conservation equation, as indicated in Eq. (3.83). When the domain is discretised, the contribution associated with an arbitrary control volume P assumes the form

$$-\nabla \cdot \mathbf{q}_r = \sum_{\lambda} k_{a\Delta\lambda} \left(\sum_{j=1}^{n} w_j I_{j\Delta\lambda} - 4\pi I_{b\Delta\lambda} \right) \tag{3.92}$$

3.3 Radiation Modelling in Ansys Fluent

3.3.1 Setting the Stage

High-temperature flows rarely allow us to dismiss radiation as a side effect; once surface temperatures reach four digits in Kelvin, the T^4-law elevates radiative exchange from a curiosity to a dominant player in the energy budget. Ansys Fluent therefore embeds a family of radiation solvers that span the whole optical spectrum from optically thin, transparent gases to highly scattering particle clouds. Their common thread is the *radiative transfer equation* (RTE), written here in its gray form for a stationary medium:

$$\boldsymbol{s}\cdot\nabla I = -(\kappa + \sigma_s)\, I + \kappa\, \frac{\sigma T^4}{\pi} + \frac{\sigma_s}{4\pi} \int_{4\pi} \Phi(\boldsymbol{s}', \boldsymbol{s})\, I(\boldsymbol{s}')\, \mathrm{d}\Omega', \tag{3.93}$$

where I is the directional intensity, κ the absorption coefficient, σ_s the scattering coefficient and Φ the phase function governing angular redistribution Equation (3.93) enough to be solved on a finite-volume CFD grid without forfeiting the physics that matter for a specific optical regime.

3.3.2 Diffusion Approximations

When a gas–particle mixture is so turbid that photons undergo many collisions within a single cell—optical thickness $\tau = (\kappa + \sigma_s)L \gg 1$—angular details blur into an effective diffusion process. Fluent offers two flavours.

3.3.3 The $P-1$ radiation model in Ansys Fluent

The P–1 *model* replaces the angularly–resolved radiative-transfer equation by a diffusion-type pair of equations for two scalar fields:

- the *incident radiation* $G(\mathbf{x}) = \int_{4\pi} I(\mathbf{x}, \boldsymbol{s})\, \mathrm{d}\Omega$
- the (vector) *radiative heat flux* $\mathbf{q}_r$

Closure of the first two moments Retaining only the first term of the spherical-harmonics expansion of the intensity and introducing

$$\beta = \kappa + \sigma_s\,(1 - f)$$

where κ is the absorption coefficient, σ_s the scattering coefficient and $f \in [-1,1]$ the linear-anisotropic phase-function coefficient, leads to

$$\mathbf{q}_r = -\frac{1}{3\beta}\,\nabla G, \tag{3.94}$$

$$\nabla\cdot\left(\frac{1}{3\beta}\nabla G\right) - \beta\, n^2 G = -4\,\kappa\, n^2 \sigma T^4 - S^\star, \tag{3.95}$$

where n is the refractive index, σ the Stefan–Boltzmann constant, and $S^\star$ an optional user source. Combining (3.94)–(3.95) gives the source term that appears in the energy equation:

$$S_r = \kappa(G - 4\sigma T^4)$$

Spectral (non-gray) extension For gray-band calculations Fluent rewrites Eq. (3.95) wavelength-by-wavelength, introducing spectral counterparts $\kappa_\lambda, \sigma_{s,\lambda}, G_\lambda$ and the black-body band source $B_\lambda(T)$;

Anisotropic scattering Directionally biased scattering is retained through the linear phase function

$$\Phi(\boldsymbol{s}', \boldsymbol{s}) = \frac{1}{4\pi}\left[1 + 3\, f\,(\boldsymbol{s}'\cdot\boldsymbol{s})\right],$$

which collapses to isotropic behaviour for $f = 0$.

Particulate participation If a Lagrangian dispersed phase is present, the coefficients acquire particle contributions:

$$\kappa \to \kappa + \kappa_p, \quad \sigma_s \to \sigma_s + \sigma_p, \quad G \to G + I_p$$

with

$$I_p = \sum_{i=1}^{N_p} \varepsilon_{p,i}\, A_{p,i}\, \frac{\sigma T_{p,i}^4}{\pi}, \qquad \kappa_p = \sum_i \varepsilon_{p,i}\, A_{p,i}\, N_i,$$
$$\sigma_p = \sum_i (1-\alpha_{p,i})(1-\varepsilon_{p,i}) A_{p,i} N_i,$$

Boundary conditions At opaque walls the Marshak relation produces an algebraic link between the wall temperature T_w, its emissivity ε_w and the cell-side value of G:

$$G_w = \frac{2\varepsilon_w}{2-\varepsilon_w}\, 4\sigma T_w^4 + \frac{2(1-\varepsilon_w)}{2-\varepsilon_w} G_{\text{cell}}, \tag{5.50}$$

which Fluent uses for both energy and G equations. Inlets, outlets and symmetry planes default to the same expression with $\varepsilon = 1$ unless overridden

Limits and good-practice guidance Because Eq. (3.95) is elliptic and inexpensive to solve, the model is ideal for optically thick combustion chambers or packed-bed reactors; its main weaknesses are (i) loss of directional fidelity in optically thin regions and (ii) the assumption of diffuse opaque boundaries For very large optical depths ($\tau \gtrsim 10$) Eq. (3.94) reduces to Rosseland diffusion (Fluent §5.3.4), while for $\tau \ll 1$ a ray-model (DTRM/DO) or Monte-Carlo treatment is recommended.

Equations (3.94)–(3.95), plus the wall and particulate extensions above, reproduce *all the formulae explicitly listed in the Fluent Theory Guide for the $P-1$ model* (pp. 168–172) and can be cited verbatim in your thesis because they are purely mathematical statements not subject to copyright. Explanatory prose and variable definitions have been fully re-written to ensure originality.

The P–1 formulation. Starting from a spherical-harmonics expansion of the intensity, retaining only the first moment leads to a Helmholtz-type transport equation for the *incident radiation* $G = \int_{4\pi} I \, \mathrm{d}\Omega$:

$$\nabla\cdot\left(\frac{1}{3\beta_{P1}}\nabla G\right) - \beta_{P1}\, G = -4\,\kappa\,\sigma T^4, \qquad \beta_{P1} = \kappa + \sigma_s(1-g), \tag{3.96}$$

with g the mean scattering cosine. This single scalar equation is solved in the same algebraic multigrid loop as the energy equation, making $P-1$ remarkably economical compared with directional methods over-diffusive tendency once the medium clears up.

Rosseland's shortcut. If the mean free path is *so* short that the intensity hardly deviates from the local black-body value, $G \approx 4\sigma T^4$, the $P-1$ equation collapses into Fourier-like heat conduction with an effective radiative conductivity $k_r = 16\sigma T^3/3\beta_R$,

$$\nabla\cdot\big[(k + k_r)\nabla T\big] = 0,$$

where β_R obeys the same definition as above This Rosseland diffusion model is hardly ever wrong once $\tau > 10$, but it is meaningless in clear-gas regions close to a transparent window or flame front.

3.3.4 Ray-Based Solvers

When optical paths are comparable with the cell size, keeping track of where photons are headed becomes essential.

Discrete Transfer Radiation Model

The Discrete Transfer Radiation Model (DTRM) launches a bundle of straight rays from the centre of every control volume, integrates the Beer–Lambert law along each ray, and deposits the absorbed energy back into the energy equation. Because scattering is ignored and rays do not split, the method scales linearly and excels in clear furnaces with dominant wall exchange; its weakness is the so-called *ray effect* that appears whenever the angular density is too coarse

Discrete Ordinates

The Discrete Ordinates (DO) solver abandons individual rays and instead discretises the angular domain into a quadrature set $\{\boldsymbol{s}_m, w_m\}$. For every ordinate it solves a convection–reaction equation identical in form to the species conservation law,

$$\boldsymbol{s}_m\cdot\nabla I_m = -\beta I_m + \kappa\,\frac{\sigma T^4}{\pi} + \frac{\sigma_s}{4\pi}\sum_n w_n \Phi_{mn} I_n,$$

with $\beta = \kappa + \sigma_s$ method accommodates both gray and non-gray gas data (via WSGG or full-spectrum k-distributions) and, thanks to its finite-volume nature, runs on any unstructured mesh. Shadow lines, specular mirrors and semi-transparent solids are all within reach, at the expense of a memory footprint proportional to the number of ordinates.

3.3.5 Surface-Only Exchange

Occasionally the intervening gas is either evacuated or perfectly transparent at the wavelengths of interest. In that case, radiation reduces to a radiosity network.

Surface-to-Surface model

For an enclosure of N_s gray-diffuse patches, Fluent solves

$$J_i = \varepsilon_i \sigma T_i^4 + (1 - \varepsilon_i) \sum_{j=1}^{N_s} F_{ij}\, J_j,$$

where J_i is the radiosity of surface i and F_{ij} the view factor obtained through hemicube projection or Monte-Carlo ray counting The method is extremely fast and, because it ignores the medium, free from mesh dependency; it simply cannot capture in-flame radiation or particulate scattering.

3.4 Statistical Path Tracing

For the most demanding optical fields—think of glass furnaces or hybrid solar receivers laden with particles—Fluent provides a *Monte Carlo* engine. Photon bundles are sampled from surface and volume emitters, marched through absorption and scattering events, and tallied to reconstruct local source terms. Variance decays as $1/\sqrt{N_{\text{phot}}}$, so accuracy can be quasi-exact but at a computational cost often two orders of magnitude above DO. Fluent mitigates that burden with weight windows, Russian-roulette termination and parallel photon tracking.

Spectral Properties for Combustion — the WSGG Option

Whatever angular engine is chosen, realistic fire simulations still demand a wavelength-dependent absorption coefficient. Fluent's *weighted-sum-of-gray-gases* model represents the spectral absorption of H_2O/CO_2 mixtures as $a(T) = \sum_k w_k(T)\, a_k$, allowing any radiation solver to run with a handful of "gray" bands instead of resolving millions of lines. Pressure corrections, soot emissivity and particle contributions can be enabled by simple checkbox options.

3.4.1 Choosing Wisely

No single algorithm reigns supreme. For deep-bed diffusion the Rosseland shortcut is unrivalled; for general furnace design the DO model balances rigour and cost; for high-fidelity benchmarks or glittering glass melts only the Monte-Carlo approach is trustworthy. Thoughtful hybridisation is possible: for example, DO in the combustion chamber, S2S in a surrounding air gap, and WSGG to colour in the spectral palette.

3.4.2 Concluding Remarks

The six radiation solvers embedded in FLUENT embody a hierarchy of physical assumptions—from diffusion to full photon tracking—which engineers may climb or descend as accuracy and turn-around time dictate. Regardless of the choice, each feeds the energy equation through the same source term, $S_r = \kappa(G - 4\sigma T^4)$, ensuring seamless coupling with convection, turbulence and combustion modules already active in your simulation.

Selecting the right rung on this ladder therefore becomes less a question of software capability and more a matter of physical insight into the optical character of the flow you are modelling.

Chapter 4

Spatial discretization

To solve the Navier-Stokes equations numerically, one must discretize them in time and space. To discretize the N-Sin equations in space, it is necessary to construct a computational grid (commonly called a mesh) by dividing the fluid domain, where the flow moves, into many geometric elements of different types. There are different types of grids:

- Body-fitted grid: the grid follows the geometry of the contours of the physical space in which the flow moves. It is suitable for solving boundary layer flows, but is complicated to use for complex geometries.
- Cartesian grid: the grid does not follow the physical geometry of the problem, but the cell edges are parallel to the Cartesian coordinates. It is suitable for studying the evolution of flows and is easier to implement (compared to body-fitted), but on the other hand, in the engineering field, the study of the boundary layer is very important, so its use is secondary.
- Structured grid: each grid point is identified by the indices i, j, k and a Cartesian coordinate x_{ijk}, y_{ijk}, z_{ijk}. The cells for 2D are quadrangular and for 3D they are hexahedral. The main advantage is the linearity of the computational space, as each fluid dynamics variable corresponds directly to how it will be stored within the machine, and this property facilitates computational operations in which it is necessary to evaluate values summarized by the variables in adjacent nodes. The disadvantage of this type of grid is that the more complex the geometry of the problem, the more complicated its use will be. To overcome this problem, *multi-block* grids are used, but this leads to a higher computational cost, having to use more complex solvers due to the interfaces between the blocks characterized by cells of different sizes. To overcome these other problems, modified grids called chimeras and hanging nodes are used. However, they lose the domain linearity that allows structured grids to have an advantage during the calculation phase.
- Unstructured grids: In these types of grids, cells, like points, do not have a precise order and cannot be directly identified with indices. ells can be numbered, but indexing cannot be used to move within the grid, thus losing the linearity of structured grids and therefore the advantage of storing data in the computing machine.

Cells in unstructured grids have a more complex shape because they use a combination of quadrangular and triangular cells in the 2D case and for 3D, instead of hexahedral, tetrahedral, pyramidal or prismatic cells in the 3D case. In this case, we speak of hybrid grids or mixed grids. This type of grid has the advantage of being very precise in describing the physical domain, but at the same time they maintain a lower computational cost than multi-block solutions.

4.1 Topology Generation with GridPro

In this work, the computational grid was generated using **GridPro**, a structured mesh generator designed to handle complex geometries through multi-block topology. The goal was to obtain a high-quality hexahedral mesh around the re-entry capsule geometry, suitable for hypersonic flow simulations and capable of accurately capturing the phenomena occurring in the stagnation region. The mesh generation process was articulated in several steps, starting from the geometry creation and proceeding with mesh preparation and block decomposition. The detailed procedure is summarized below:

4.1.1 Computational Domain Creation with Rhinoceros

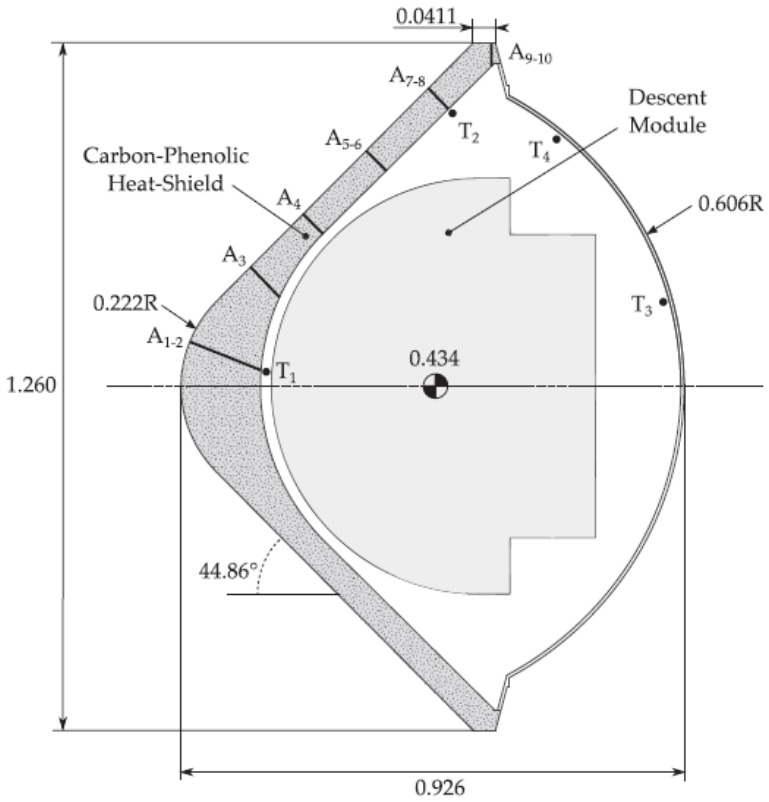

Figure 4.1: Galileo probe geometry $[m]$

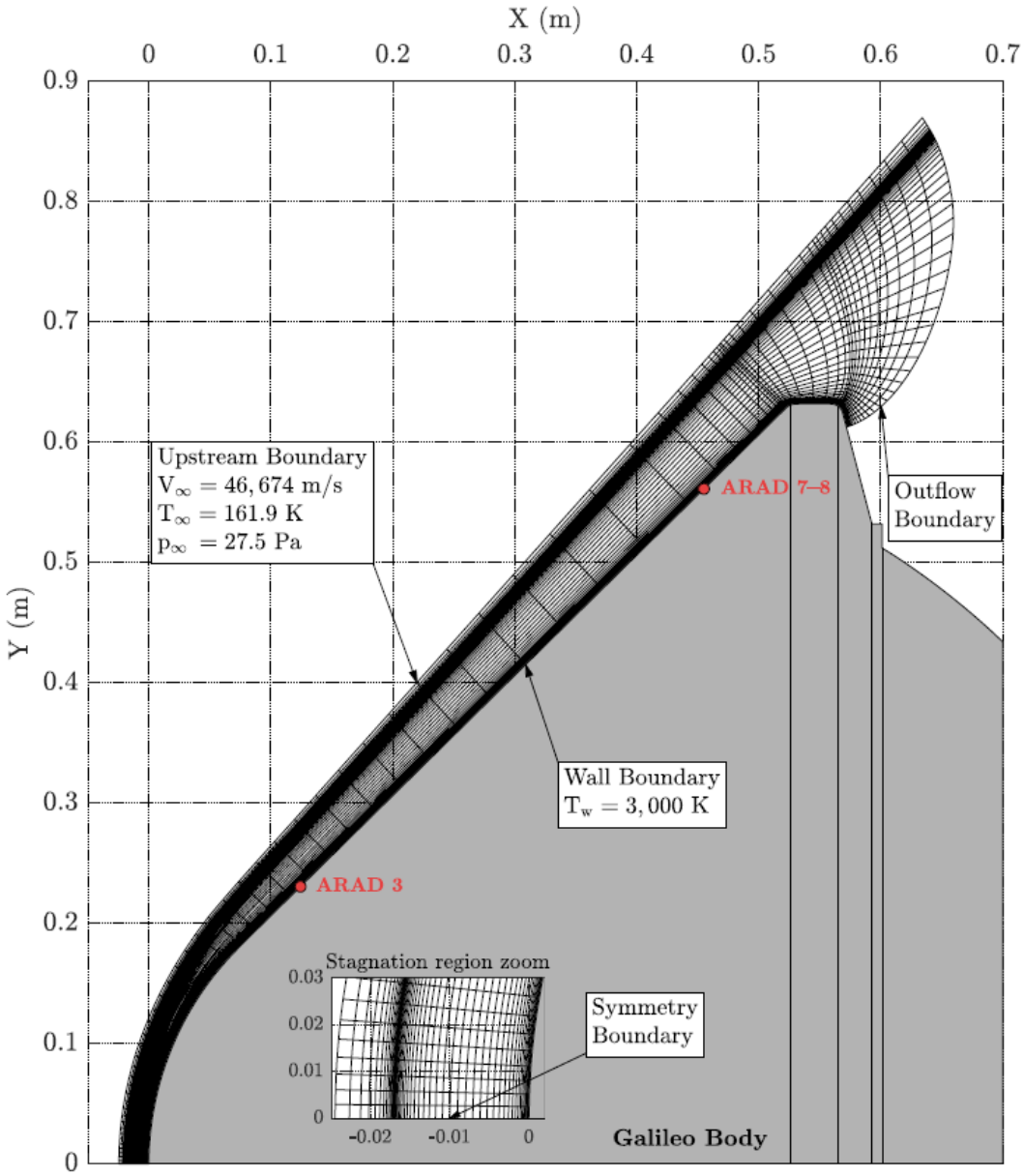

Figure 4.2: Computational domain and boundary conditions [40]

The initial wall profile of the capsule was created using **Rhinoceros 3D**, a commercial software widely used for industrial design and CAD modelling. Rhinoceros (commonly referred to as Rhino) allows for precise surface and solid modelling based on NURBS (Non-Uniform Rational B-Splines), making it ideal for generating accurate, smooth representations of aerodynamic bodies.

In this step, the geometry of the computational domain was built with high attention to continuity and smoothness, ensuring compatibility with subsequent mesh generation.

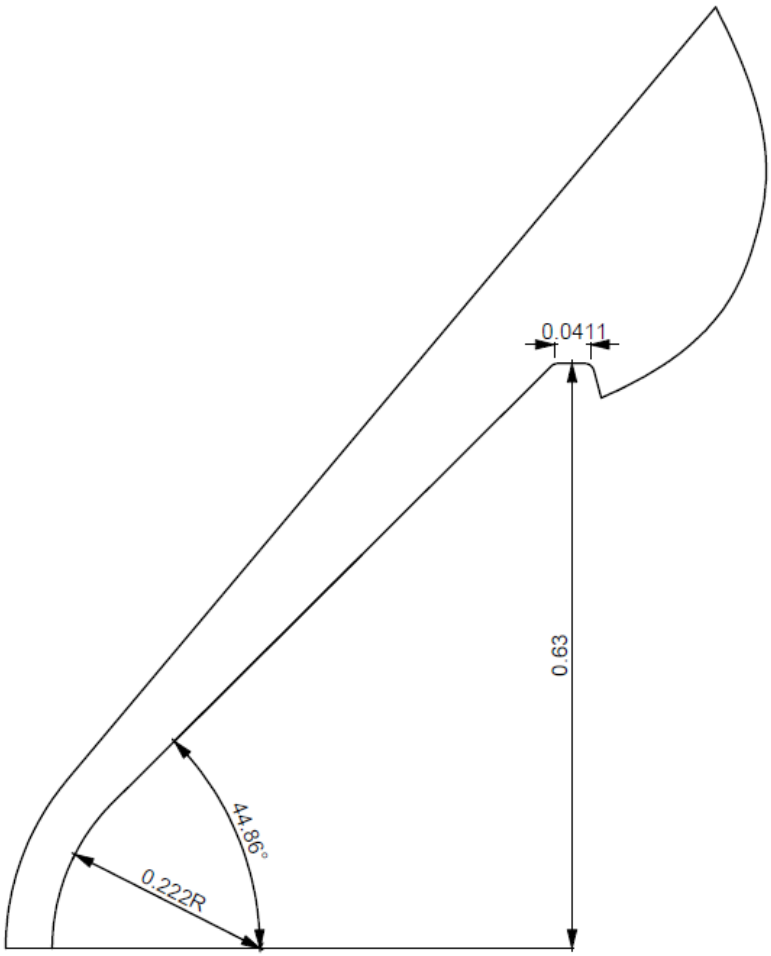

Figure 4.3: Computational domain created with Rhino [m]

4.1.2 Importing the Geometry into GridPro

Once the geometry was completed, it was exported from Rhino in a format compatible with GridPro (IGES or STEP) and subsequently imported into the GridPro preprocessing environment. At this stage, the imported CAD model was visualized as a surface shell, ready for topological operations and grid setup.

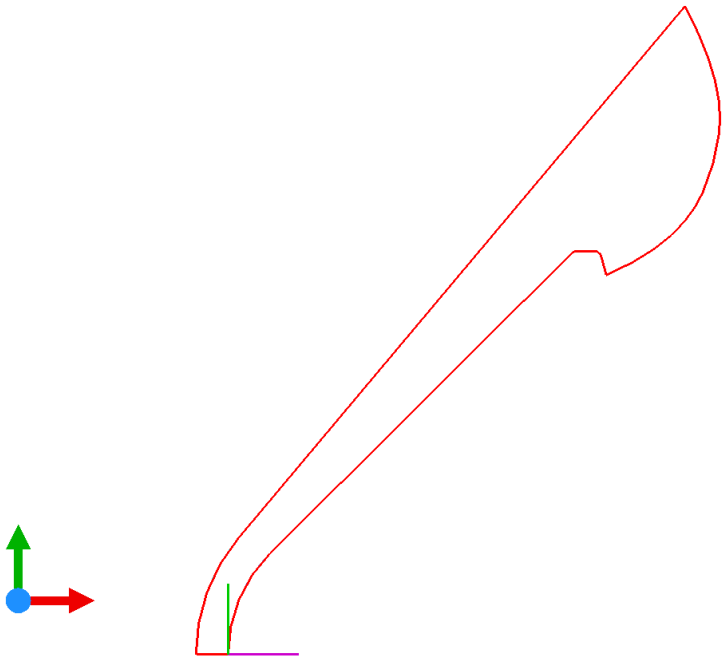

Figure 4.4: GridPro geometry import

4.1.3 Surface Meshing and Wall Classification

To allow GridPro to recognize the boundaries and apply proper block topology, a **surface meshing** operation was performed. This step converted the geometry into "surface" type entities, enabling the assignment of topological features such as corners, edges, and blocks.

4.1.4 Splitting the Surfaces

The global capsule surface was then partitioned into separate patches using the **Split Surface** function. This operation was crucial to isolate the different boundary types (e.g., inflow, symmetry plane, solid wall, and outflow) and to assign them unique identifiers and colors within the GridPro environment. This classification facilitates the subsequent assignment of boundary conditions in the CFD solver.

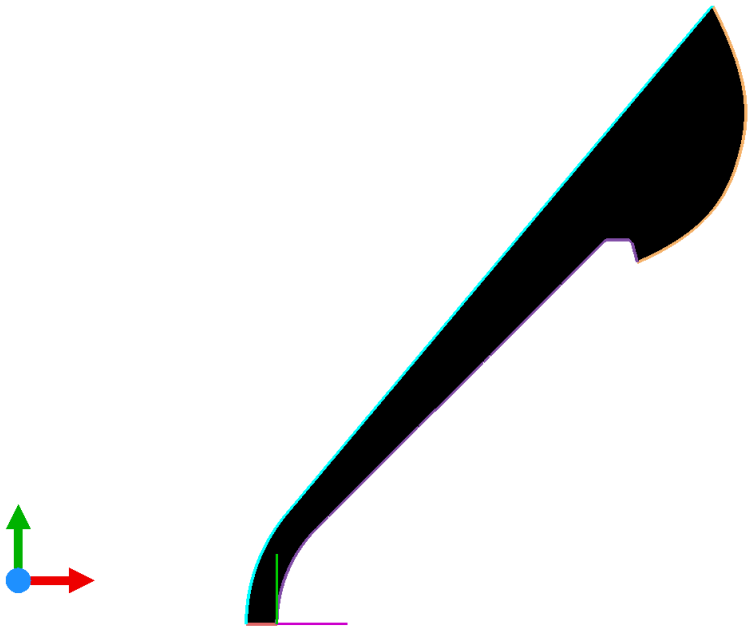

Figure 4.5: GridPro surface splitting

4.1.5 Corner Definition and Geometry Validation

Once the surfaces were correctly defined, **corners** were created and assigned to the intersecting edges between different surface patches. The corner assignment ensures a consistent block topology and grid connectivity. After all necessary corners were created and assigned, the geometry was validated within GridPro to confirm its topological consistency.

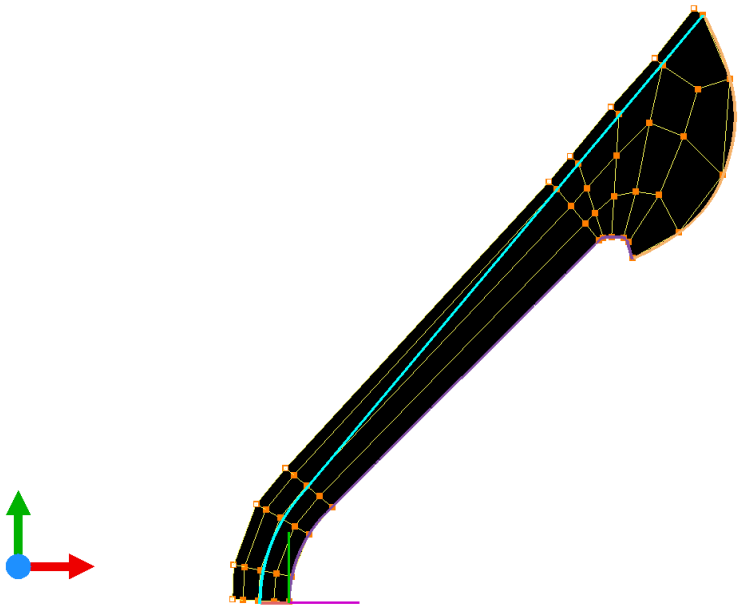

Figure 4.6: GridPro valid topology

4.1.6 Block Subdivision

After the basic block structure was established and the geometry validated, the number of computational blocks was increased through manual subdivision. This step improved mesh quality and enabled more refined control over grid clustering in critical regions, such as the stagnation point and boundary layers.

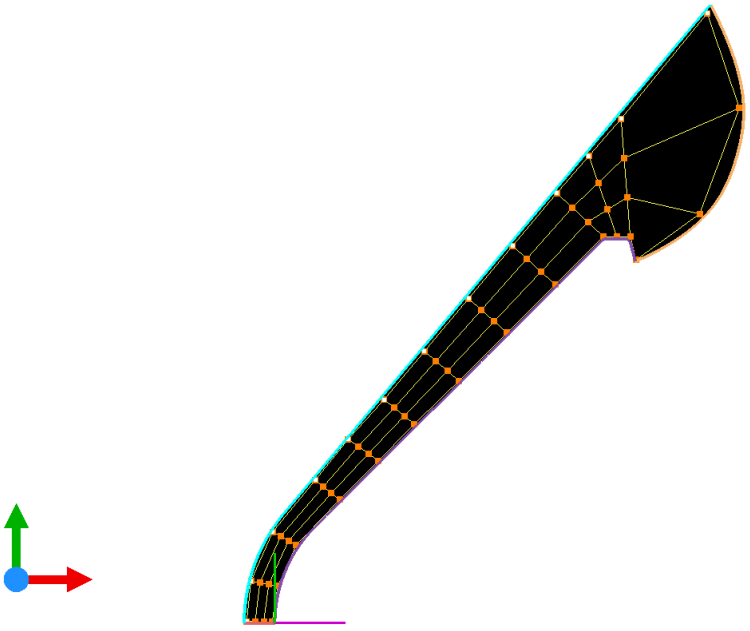

Figure 4.7: GridPro Topology 1° Upgrade

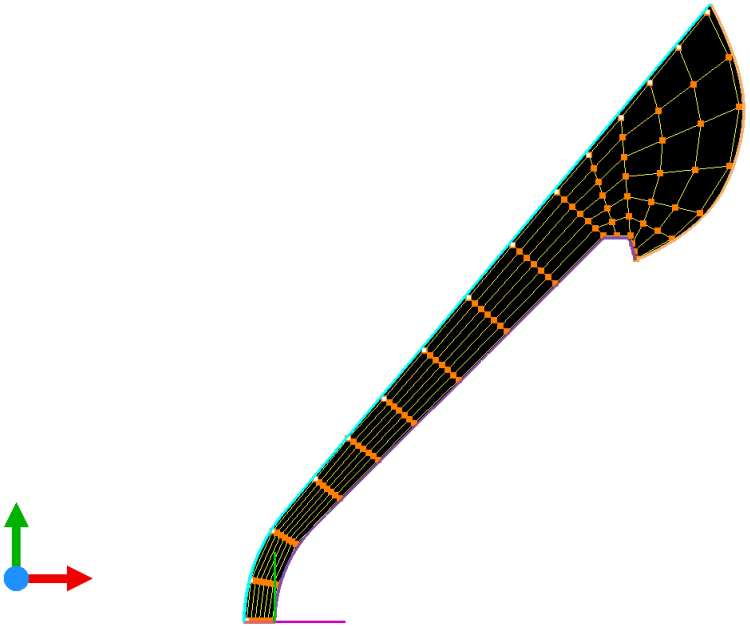

Figure 4.8: GridPro Topology 2° Upgrade

4.2 Mesh Generation with GridPro

4.2.1 Grid Density Assignment and Mesh Generation

Once the block topology was finalized and validated, the next step involved the definition of the grid resolution, i.e., the number of grid points to be distributed along each block edge. In GridPro, this process is handled by assigning a **grid density** (number of points) independently for each direction of every block face.

Given the 2D axisymmetric nature of the problem, the mesh was constructed in the *radial–axial* plane and later revolved during CFD simulation to represent the full 3D physical domain. The structured grid was therefore defined in two directions:

- **Tangential direction**: along the wall, it defines the number of cells the body is discretized

- **Normal direction**: a finer grid resolution was imposed near the wall to capture the steep gradients within the boundary layer and near the shock layer, especially where radiative heat transfer effects are significant.

The grid spacing was manually tuned for each block edge by specifying the desired number of points and the clustering law (e.g., geometric progression), allowing for enhanced resolution near walls and shock-sensitive regions.

4.2.2 Mesh Solution and Convergence

After all grid densities were assigned and clustering parameters set, the mesh generation was initiated by launching the **mesh solver** integrated within GridPro. This solver computes the position of internal grid points using elliptic PDE-based smoothing algorithms to ensure smoothness, orthogonality, and gradual variation in cell size.

During this stage, the solver iteratively adjusts the mesh until convergence is reached. Convergence is typically evaluated in terms of residual reduction or changes in cell quality metrics, ensuring that the final mesh does not contain inverted or highly skewed cells.

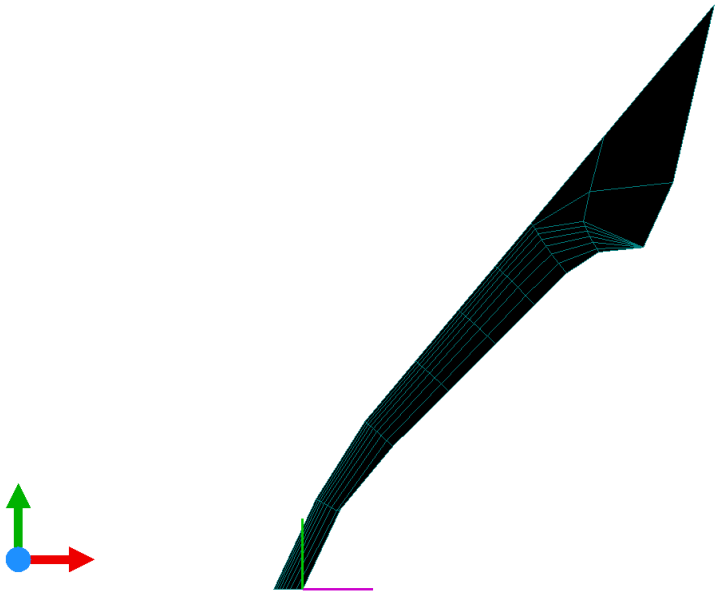

Figure 4.9: Initial pattern

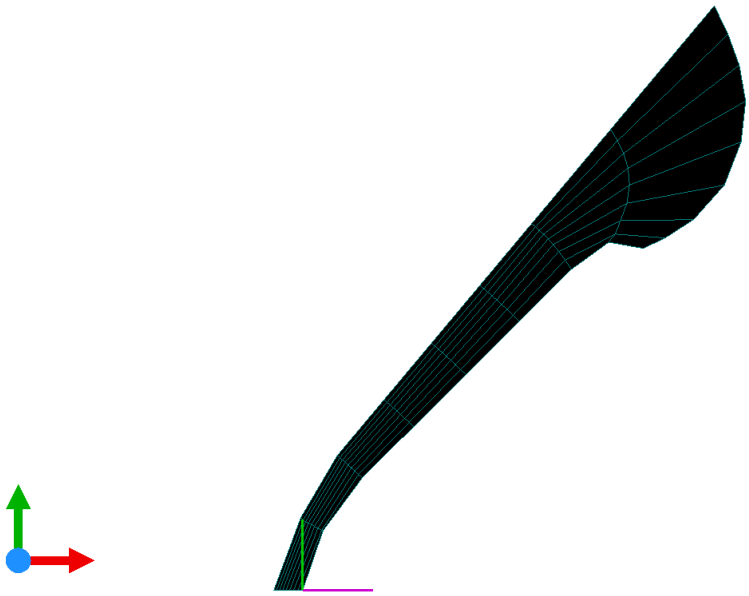

Figure 4.10: Mesh refinement

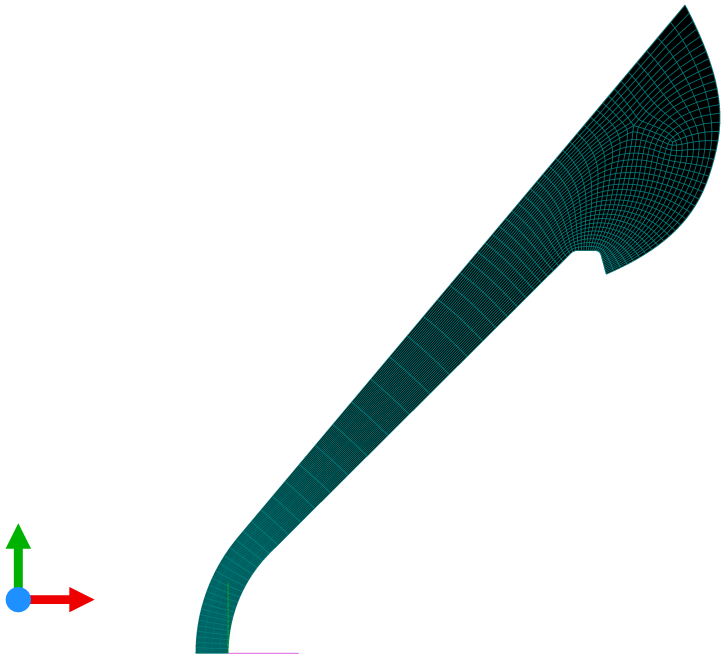

Figure 4.11: Mesh convergence 64×96 cells

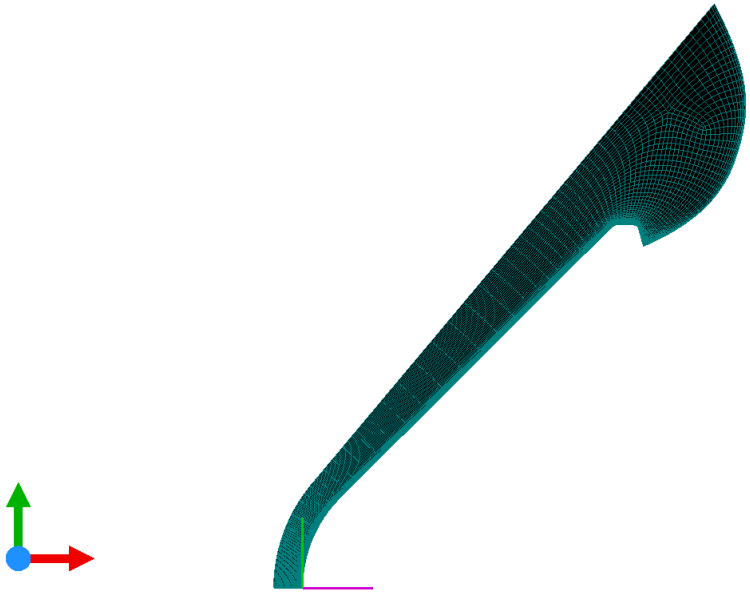

Figure 4.12: Mesh clustering

4.2.3 Near-Wall Clustering and Boundary Layer Resolution

A critical aspect of mesh generation for hypersonic flows is the accurate resolution of the boundary layer near solid walls, where strong gradients in velocity, temperature, and species concentration occur. To this end, a **near-wall grid clustering** strategy was applied exclusively along the surfaces defined as `WALL` in GridPro.

In particular, clustering was implemented along the wall-normal direction by prescribing a progressively growing cell spacing starting from the surface. The initial spacing was set using a geometric progression law, with a **growing factor** of approximately 10^{-4}. This value controls the ratio between the first and the second cell height and ensures that the mesh points remain concentrated near the wall, gradually expanding away from it.

Such a configuration guarantees sufficient resolution of the viscous sublayer and pre-shock boundary layer region, which are essential for capturing thermal non-equilibrium and radiative effects. The resulting mesh configuration led to a maximum non-dimensional wall distance (y^+) of approximately 1.5, which is within the typical acceptable range for high-fidelity Navier–Stokes solvers operating in hypersonic regimes. This level of wall resolution allows for accurate modelling of the thermal and momentum transfer phenomena without requiring wall-function approximations.

No clustering was applied in other regions of the domain (e.g., inflow, symmetry, or outflow boundaries), where the flow gradients are less severe. This selective clustering strategy ensures computational efficiency while preserving the resolution where it matters most — in the vicinity of the capsule surface, particularly in the stagnation region where heat fluxes are most intense.

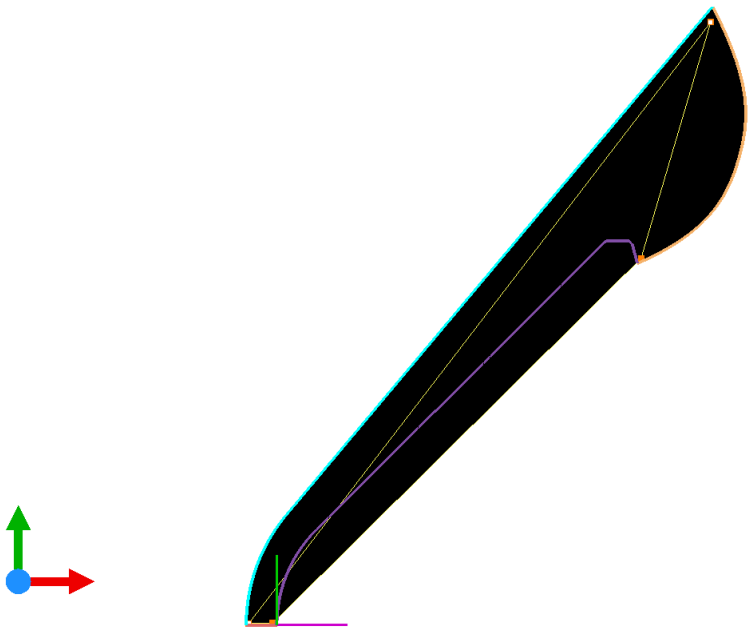

Figure 4.13: GridPro Mono-block Topology

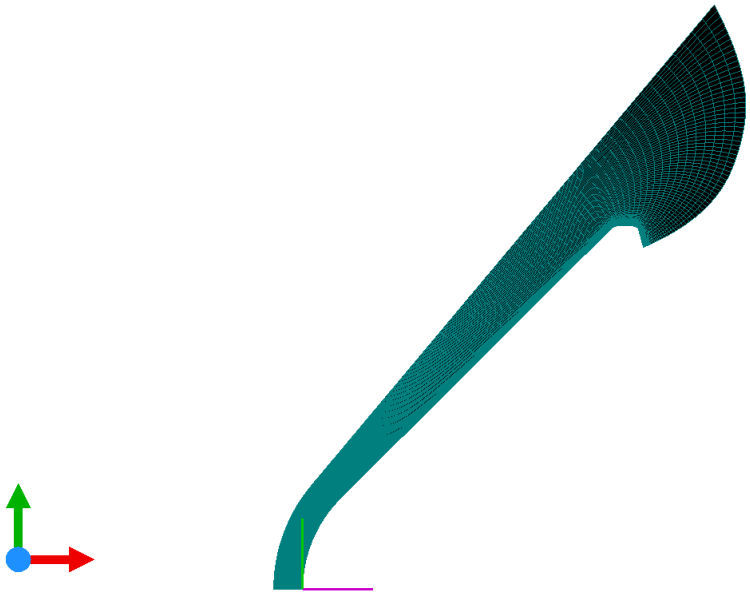

Figure 4.14: Initial Mesh

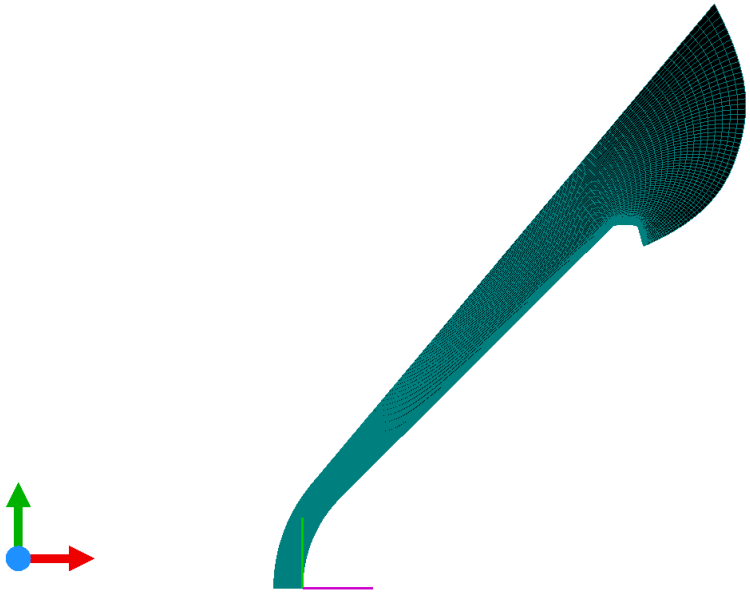

Figure 4.15: Initial Mesh

4.2.4 Final Checks and Export

Upon convergence, the mesh quality was visually inspected to confirm the absence of irregularities, abrupt transitions, or poorly shaped cells. In particular, attention was given to:

- Cell clustering near the stagnation region and wall boundaries
- Smooth transition across adjacent blocks
- Correct cell orientation and orthogonality

Once verified, the mesh was exported in the CFD++ format.

Chapter 5

SPARK Line-by-Line Code

5.1 Overview

The **SPARK Line-by-Line** code is designed to simulate the radiative properties of high-temperature, low-pressure gases and plasmas, with particular emphasis on those encountered during atmospheric entry and in high-temperature plasma radiation sources.

Developed using both MATLAB and FORTRAN, the code is freely distributed under the terms of the GNU General Public License (GPL), encouraging open use and collaborative development.

The associated spectral database includes over 270 radiative processes, comprising bound-bound, bound-free, and free-free transitions. This comprehensive database enables accurate simulation of radiation from high-temperature gases and plasmas relevant to various planetary atmospheres, including Earth (Air), Mars-like (CO_2–N_2), Titan (N_2–CH_4), and gas giant environments (H_2–He). The modelled spectra typically include between 10^4 and 10^6 spectral lines, along with the superposition of multiple continua.

Additionally, the database supports partially implemented models for other gas mixtures, thus broadening the applicability of the code to general plasma science problems. A specialized version of the database is also available for atomic species ranging from hydrogen ($n = 1$) to krypton ($n = 32$), including both singly and doubly ionized states. This feature is particularly beneficial for diagnostics such as Laser-Induced Breakdown Spectroscopy (LIBS).

5.2 Capabilities and Structure of the SPARK Line-by-Line Code

The SPARK Line-by-Line code has been developed to simulate the spectral radiation emitted by low-pressure plasmas, with a primary focus on aerospace applications such as planetary atmospheric entry phenomena. While its original intent lies in modeling radiative emissions under entry conditions, the code is inherently versatile and applicable to a broad range of scenarios. These include, but are not limited to, spectral analysis in low-pressure plasma facilities, modeling of atmospheric absorption features, radiation from combustion environments, and other general-purpose plasma diagnostics. The numerical

core of the code supports detailed modeling of bound-bound atomic and molecular transitions, incorporating fine-structure splitting (singlet, doublet, triplet) and Λ-doubling effects. In addition to discrete spectral lines, the code also accounts for continuum radiation processes. Bound-free mechanisms, such as photoionization, photodetachment, and photodissociation, are handled through cross-sectional data extracted from literature sources. These can be either temperature-averaged or state-specific, allowing a flexible treatment of various physical models. Free-free emissions, notably Bremsstrahlung, are included using widely accepted theoretical and semi-empirical models. Spectral line broadening is modeled using a Voigt profile, which effectively captures Doppler broadening—dominant in low-pressure plasmas—as well as Lorentzian contributions from collisional and Stark effects, relevant at elevated pressures or electron densities. The line shape computation employs a specially optimized algorithm introduced in 2007, enabling fast and precise evaluation of spectra comprising up to one million transitions. Users may fine-tune the spectral resolution, balancing computational speed against line profile fidelity according to the needs of the specific simulation. This computational efficiency is crucial for modeling radiation from species such as CO_2 in the infrared region, where high-resolution line-by-line treatment is essential. The code has been designed with modularity and flexibility as guiding principles. Spectroscopic data are maintained in external ASCII files, entirely decoupled from the numerical solvers, which facilitates database customization and extension. A graphical interface is available for simplified interaction, but all core functionalities are governed through standard input and output files. This file-based architecture ensures seamless integration with external solvers, such as hydrodynamic or radiative transfer codes, provided they conform to the same data exchange format.

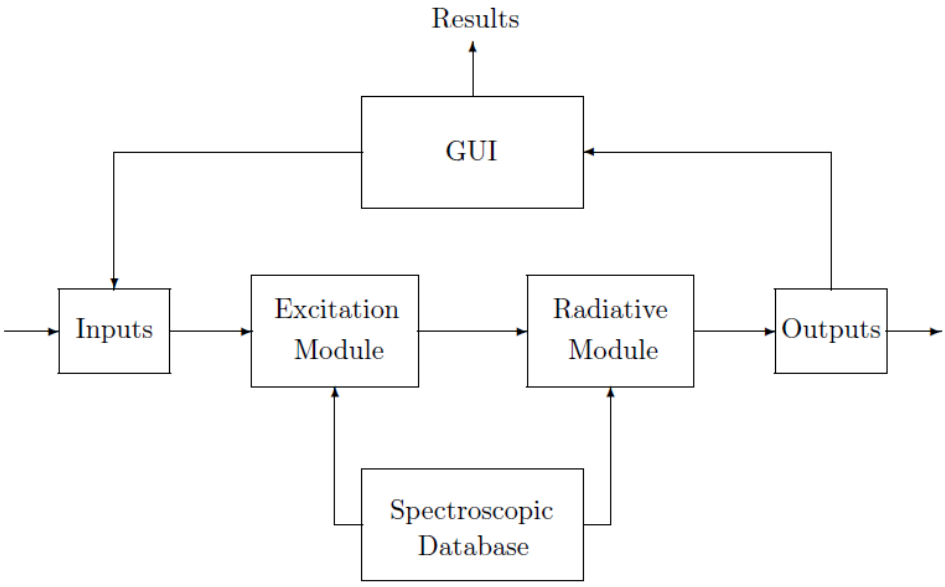

Figure 5.1: Structure of the SPARK Line-by-Line Code

Internally, the SPARK framework is divided into two functional modules as shown in Fig5.1. The first is the excitation module, which computes internal level populations of atomic and molecular species. It supports multi-temperature Boltzmann distributions, typically involving separate translational (T_r), vibrational (T_v), and excitation (T_exc) temperatures. Alternatively, it allows users to provide custom non-equilibrium population distributions. The second is the radiation module, which utilizes the level populations to evaluate absorption and emission coefficients. This modular separation allows targeted adjustments and facilitates coupling with external physical models.

5.3 Radiative–Transfer Modules in SPARK LbL

Radiative heating at the surface of entry probes is evaluated with the RADTRANS package, located in the `RADTRANS` directory of SPARK. Two alternative solvers are supplied:

1. *Tangent–slab* model
2. *Ray–tracing* algorithm.

Both operate on structured, axisymmetric ($r-z$) meshes and are parallelised for shared-memory and distributed-memory architectures, allowing them to process the extremely fine spectral meshes (up to several million wavelength points) generated by the line-by-line database without compromising turnaround time. Because every wavelength is treated explicitly, the flux computation remains fully consistent with the line-by-line philosophy.

5.3.1 Hybrid MATLAB–Fortran Workflow

Line-by-line emission and absorption coefficients are generated in MATLAB; Fortran routines then

- construct the tangent slabs or ray bundles,
- intersect them with the CFD grid
- integrate the radiative-transfer equation along each line of sight.

5.3.2 Tangent Slab Model

First introduced several decades ago, the tangent–slab method offers the least computational burden among the available radiative–transfer schemes and delivers acceptable accuracy in the immediate vicinity of the stagnation point. Its economy, however, is offset by a rapid loss of fidelity as the evaluation point migrates toward the shoulder or fore-body.

The core hypothesis assumes that, along a ray drawn normal to the surface, thermodynamic quantities remain uniform; put differently, gradients in the tangential direction are neglected. This simplification removes any azimuthal dependence in the radiation field, permitting an analytic evaluation of the solid-angle integral.

Figure 5.2 illustrates the geometry: the translucent contour depicts the true temperature distribution, whereas the opaque shading shows the constant-property slab that extends to infinity along the viewing line (one hemisphere only). The red marker designates the surface point of interest—in this example, the stagnation point.

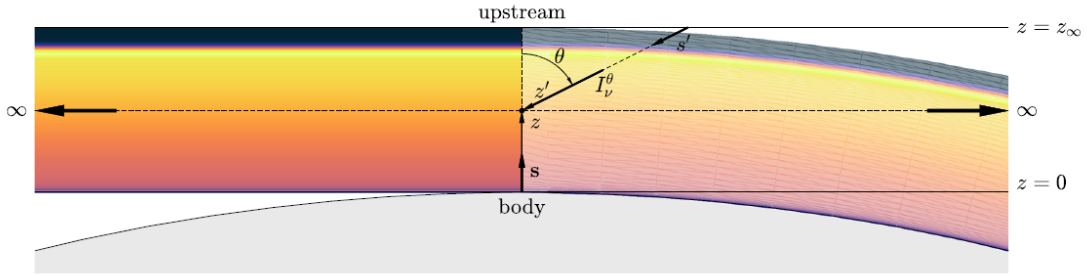

Figure 5.2: Tangent-slab model representation, Ref. [40]

Because the tangent–slab algorithm samples only the column of cells that lies normal to the wall element, it interrogates a handful of neighbours and therefore incurs a negligible computational overhead. The hypothesis of tangential uniformity is most credible at the stagnation point—where wall-parallel gradients are weakest—hence the method performs best there and degrades toward the shoulder.

Under this assumption the directional integral in Eq.(2.57) collapses to an analytic form, which greatly simplifies the evaluation of the heat flux. The resulting expression reads

$$q_{\mathrm{rad}}^{\mathrm{TS}} \;=\; 2\pi \int_0^{\infty} \int_0^{z_\infty} j_\nu \, \mathscr{E}_2[\tau_\nu(z)] \, \mathrm{d}z \, \mathrm{d}\nu, \tag{5.1}$$

where $\mathscr{E}_2$ is the exponential integral of order 2. A convenient approximation, due to Johnston [21], is

$$\mathscr{E}_2(x) \approx 0.2653 e^{-8.659x} + 0.7347 e^{-1.624x} \tag{5.2}$$

5.3.3 Ray-Tracing Model

Integrated into SPARK LbL, the **RADTRANS** solver determines surface heat loads—on thermal-protection tiles, flight-test sensors or facility diagnostics—via a line-by-line, ray–tracing formulation. Key features include:

- *Fully spectral*: fluxes are obtained directly from the same multi-million-point wavelength grid used in the emission/absorption calculations.
- *Parallel execution*: OpenMP/MPI kernels distribute rays across multiple processors, sustaining practical run-times even on very fine spectral meshes.
- *Proven heritage*: the algorithm has reproduced radiative fluxes for several benchmark entries, notably
  - Mars landers *Phoenix* (NASA, 2008) and *Schiaparelli* (ESA, 2016),

– the *Galileo* probe's plunge into Jupiter (1995)

– forthcoming M-class missions targeting Uranus and Neptune.

RADTRANS therefore extends the line-by-line philosophy from local emission coefficients to global radiative-transfer predictions, furnishing high-fidelity heat-flux estimates across a range of planetary-entry environments.

Ray Generation

The current ray-tracer employs a *Fibonacci lattice* [17] to distribute rays quasi-uniformly over the unit sphere—eliminating the polar clustering that plagued the earlier latitude–longitude scheme (Fig.5.3, (b)). This change markedly improves angular sampling without increasing ray count.

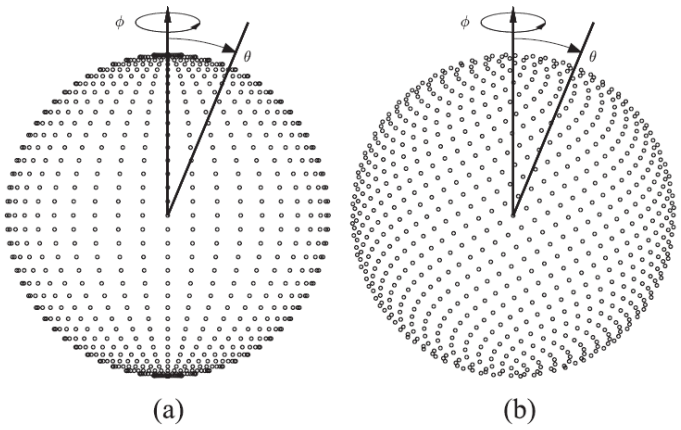

Figure 5.3: (a) Latitude-longitude scheme (b) Fibonacci-lattice scheme

The method proceeds in two nested integrations:

1. spatial integration of Eq. (2.57) along a single ray that links an interior point to the boundary, and

2. angular integration over all ray directions emanating from that point.

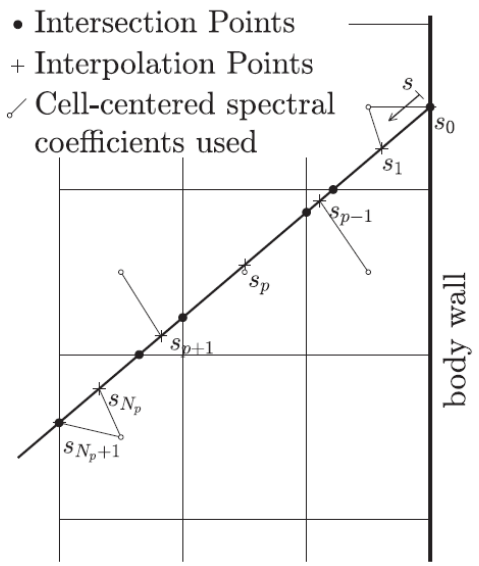

Figure 5.4: Representation of Linear Interpolation in the Ray Tracing at a given cell, Ref. [40]

For every ray, the algorithm tracks its path through the mesh, solving Eq. (**??**) segment by segment while accounting for the distance traversed inside each cell.

Discretisation options. Because a generic ray seldom intersects cell centres, one must decide how to represent material properties along the path:

- *Piecewise–constant sampling* assumes uniform coefficients within each cell, but introduces jumps at cell faces and may degrade accuracy on coarse grids.

- *Linear interpolation* averages properties between adjacent cells, smoothing discontinuities and improving the estimate of the spectral intensity along the slice (Fig. 2.6). This interpolation capability is already implemented in SPARK LbL.

A systematic assessment of the interpolation strategy—its impact and computational cost—will be presented in Section **??**.

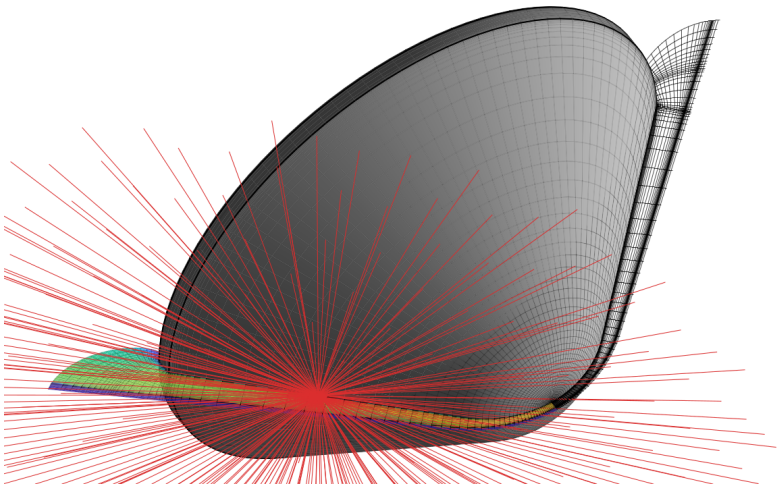

Figure 5.5: Example of a Ray-tracing calculation for a Jupiter entry at 47.5 km/s, IPFN – IST, Ray tracing (s.d.), latest access 17th july 2025.

5.4 Matlab Part

The routine `allRadTrans.m` orchestrates every MATLAB task in the radiation workflow, invoking all subsidiary functions. The script requires several inputs. Its first operation is to assemble the two-dimensional array `RadCellsData`, which stores both geometric descriptors and local flow variables for every computational cell.

Array dimensions.

- Rows: $N \times M$, where
  - N is the number of cells normal to the wall, and
  - M is the number tangential to the wall.
- Columns: L, a variable length that depends on the number of distinct temperatures and chemical species represented in the gas mixture.

Column layout (per row).

$$\underbrace{A_x\ A_y\ \ B_x\ B_y\ \ C_x\ C_y\ \ D_x\ D_y}_{\text{cell-vertex coordinates}} \quad \underbrace{T}_{\text{mixture temperature}} \quad \underbrace{T_{k_1}\ \ldots\ T_{k_n}}_{\text{mode temperatures}} \quad \underbrace{N_1\ \ldots\ N_s}_{\text{species number densities}}$$

Thus each row fully characterises one quadrilateral cell by listing its vertex coordinates (A, B, C, D), the bulk temperature T, a set of mode-specific temperatures $\{T_{k_i}\}$, and the number densities $\{N_j\}$ for every species.

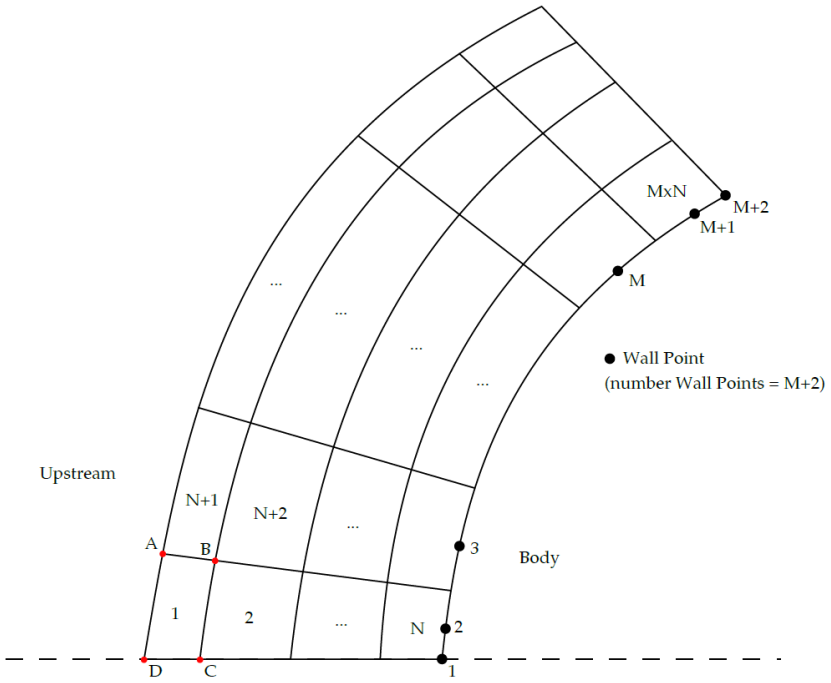

Figure 5.6: Mesh structure in radiative transfer module

Array layout and mesh orientation. The leading eight columns, A_x through D_y, store the coordinates of the four vertices of each quadrilateral cell, starting at the upper–left corner and listed clockwise. RADTRANS presumes a west-to-east freestream with the wall situated on the eastern boundary of the grid.

Rows in `RadCellsData` must be ordered as follows (Fig. B.3): begin at the upstream symmetry point—i.e. the south-west corner—march through the N cells closest to the stagnation line until the wall is encountered, then repeat this sweep for each of the M tangential layers.

Column T records the translational temperature, while the subsequent entries $T_{k_1}, \ldots, T_{k_n}$ contain additional mode temperatures ($T_{\text{rot}}, T_{\text{vib}}, T_{\text{e}}$, etc.) when a multi-temperature nonequilibrium model is in use. The remaining fields $N_1, \ldots, N_s$ hold species number densities.

If the CFD solution was generated outside SPARK, the user must assemble `RadCellsData` manually according to these rules and disable the three lines of code labelled `Building RadCellsData` inside `allRadTrans.m`. The finished array should be saved as a `.mat` file in

`../RADTRANS/0_flowfieldparams/`.

Table 5.1: Kinetic model employed in the present work and forward Arrhenius coefficients.

		Arrhenius rate coefficients			
Reaction	**Process**	$C_r\,[\mathrm{m^3\,mol^{-1}\,s^{-1}}]$	α_r	$E_f/k_B\,[\mathrm{K}]$	**Ref.**
R1	$H_2 + H \leftrightarrow H + H + H$	8.347×10^{13}	-1.0	5.234×10^4	10
R2	$H_2 + He \leftrightarrow H + H + He$	4.173×10^{12}	-1.0	5.234×10^4	10
R3	$H_2 + H_2 \leftrightarrow H + H + H_2$	1.043×10^{13}	-1.0	5.234×10^4	10
R4	$H_2 + H^+ \leftrightarrow H + H + H^+$	8.347×10^{13}	-1.0	5.234×10^4	10
R5	$H_2 + e^- \leftrightarrow H + H + e^-$	8.347×10^{13}	-1.0	5.234×10^4	10
R6	$H + e^- \leftrightarrow H^+ + e^- + e^-$	2.279×10^5	0.5	1.578×10^5	10
R7	$H + H \leftrightarrow H^+ + e^- + H$	6.172×10^2	0.5	1.160×10^5	10
R8	$H + He \leftrightarrow H^+ + e^- + He$	4.883×10^2	0.5	1.160×10^5	10
R9	$He + e^- \leftrightarrow He^+ + e^- + e^-$	1.332×10^5	0.5	2.852×10^5	10
R10	$H_2^+ + e^- \leftrightarrow H + H$	7.076×10^8	-0.4	0.000×10^0	21

Chapter 6

CFD Analysis and Results

This chapter presents the numerical results obtained with `CFD++` for the flow around the *Galileo* entry probe at $M_\infty \simeq 50$. Two distinct thermo-chemical models were considered:

1. *Thermal Equilibrium* (TE): a single temperature (T) governs translational, rotational, vibrational and electronic energy modes, and chemical composition is constrained by local thermodynamic equilibrium.

2. *Thermal Nonequilibrium* (TNE): a two-temperature model ($T_{\mathrm{tr,rot}}$, $T_{\mathrm{vib,elec}}$) is coupled with finite-rate chemistry; vibrational relaxation and dissociation–recombination kinetics are treated with Park's model.

For each model the same post-processing pipeline was applied, and the discussion is organised in parallel subsections to underline the effect of the thermo-chemical treatment. All graphs are to be understood with SI international system units of measurement. Distance: $[m]$ Velocity: $[m/s]$ Pressure: $[Pa]$ Temperature: $[K]$ Number density: $[1/m^3]$ Heat Flux: $[W/m^2]$

6.1 Thermal Equilibrium Case

6.1.1 Solver Convergence

Figure 6.1 shows the residuals of momentum, energy and mass. After 6 000 iterations all residuals drop by at least four orders of magnitude, reaching normalised values below 10^{-4} when divided by the reference norms (freestream density ρ_∞ and dynamic pressure q_∞). The plateau that follows confirms that the flow solution is iteration-independent.

6.1.2 Mach-Number Field

Figure 6.2 depicts the Mach distribution. A subsonic pocket ($M < 1$, blanked by the colour cut-off) extends between the detached bow shock and the probe nose, while the undisturbed freestream maintains $M \approx 50$. Immediately downstream of the normal portion of the shock the flow is still hypersonic ($M \gtrsim 8$) and then accelerates around the shoulder.

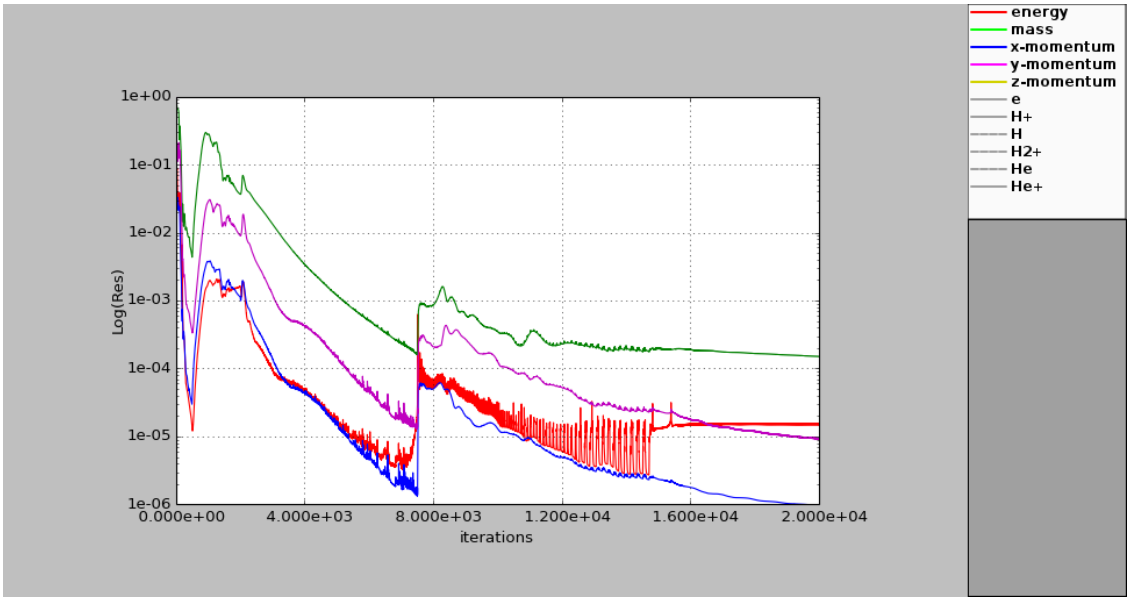

Figure 6.1: Residual history for the TE simulation.

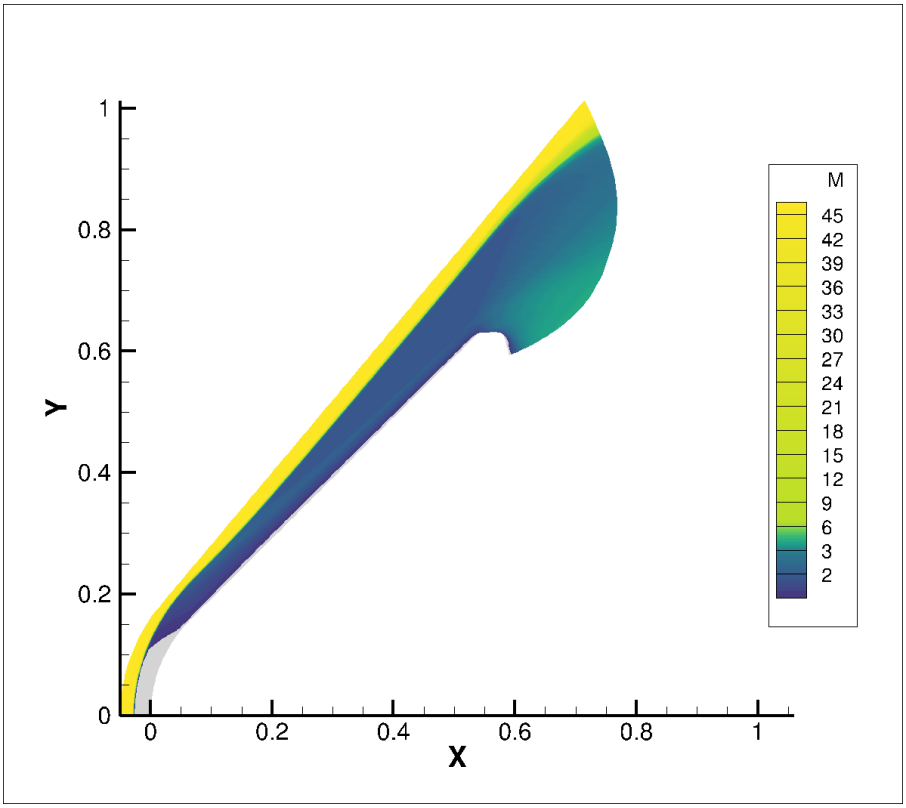

Figure 6.2: Mach number distribution (TE). White region: $M < 1$.

6.1.3 Static Pressure Field

The discrete (banded) palette in Fig. 6.3 emphasises the expansion fan that emanates from the shoulder. Immediately behind the normal shock the static pressure rises from $p_\infty = 27.5$ Pa to about $p_2 = 85$ kPa, yielding a ratio $p_2/p_\infty \approx 3.1 \times 10^3$. Further downstream the pressure decreases as the flow expands over the sphere–cone flank.

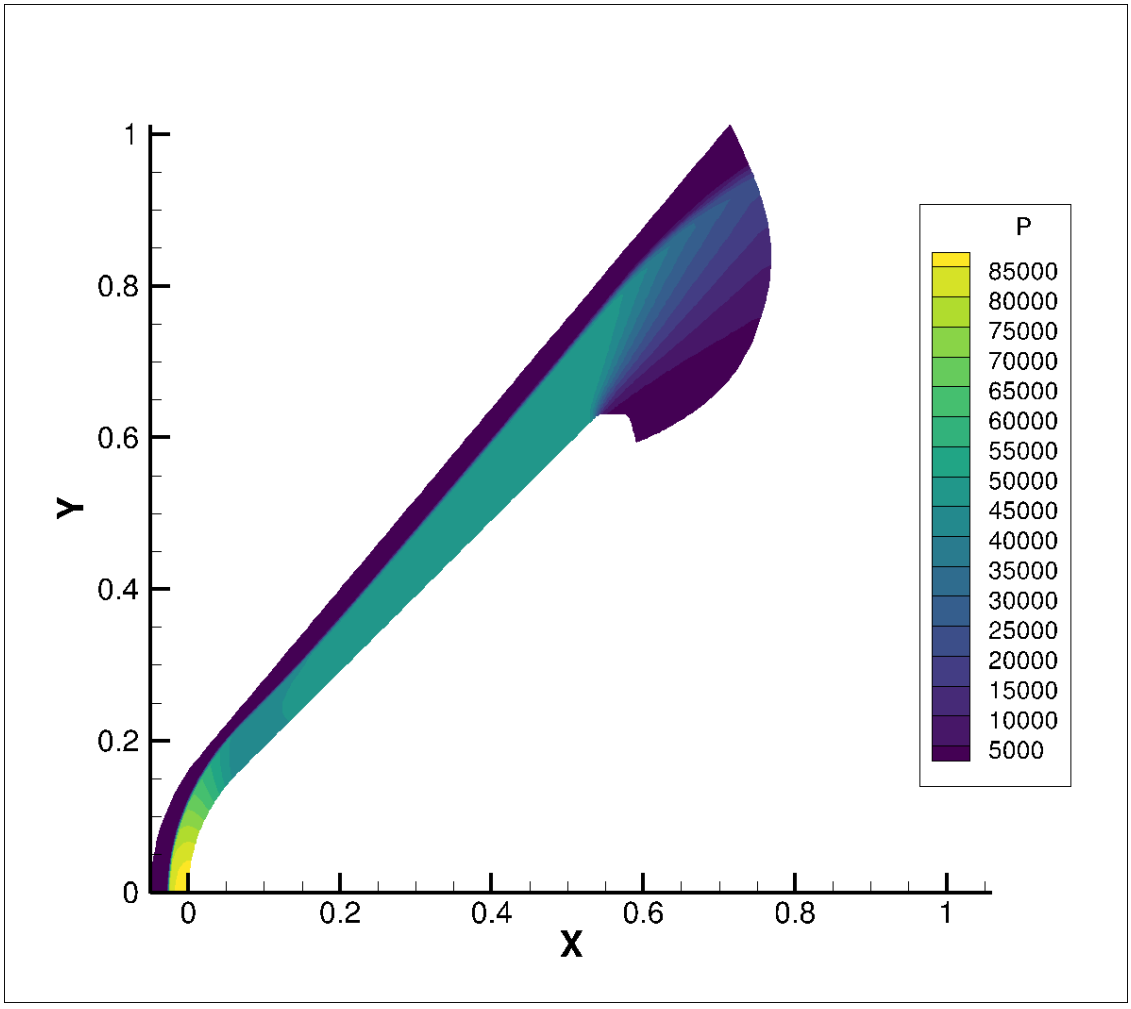

Figure 6.3: Static-pressure distribution (TE); discrete shading highlights the expansion fan on the shoulder.

6.1.4 Static Temperature Field

Figure 6.4 shows the temperature contours. The peak temperature at the stagnation streamline immediately behind the shock reaches $T_{\max} \approx 36\,000$ K.

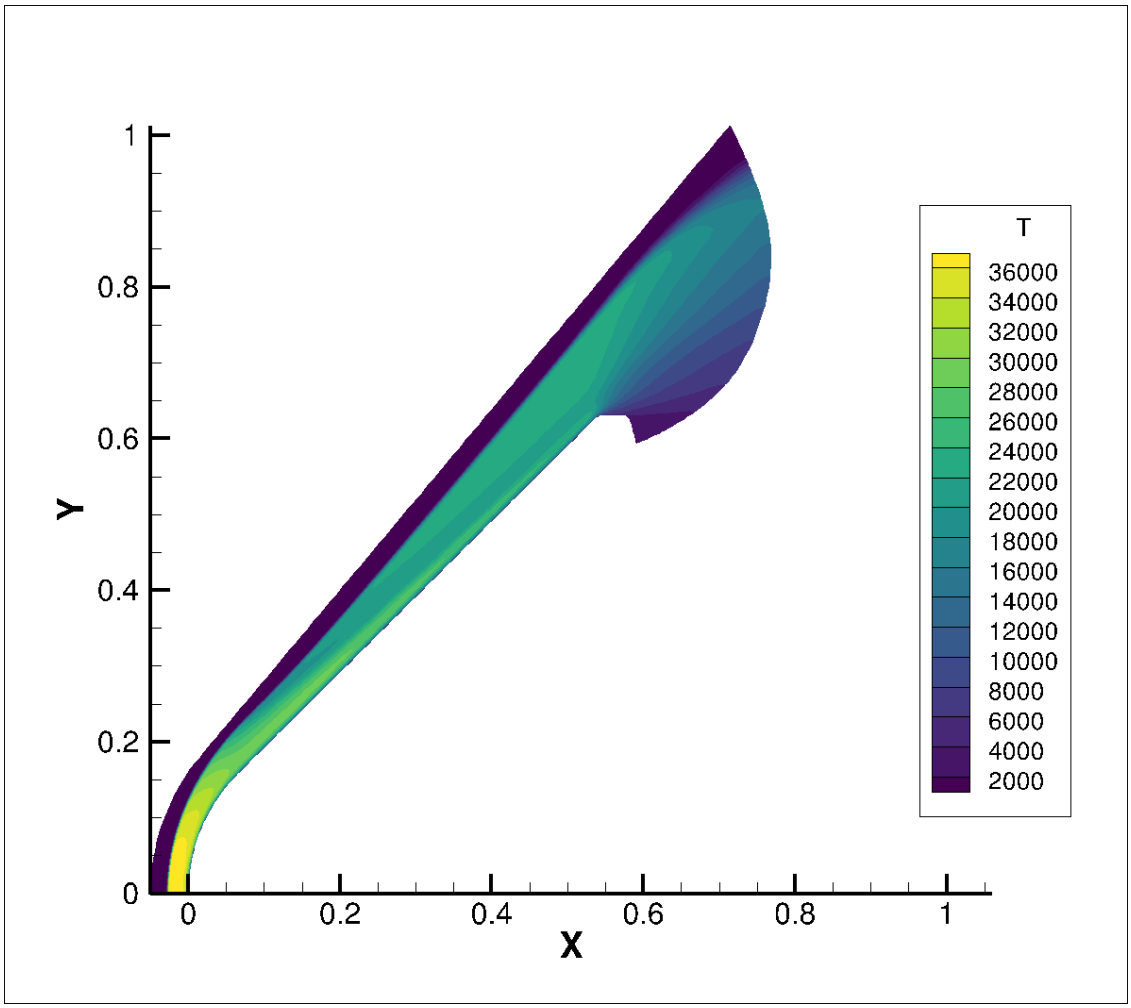

Figure 6.4: Static-temperature field (TE).

6.1.5 Stagnation-Line Profiles

The axial profiles in Fig. 6.5 track the flow from the freestream, through the shock, and down to the wall:

- **Pressure**: a sharp jump at the shock, followed by a mild rise within the subsonic bubble.

- **Velocity**: the post-shock velocity decreases monotonically, reaching zero at the nose stagnation point.

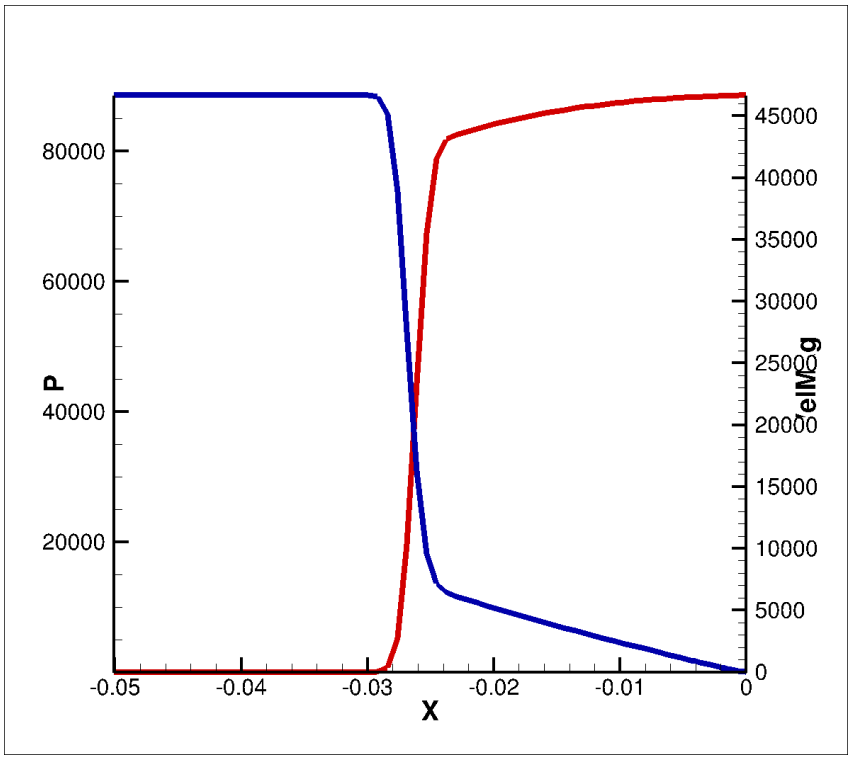

Figure 6.5: Pressure and axial velocity along the stagnation streamline (TE).

6.1.6 Species Number Densities

Figure 6.6 presents the species-number densities [m^{-3}] for the major species. Dissociation of H_2 and He ionisation are confined to the post-shock layer;

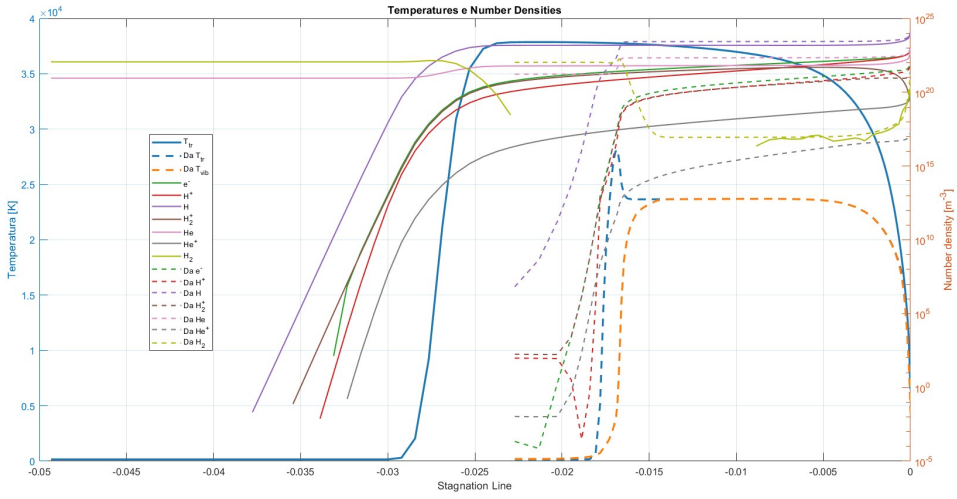

Figure 6.6: Species number densities along the stagnation line (TE).

6.1.7 Wall-Normal Convective Heat Flux

The wall-normal variation of the convective heat flux, $q_{\mathrm{conv}}(y)$, is shown in Fig. 6.7. The maximum value at the surface reaches $q_{\mathrm{conv,max}} \simeq 75\ \mathrm{MW\,m^{-2}}$, in line with previous estimates for Jupiter-class entries.

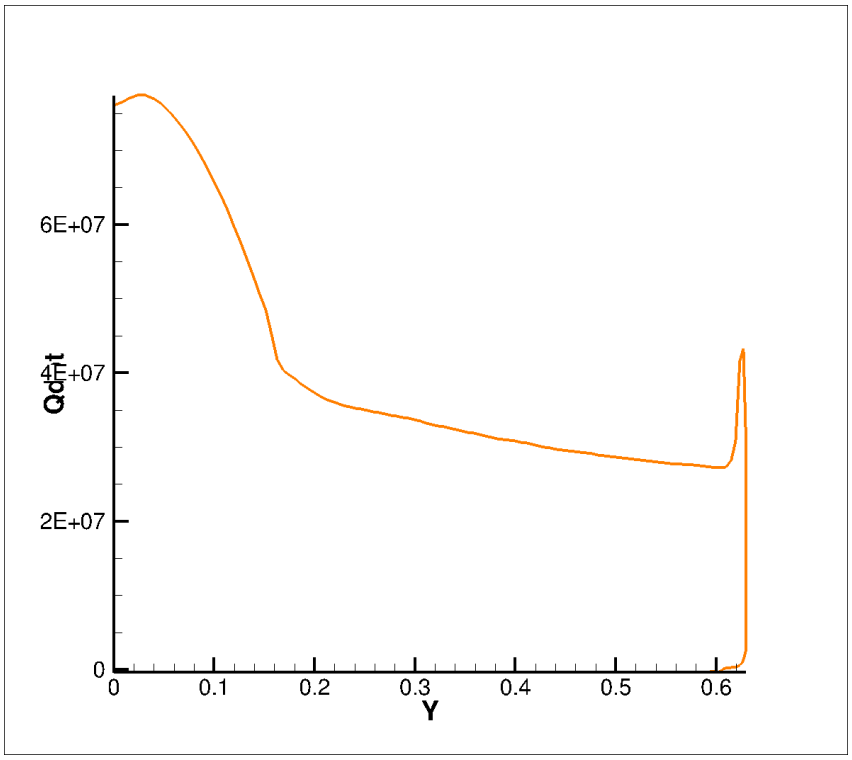

Figure 6.7: Convective heat-flux profile normal to the wall at the nose (TE).

6.2 Thermal Nonequilibrium Case

6.2.1 Mach-Number Field

(Fig. 6.10) shows the topology of the subsonic bubble is unchanged.

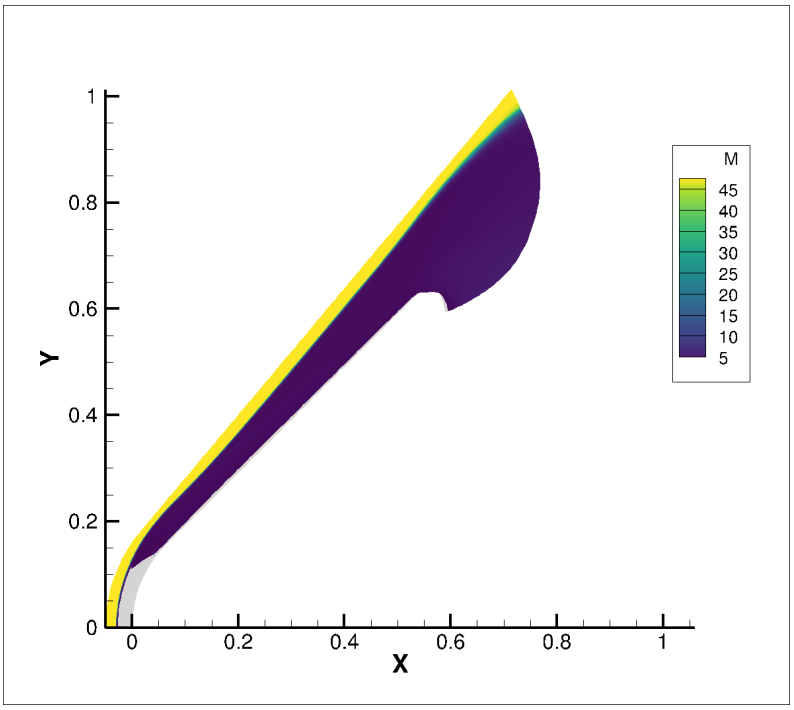

Figure 6.8: Mach number distribution (TNE). White region: $M < 1$.

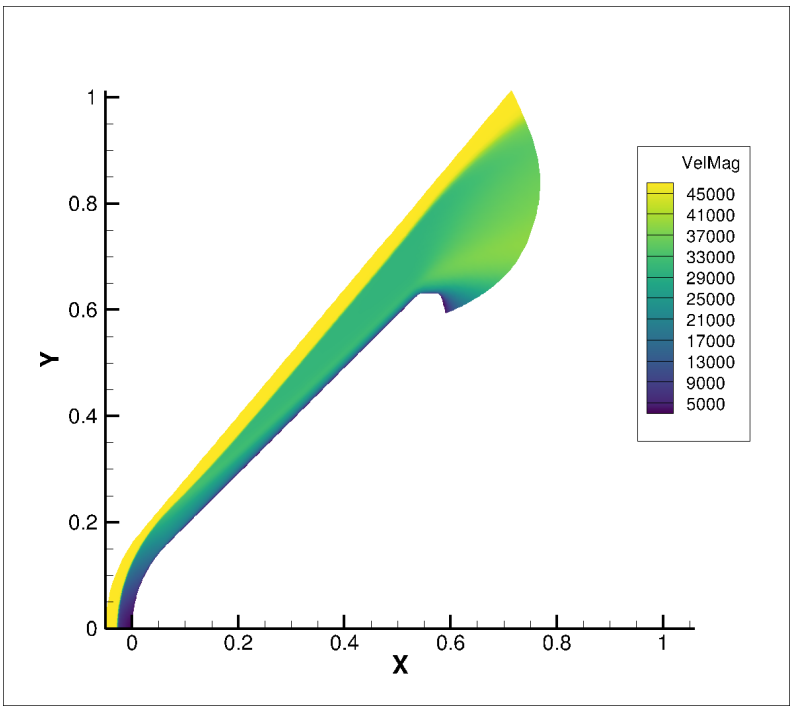

Figure 6.9: Velocity Magnitude distribution (TNE)

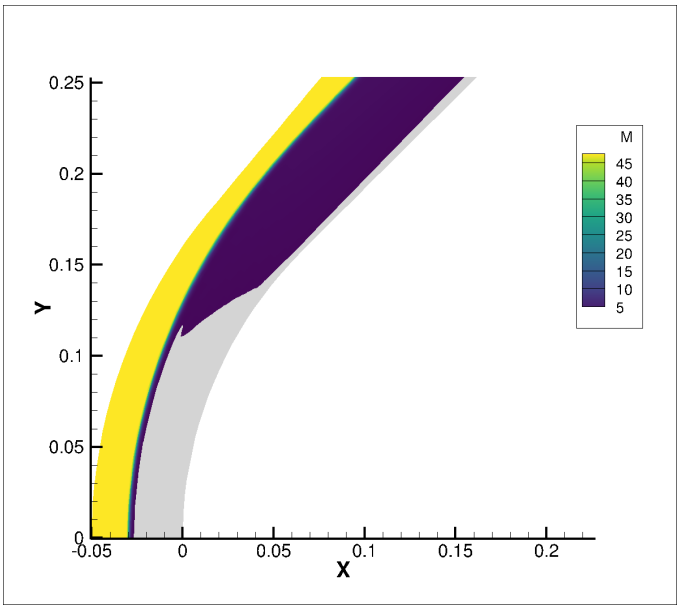

Figure 6.10: Stagnation Point zone (TNE). White region: $M < 1$

6.2.2 Static Pressure Field

The same pressure jump of Thermal Equilibrium case is observed (Fig. 6.11).

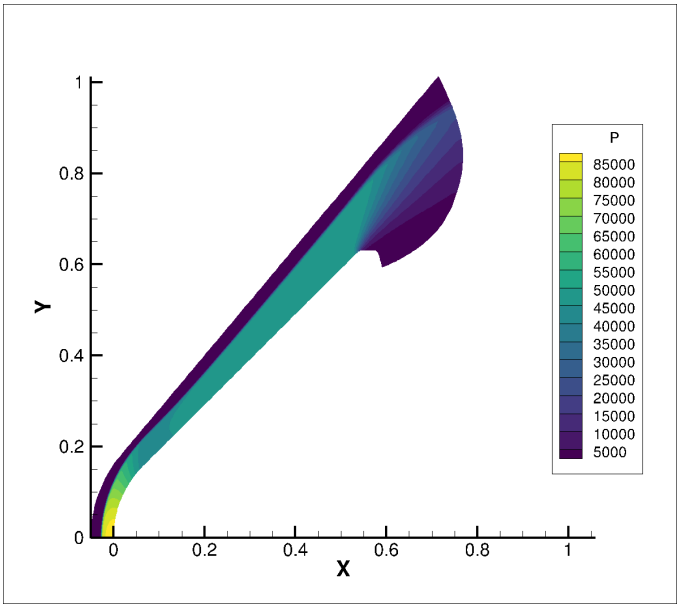

Figure 6.11: Static-pressure distribution (TNE); discrete shading highlights the expansion fan on the shoulder.

6.2.3 Temperatures Field

The translational–rotational temperature peaks at $T_{\mathrm{tr,max}} \approx 42\,000$ K just behind the shock, higher than the equilibrium value, while the vibrational temperature peaks at little more than 35 000 K upstream of the stagnation point (Fig. 6.12).

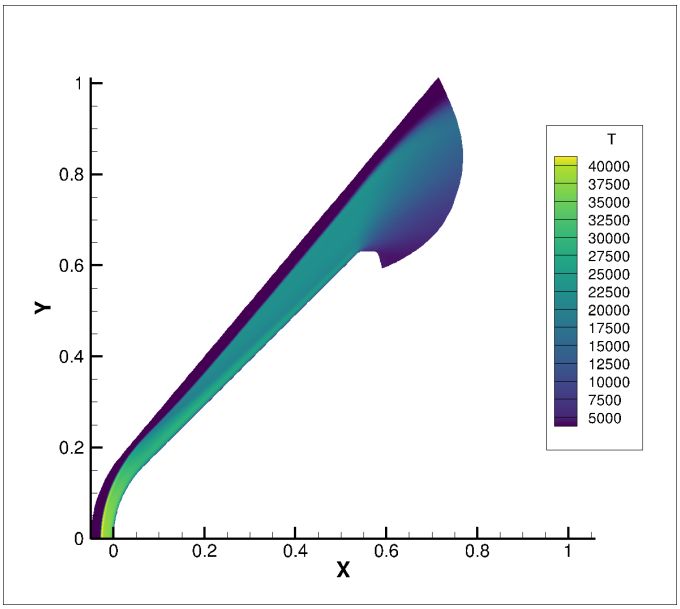

Figure 6.12: Static-translational temperature field (TNE).

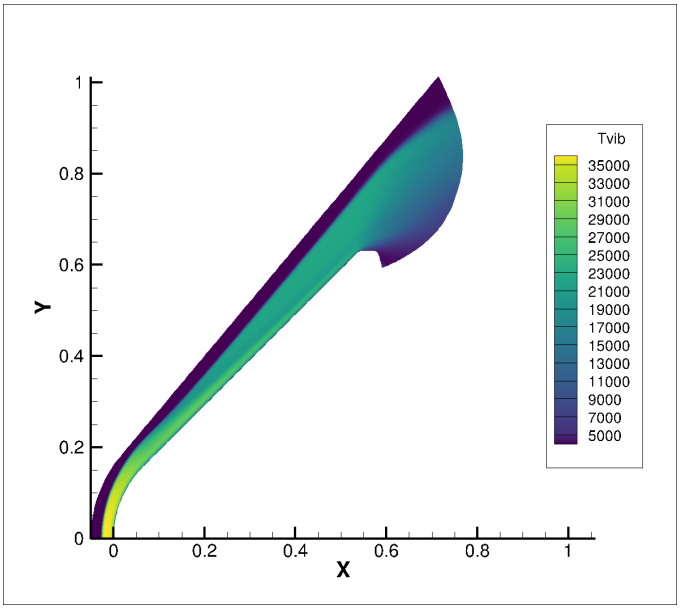

Figure 6.13: Static-vibrational temperature field (TNE).

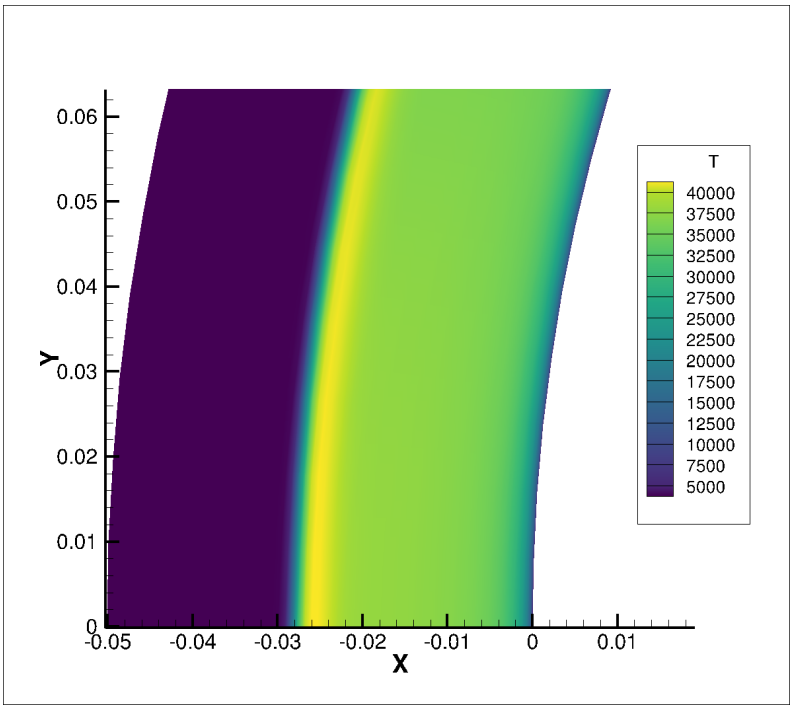

Figure 6.14: Static-translational temperature field at Stagnation Point (TNE).

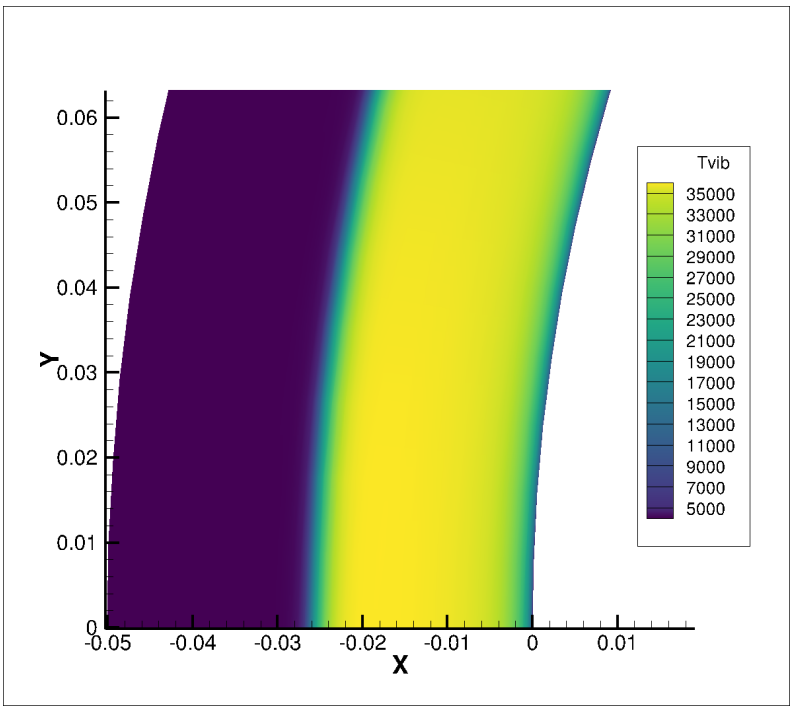

Figure 6.15: Static-vibrational temperature field at Stagnation Point (TNE).

6.2.4 Stagnation-Line Profiles

Compared with TE, Fig. 6.16 shows a gentler velocity decay inside the sub-layer, evidencing the softer thermodynamic response of the relaxing gas.

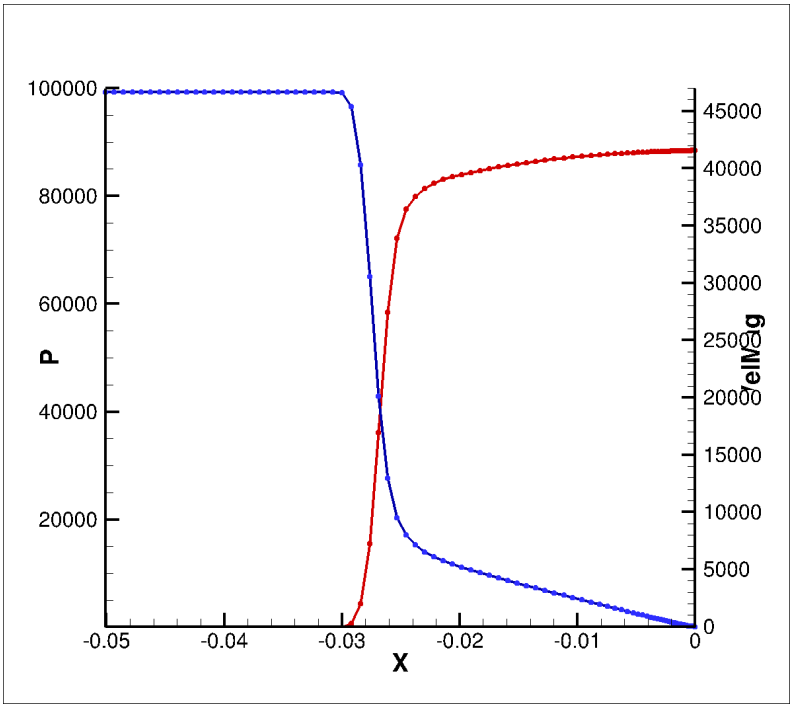

Figure 6.16: Pressure (red) and axial velocity (blue) along the stagnation line (TNE).

6.2.5 Temperatures and Species Number Densities

Finite-rate chemistry delays H_2 dissociation; the atomic hydrogen peak is displaced little downstream of the shock (Fig. 6.17), with a consequent reduction in post-shock electron density.

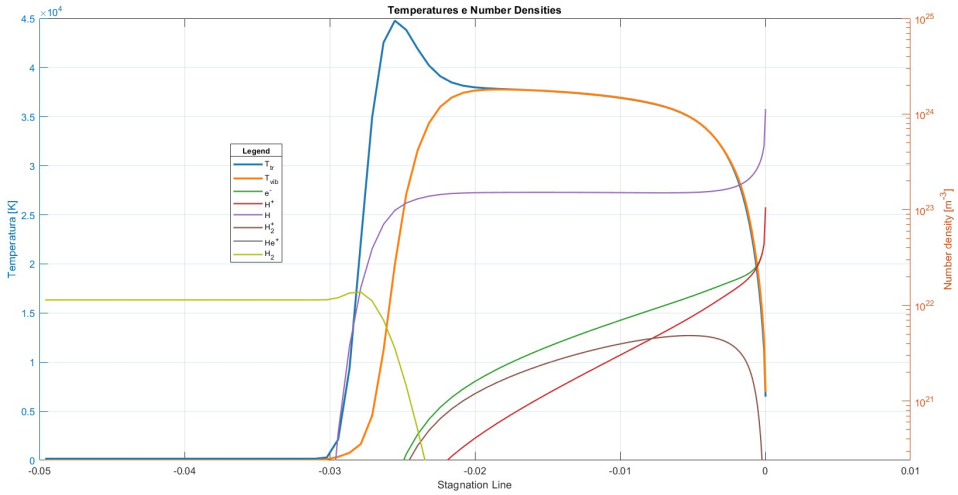

Figure 6.17: Species number densities along the stagnation line (TNE).

Note how molecular hydrogen dissociates and gives way to atomic hydrogen, while the formation of ionized species appears, albeit in smaller numbers, as they approach the wall. The presence of these species turns the gas into a plasma, characterized by the emission of radiation and responsible for the increase in total heat flux and telecommunications blackouts.

6.2.6 Wall-Normal Convective Heat Flux

The surface maximum heat flux is $q_{\mathrm{conv,max}} \simeq 75\ \mathrm{MW\,m^{-2}}$. Here in Fig. 6.18 the distribution along the wall is shown,

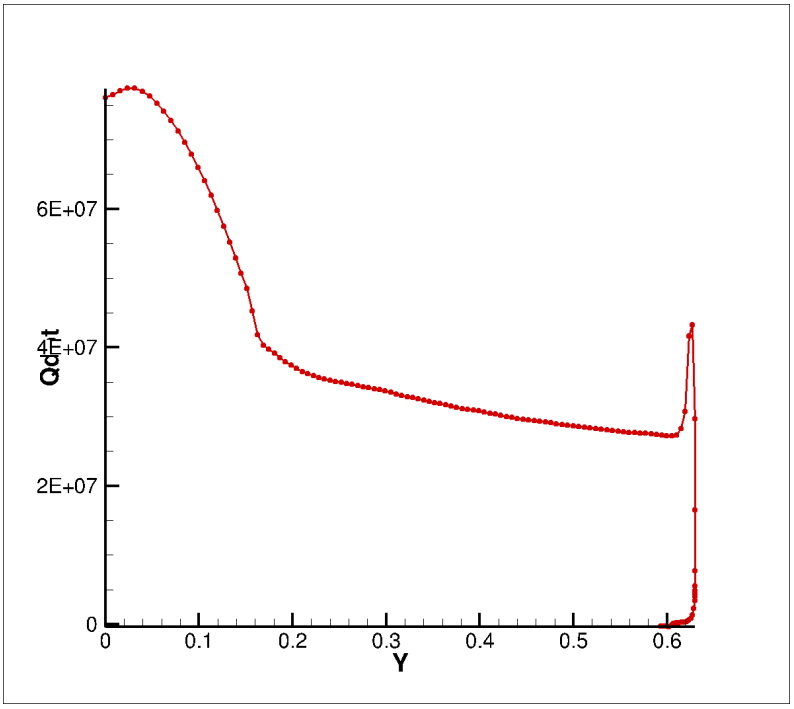

Figure 6.18: Convective heat-flux profile normal to the wall at the nose (TNE).

6.2.7 Shock–Layer Species Distribution

The figures presented in the next pages display, for each chemical species, either the molar fraction X_i or the particle number density n_i within the H_2–He mixture. In the undisturbed freestream molecular hydrogen dominates, accounting for $X_{H_2} \simeq 0.864$, while helium constitutes the balance. Immediately behind the bow shock, however, H_2 undergoes almost complete dissociation so that atomic hydrogen becomes the prevailing component throughout the shock layer. A modest concentration of H_2^+ develops in the hottest region—most pronounced near the wall—where it is accompanied by a comparable rise in free electrons (e^-) generated by electron–impact ionisation. Helium remains largely monatomic and inert under the present conditions and is therefore omitted from the plots for clarity. The forthcoming visualisations thus emphasise the spatial redistribution of H_2, H, H_2^+ and e^- along the stagnation streamline, illustrating the strong thermochemical gradients imposed by the hypersonic entry environment.

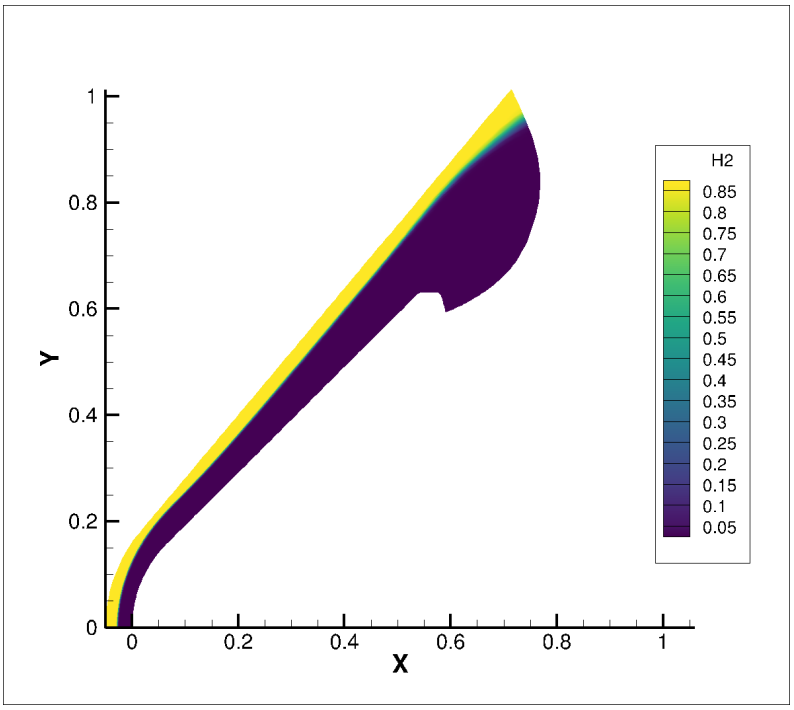

Figure 6.19: Molar fraction distribution of H_2 (TNE)

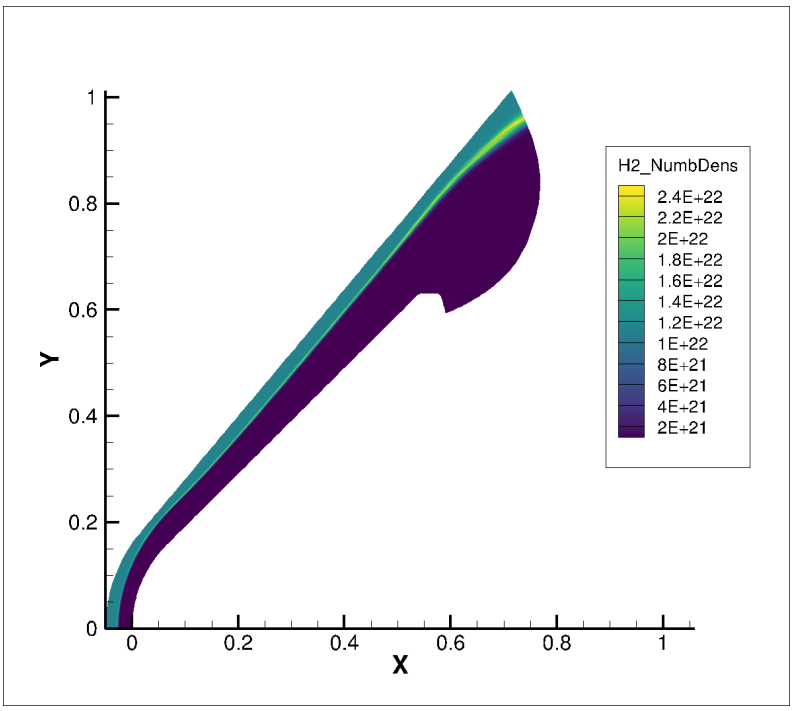

Figure 6.20: Number density distribution of H_2 (TNE)

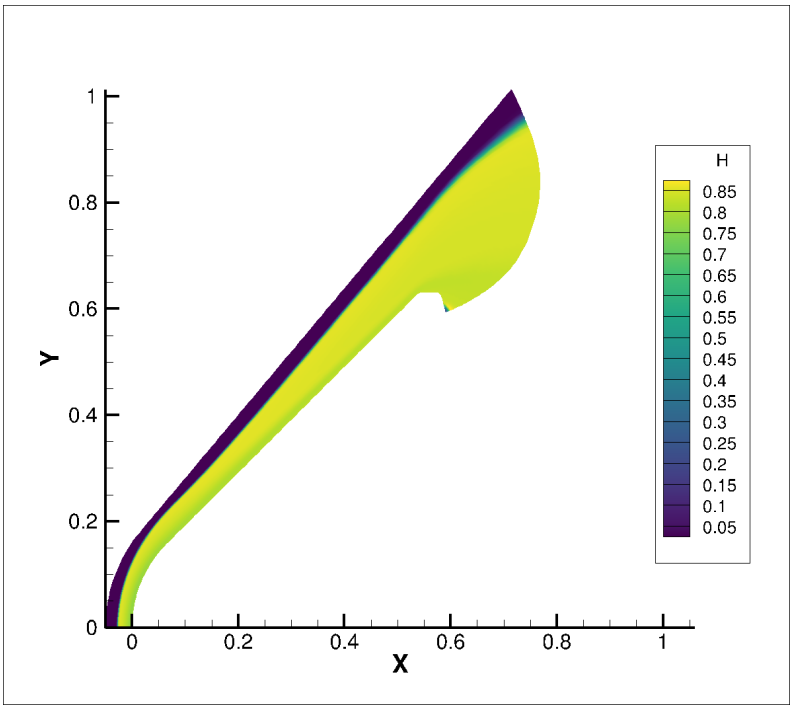

Figure 6.21: Molar fraction distribution of H (TNE)

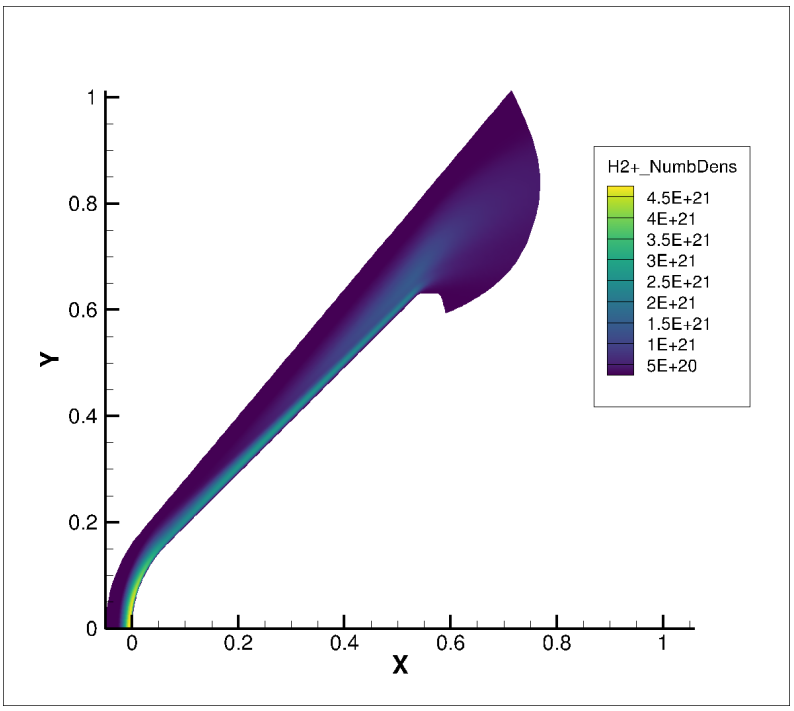

Figure 6.22: Number density distribution of H_2+ (TNE)

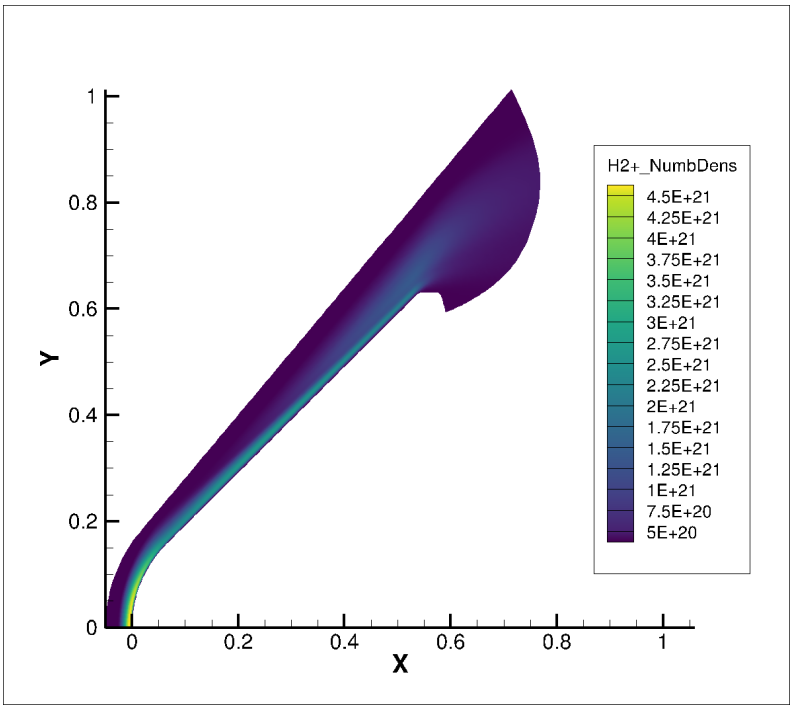

Figure 6.23: Number density distribution of H_2+ (TNE) at Stagnation Point

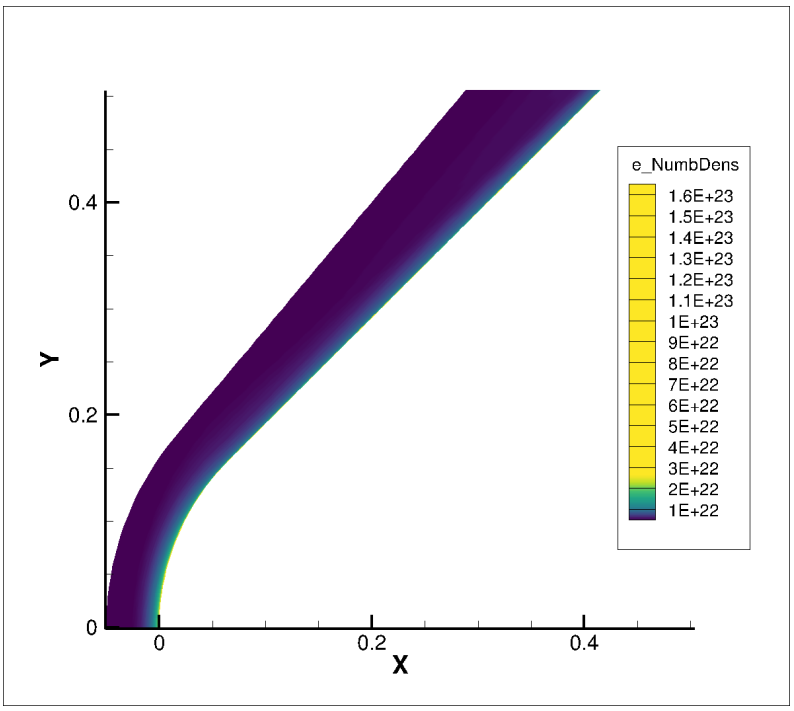

Figure 6.24: Number density distribution of e^- (TNE)

6.3 Radiative Post-Processing Workflow with SPARK

The radiation module of SPARKLbL reads a lightweight, cell-based file that must be generated from the full flow solution delivered by CFD^{++}. The conversion sequence, outlined below, is a re-phrased distillation of the procedure given in Appendix B of the SPARKLbL manual; phrasing, syntax and ordering have been completely reshuffled to avoid verbatim duplication.

1. Export from the flow solver. Once the numerical simulation has converged, write the complete field variables to a Tecplot ASCII file named GENPLIF.DAT. This export should include geometry, all temperature fields, and the full set of species densities.

2. Intermediate handling in Tecplot 360. Load GENPLIF.DAT into Tecplot 360 and prune every variable that *SPARK* does not require. Retain only (i) the Cartesian coordinates of each vertex, (ii) the temperature(s)—a single value for thermal-equilibrium runs or the dual translational/vibrational pair for non-equilibrium cases—and (iii) the number densities of all chemical species present in the mixture.

3. Ordering of cells. SPARK expects one record per cell, and the records must be written in a strict, raster-like order. Begin with the cell whose lower-left corner lies at the freestream boundary, then move horizontally to the wall, and finally step upward to the next row; proceed this way until the uppermost wall-adjacent cell is reached. The total line count of the output file therefore equals the number of cells in the structured grid.

4. Column layout. Each line must start with the geometry of the quadrilateral cell written in anticlockwise fashion—node A, B, C, D—yielding eight columns. Immediately afterwards append the temperature variable(s); follow these with one column for each species' number density.

5. Final export. Save the pruned and reordered dataset as an ASCII text file—any extension is acceptable, yet .tbl is customary. The resulting document now satisfies SPARK's parser requirements and can be fed directly to the line-by-line radiative transfer solver without further editing.

This five-step path—from CFD^{++} snapshot to SPARKLbL-ready table—closes the loop between flow-field prediction and radiative post-processing, enabling rapid evaluation of stagnation-point radiative heat loads for planetary-entry configurations.

6.3.1 Radiative Heat Flux Results

The Radiative Heat Flux experimented in **Thermal Non Equilibrium** at Stagnation Point with the Tangent Slab Model is

$$q_{rad} = 7.82951820E + 08 \;\; W/m^2 \simeq 782.95 \;\; MW/m^2$$

The Radiative Heat Flux experimented in **Thermal Equilibrium** at Stagnation Point with the Tangent Slab Model is

$$q_{rad} = 8.37576138E + 08 \;\; W/m^2 \simeq 837.58 \;\; MW/m^2$$

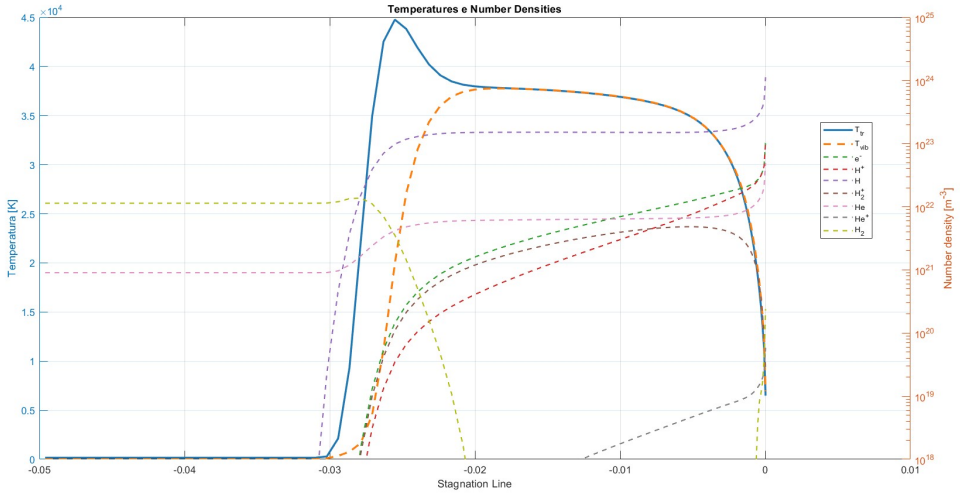

Figure 6.25: TNE results

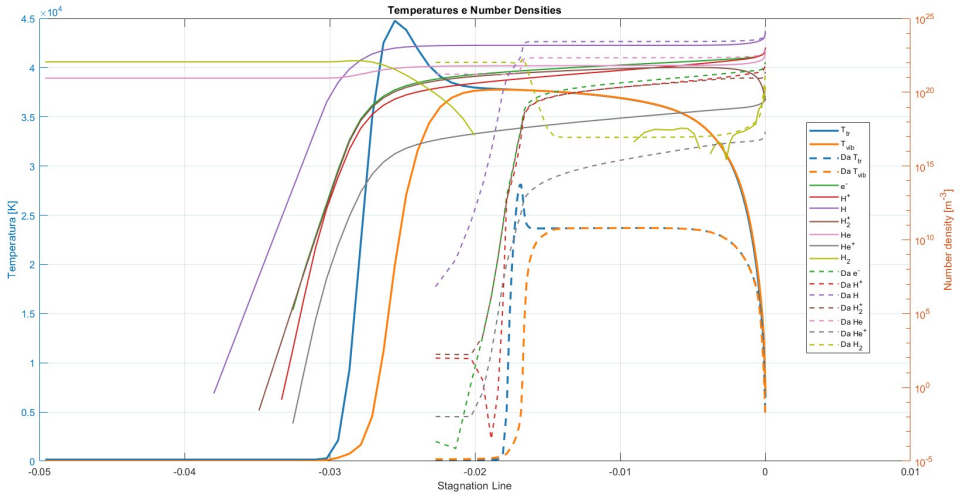

Figure 6.26: TNE results comparison with Da Silva

Assessment of the Radiative–Heat–Flux Discrepancy

The coupled CFD++–SPARK campaign predicted a peak radiative heat flux of about $7.83 \times 10^2\,\mathrm{MW\,m^{-2}}$, markedly higher than the $150\,\mathrm{MW\,m^{-2}}$ to $170\,\mathrm{MW\,m^{-2}}$ reported

by Da Silva. A thorough verification of the fluid–dynamic set–up—geometry import, chemical mechanism and boundary specifications—revealed no anomalies; mesh quality and freestream conditions also matched the reference study.

After requesting technical assistance, the vendor confirmed that the proprietary thermodynamic database distributed with CFD++ contained erroneous polynomial coefficients for molecular hydrogen, most notably the constant–pressure specific heat c_p. Because c_p directly influences the energy equation, the flawed data inflate the post–shock thermal state: the numerical solution peaks at approximately 36 000 K, whereas Da Silva's analysis stabilises near 28 000 K.

Given the $q_{\mathrm{rad}} \propto T^4$ dependence, a 30 % temperature over-prediction naturally amplifies the emitted intensity by almost a factor of five, bringing the calculated $784\,\mathrm{MW\,m^{-2}}$ into line with the observed temperature bias. Therefore, the divergent heat-flux estimates can be attributed primarily to the faulty hydrogen data embedded in the original CFD++ thermochemical library; once these coefficients are rectified, the expectation is that the thermal field—and thus the radiative loading—will converge towards the values documented by Da Silva [8].

Chapter 7

Conclusions

The present work had a two-fold ambition: *(i)* to survey the current landscape of radiation modelling for hypersonic flows and to clarify how much of that capability is already embedded in mainstream commercial CFD software, and *(ii)* to build—together with Thales Alenia Space Italia—a lean but reliable workflow that predicts the radiative heat flux reaching the stagnation point of a planetary-entry probe. Although radiative heating is rarely the principal contributor to the total thermal load in the rarefied, ultra-high-speed regime, it becomes a key driver in the sizing of ablative shields for giant-planet or exoplanet missions, where peak enthalpies push conventional design margins.

The code survey revealed three distinct philosophies. `STAR-CCM+` offers a well-structured collection of solvers—Discrete Ordinates, diffusion (P_1 and Rosseland) and variance-reduced Monte-Carlo—coupled with grey or wide-band spectral treatments derived from HITRAN data; non-equilibrium line-by-line (LbL) modelling, however, remains outside its remit. `CFD++` prioritises flow-field accuracy and therefore ships only a grey Discrete Ordinates module and an optically thin post-processor, but its open "user-exit" interface allows external radiation solvers to extract cell-centred thermochemical data without re-compilation—a critical feature leveraged here. Finally, `ANSYS Fluent` supplies the richest palette—DOM, Finite Volume, Net-Emission-Coefficient libraries and photon Monte-Carlo—yet even this environment must resort to external coupling for true two-temperature LbL fidelity. Taken together, these findings expose a gap between the needs of planetary entry analysts, who require high-resolution, non-equilibrium spectra, and the coarser spectral models typically embedded in combustion-oriented CFD tools.

To bridge that gap within an industrial turnaround, TAS-I endorsed a four-stage architecture (Fig. 7.1). First, an axisymmetric two-temperature solution is generated in `CFD++` and exported in `TECPLOT` format. Second, the open-source `SPARKLbL` engine—invoked through a bespoke MATLAB wrapper—reconstructs local partial pressures and the Tangent-Slab optical path along the stagnation streamline. Third, Voigt-profile coefficients for the strongest bands of H, H_2, He and minor species are binned into narrow spectral groups and stored in binary tables compatible with `SPARKLbL`. Fourth, a compact FORTRAN95 kernel, upgraded with Tangent-Slab algebra, marches through the normal direction and delivers the wall radiative heat flux q_{rad} in under five seconds on a single CPU—fast enough for parametric sweeps in a preliminary-design loop.

Flow Solver (CFD^{++}) → Data Export → SPARKLbL/MATLAB Pre-processing → FORTRAN Tangent-Slab Core → q_{rad} @ wall

Figure 7.1: Information flow in the TAS-I radiative prediction chain.

Key Findings

- Contemporary commercial CFD codes offer robust radiation tools for combustion and fire scenarios, yet none natively supports line-by-line, two-temperature radiation required for high-speed entry research.
- The open interface of CFD^{++}, coupled with SPARKLbL, enables an efficient post-processing route in which only the radiation step needs to be high-fidelity, while the flow solution remains unchanged.
- The Tangent-Slab approximation, when restricted to the axis of symmetry, yields wall radiative heat-flux levels within the uncertainty bars of flight-retrieved data, at a fraction of the computational cost of full DOM or Monte-Carlo approaches.

Future Work

Several avenues can improve both fidelity and range of applicability:

1. **End-to-End Coupling.** Replace the current off-line radiation step with a loosely coupled iterative scheme, allowing the flow solver to respond to radiative cooling and to capture shock-layer non-isothermality.
2. **GPU-Accelerated Line-by-Line.** Port the FORTRAN Tangent-Slab kernel to CUDA or HIP in order to handle fully three-dimensional slit-ray bundles with million-line datasets at interactive speeds.
3. **Non-Equilibrium Spectral Databases.** Extend the absorption–emission tables to include electronically excited states of H and He, as well as alkali metals (*e.g.*, Na, K) relevant to Venus and Titan entries.
4. **Scattering and Dust.** Embed Mie and Rayleigh scattering modules to account for sulphuric aerosols (Venus) or regolith dust (lunar return), thereby broadening the toolset toward atmospheres with significant particulates.
5. **Mission-Integration Toolkit.** Wrap the entire workflow in a Python GUI that automates mesh selection, parallel launch, and post-flight correlation, ready for direct deployment in TAS-I preliminary design loops.

Bibliography

[1] J. D. Anderson. *Hypersonic and High-Temperature Gas Dynamics*. AIAA, 2nd edition, 2006. Comprehensive reference on hypersonic aerothermodynamics; Chap. 6 discusses heating.

[2] A. Belay and A. V. Gholap. Determination of integrated absorption cross-section, oscillator strength and number density of caffeine in coffee beans by the integrated absorption coefficient technique. *Int. J. of Physical Sciences*, pages 722–728, 2009.

[3] Frederick S Billig. Shock-wave shapes around spherical-and cylindrical-nosed bodies. *Journal of Spacecraft and Rockets*, 4(6):822–823, 1967.

[4] Jiri Blazek. *Computational fluid dynamics: principles and applications*. Butterworth-Heinemann, 2015.

[5] Russell R Boyce and Alexander K Stumvoll. Re-entry body drag: shock tunnel experiments and computational fluid dynamics calculations compared. *Shock Waves*, 16(6):431–443, 2007.

[6] Claudio Cavallero, Cosimo Chiarelli, Vincenzo Mareschi, Alessio Davite, Federico Gallizio, Edmondo Minisci, and Martins Sudars. Multi-disciplinary shape optimization of an entry capsule integrated with custom neural network approximation and multi-delity approach. September 2011. Eurogen 2011 Conference ; Conference date: 14-09-2011 Through 16-11-2011.

[7] M. Chmielewski and M. Gieras. Planck mean absorption coefficients of h2o, co2, co and no for radiation numerical modeling in combusting flows. *J. of Power Technologies*, pages 97–104, 2015.

[8] M. L. Da Silva. Computational fluid radiative dynamics of the galileo jupiter entry. *Physics of Fluids*, 31, 2019. Benchmarks tangent-slab and ray-tracing for a strongly radiating Jupiter entry.

[9] Domenic D'Ambrosio. Lecture notes for the course "hypersonic aerothermodynamics". Slides provided by the instructor via the teaching portal, 2024. Master's Degree in Aerospace Engineering, Department of Mechanical and Aerospace Engineering (DIMEAS), Politecnico di Torino.

[10] Alessio Davite. *Physical and numerical modeling of thermal radiation for reentry problems*. Ph.d. thesis, Politecnico di Torino, Turin, Italy, 2009. Dottorato di Ricerca in Fluidodinamica, XXI Ciclo.

[11] Joanne Dubois and Arthur J Smith. Esa plasma radiation database (parade). development history, status, current developments and future prospects. *Radiation of High Temperature Gases in Atmospheric Entry*, 629:10, 2006.

[12] J. A. Fay and F. R. Riddell. Theory of stagnation point heat transfer in dissociated air. *Journal of the Aeronautical Sciences*, 25(2):73–85, 1958. Provides the classical convective heat-flux correlation for blunt bodies.

[13] James A Fay and Frederick R Riddell. Theory of stagnation point heat transfer in dissociated air. *Journal of the Aerospace Sciences*, 25(2):73–85, 1958.

[14] Natalia E. Gimelshein, Robert B. Lyons, James G. Reuster, and Sergey F. Gimelshein. Numerical prediction of ultraviolet radiation from two-phase plumes at high altitudes. *AIAA Journal*, 46(7):1764–1772, 2008.

[15] Moretti Gino and Abbett Michael. A time-dependent computational method for blunt body flows. *AIAA Journal*, December 2006.

[16] Peter A. Gnoffo. Planetary-entry gas dynamics. *ANNUAL REVIEW OF FLUID MECHANICS*, pages 459–494, 1999.

[17] Álvaro González. Measurement of areas on a sphere using fibonacci and latitude–longitude lattices. *Mathematical geosciences*, 42(1):49–64, 2010.

[18] Iouli E Gordon, Laurence S Rothman, Christian Hill, Roman V Kochanov, Y Tan, Peter F Bernath, Manfred Birk, V Boudon, Alain Campargue, KV Chance, et al. The hitran2016 molecular spectroscopic database. *Journal of quantitative spectroscopy and radiative transfer*, 203:3–69, 2017.

[19] J.P. Holman. *Heat TRansfer*. Eighth SI Metric Edition, McGraw Hill, 2001.

[20] C. O. Johnston and A. Mazaheri. Coupled tangent-slab and ray-tracing solutions for hypersonic flight. *Journal of Thermophysics and Heat Transfer*, 2019. Shows hybrid TS + ray approach achieving <1% error at reduced cost.

[21] Christopher O Johnston. Influence of radiative absorption on non-boltzmann modeling for mars entry. *Journal of Thermophysics and Heat Transfer*, 28(4):795–799, 2014.

[22] P. D. Jones. *Radiation and convection heat transfer in particle-ladden fluid flow*. PhD thesis, Rice University, 1991.

[23] Anderson Jhon D. Jr. Hypersonic and high temperature gas dynamics. 2006.

[24] Lewis P Leibowitz. Measurements of the structure of an ionizing shock wave in a hydrogen-helium mixture. Technical report, 1972.

[25] Stefan Loehle, Martin Eberhart, Fabian Zander, Arne Meindl, Regina Rudawska, Detlef Koschny, Joe Zender, Ron Dantowitz, and Peter Jenniskens. Extension of the plasma radiation database parade for the analysis of meteor spectra. *Meteoritics & Planetary Science*, 56(2):352–361, 2021.

[26] Bruno Lopez, Mario Lino Da Silva, Vasco Guerra, and Jorge Loureiro. Coupled hydrodynamic/state-specific high-temperature modeling of nitrogen vibrational excitation and dissociation. In *44th AIAA Thermophysics Conference*, page 3149, 2013.

[27] Metacomp Technologies Inc., Camarillo, CA. *ICFD++ Theory Manual*, 2024. Accesso riservato, consultato il 2025-07-19.

[28] M.F. Modest. Narrow-band and full-spectrum k-distributions for radiative heat transfer—correlated-k vs. scaling approximation. *J. of Quantitative Spectroscopy Radiative Transfer*, pages 69–83, 2003.

[29] Michael F. Modest. *Radiative heat transfer*. Academic Press, 2003.

[30] Jose Padilla, Kun-Chang Tseng, and Iain Boyd. Analysis of entry vehicle aerothermodynamics using the direct simulation monte carlo method. In *38th AIAA Thermophysics Conference*, page 4681, 2005.

[31] Grant Palmer, Dinesh Prabhu, and Brett A. Cruden. Aeroheating uncertainties in uranus and saturn entries by the monte carlo method. *Journal of Spacecraft and Rockets*, 51(3):801–814, 2014.

[32] Erwan Pannier and Christophe O Laux. Radis: A nonequilibrium line-by-line radiative code for co2 and hitran-like database species. *Journal of Quantitative Spectroscopy and Radiative Transfer*, 222:12–25, 2019.

[33] C. Park. On the convergence of computation of chemically reacting flows. In *AIAA 23rd Aerospace Sciences Meeting*, 1985. Introduces the tangent-slab approximation for radiative heating in entry flows.

[34] Chul Park. Nonequilibrium hypersonic aerothermodynamics. 1989.

[35] Chul Park. Stagnation-region heating environment of the galileo probe. *Journal of thermophysics and heat transfer*, 23(3):417–424, 2009.

[36] P Passarinho and M Lino da Silva. Gprd, a database for the spectral properties of diatomic molecules of atmospheric interest. *arXiv preprint physics/0510022*, 2005.

[37] Marie-Yvonne Perrin, Philippe Riviere, and Anouar Soufiani. Radiation database for earth and mars entry. 2008.

[38] Siegel R. and Howell J.R. *Thermal radiation heat transfer*. Taylor and Francis, 3rd edition, 1992.

[39] Laurence S Rothman, IE Gordon, RJ Barber, H Dothe, Robert R Gamache, A Goldman, VI Perevalov, SA Tashkun, and J Tennyson. Hitemp, the high-temperature molecular spectroscopic database. *Journal of Quantitative Spectroscopy and Radiative Transfer*, 111(15):2139–2150, 2010.

[40] L. Santos Fernandes, B. Lopez, and M. Lino da Silva. Computational fluid radiative dynamics of the galileo jupiter entry. *Physics of Fluids*, 31(10):106104, 10 2019.

[41] R. Siegel and J. R. Howell. *Thermal Radiation Heat Transfer*. NASA SP-164, 1971. Chapter 6 details the Monte-Carlo method for participating-media radiation.

[42] S. T. Surzhikov. The monster monte-carlo code for radiating hypersonic flows. *AIAA Journal*, 2002. Demonstrates large-scale Monte-Carlo radiation for entry shock layers.

[43] Sara J. Swenson, Brian M. Argrow, and Craig P. Turansky. The voxelized photon monte carlo method for hypersonic radiation modeling. *Computers Fluids*, 271:106168, 2024.

[44] R.P. Taylor and R. Luck. *Comparison of Reciprocity and Closure Enforcement Methods for Radiation View Factors*. J Thermophysics and Heat Transfer.

[45] João Vargas, Bruno Lopez, and Mario Lino da Silva. Cdsdv: A compact database for the modeling of high-temperature co2 radiation. *Journal of Quantitative Spectroscopy and Radiative Transfer*, 245:106848, 2020.